



저작자표시-비영리-변경금지 2.0 대한민국

이용자는 아래의 조건을 따르는 경우에 한하여 자유롭게

- 이 저작물을 복제, 배포, 전송, 전시, 공연 및 방송할 수 있습니다.

다음과 같은 조건을 따라야 합니다:



저작자표시. 귀하는 원저작자를 표시하여야 합니다.



비영리. 귀하는 이 저작물을 영리 목적으로 이용할 수 없습니다.



변경금지. 귀하는 이 저작물을 개작, 변형 또는 가공할 수 없습니다.

- 귀하는, 이 저작물의 재이용이나 배포의 경우, 이 저작물에 적용된 이용허락조건을 명확하게 나타내어야 합니다.
- 저작권자로부터 별도의 허가를 받으면 이러한 조건들은 적용되지 않습니다.

저작권법에 따른 이용자의 권리는 위의 내용에 의하여 영향을 받지 않습니다.

이것은 [이용허락규약\(Legal Code\)](#)을 이해하기 쉽게 요약한 것입니다.

[Disclaimer](#)

공학박사학위논문

로터로 구동되는 새로운 공중조작
시스템의 동역학 및 제어

**Dynamics and Control Problems of Novel Aerial
Manipulation Systems with Rotor Actuation**

2021 년 2 월

서울대학교 대학원

기계항공공학부

양 현 수

로터로 구동되는 새로운 공중조작 시스템의 동역학 및 제어

Dynamics and Control Problems of Novel Aerial
Manipulation Systems with Rotor Actuation

지도교수 이 동 준

이 논문을 공학박사 학위논문으로 제출함

2020 년 10 월

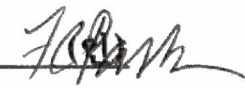
서울대학교 대학원

기계항공공학부

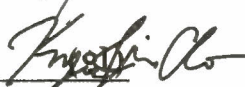
양 현 수

양현수의 공학박사 학위논문을 인준함

2020 년 12 월

위 원 장 : 박 종 우 (인) 

부위원장 : 이 동 준 (인) 

위 원 : 조 규 진 (인) 

위 원 : 박 재 홍 (인) 

위 원 : Christian Ott (인) 

Abstract

Dynamics and Control Problems of Novel Aerial Manipulation Systems with Rotor Actuation

Hyunsoo Yang

Department of Mechanical and Aerospace Engineering

The Graduate School

Seoul National University

In this thesis, we deal with dynamics and control problems of novel aerial manipulation systems with rotor actuation. Aerial manipulation systems include: 1) drone equipped with robotic arm inheriting flying capability of multi-rotor drone while it also inherits versatile manipulation capability from robotic arm; and 2) distributed rotor-based vibration suppression system which is developed to manipulate and transport of long flexible load by distributing scalable modules along with the load with onboard sensing capability.

The drone-manipulator system is inherited under-actuated property of conventional multi-rotor drone and a high degree of freedom of robotic manipulator while the system dynamics are fully coupled between these two subsystems. To deal with this under-actuated nonlinear dynamics, we reveal an underlying structure of the nonlinear drone-manipulator dynamics, which can substantially facilitate the control design and analysis by applying passive decomposition. We show that the Lagrange dynamics of drone-manipulator systems can

be completely decoupled into: 1) the center-of-mass dynamics in $E(3)$, which, similar to the standard drone dynamics, is point-mass dynamics with under-actuation and gravity effect; and 2) the “internal rotational” dynamics of the drone’s rotation and manipulator configuration, which assumes the form of standard Lagrange dynamics of a robotic manipulator with full-actuation and no gravity effect. Relying on this structure, we propose a novel backstepping-like end-effector tracking control law, which can allow us to assign different roles for the center-of-mass control and for the internal rotational dynamics control according to task objectives.

In the second part, RVM (Robot-based Vibration Suppression Modules) is proposed for the manipulation and transport of a large flexible object. Since the RVM is designed to be easily attachable/detachable to the object, this RVM allows distributing over the manipulated object so that it is scalable to the object size. The composition of the system is partly motivated by the MAGMaS (Multiple Aerial-Ground Manipulator System), however, since the multirotor-drone usage is mechanically too complicated and its design is not optimized for manipulation, thus we overcome these limitations using distributed RVMs and newly developed theory. For this, we first provide a constrained optimization problem of RVM design with the minimum number of rotors, so that the feasible thrust force is maximized while it minimizes undesirable wrench and its own weight. Then, we derive the full dynamics and elucidate a controllability condition with multiple distributed RVMs and show that even if multiple, their structures turn out similar to composed with a single multi-rotor drone. We also elucidate the optimal placement of the RVM

via the usage of LQG (Linear Quadratic Gaussian) framework.

Keywords: Aerial Robot, Aerial Manipulation, Dynamics, Control, Optimal Placement, Underactuation

Student Number: 2014-30352

Contents

List of Figures	vi
1 Introduction	1
1.1 Motivation and Contribution	1
1.2 Outline	8
2 Dynamics and Control of Single Drone-Manipulator System	10
2.1 Introduction	10
2.2 Lagrange Dynamics of Quadrotor-Manipulator System	13
2.3 Passive Decomposition of Quadrotor-Manipulator System	18
2.4 Trajectory Tracking Control Design	25
2.5 Conclusion	32
3 Cooperative Hierarchical Control of Multiple Drone-Manipulator Systems	33
3.1 Introduction	33
3.2 Preliminary	36
3.2.1 Dynamics Modeling of QM System	36
3.2.2 Dynamics Decomposition and Control of QM System	37
3.3 Hierarchical Control Framework for Multiple QM Systems	40
3.3.1 Object Behavior Design	41
3.3.2 Optimal Cooperative Force Distribution	42
3.3.3 Force Control of QM System with Object Stiffness Model	46
3.3.4 Simulation	53
3.4 Conclusion	56
4 Flexible Load Vibration Suppression using Multi-rotor Drone	57
4.1 Introduction	57
4.2 System Description	59
4.3 System Modeling	62
4.3.1 Flexibility Modeling of the Load	62
4.3.2 Kinetic Energy of the MAGMaS	65
4.3.3 Potential Energy	67
4.3.4 Euler-Lagrange Dynamics	67

4.4	Control Design	69
4.4.1	Manipulator Control	70
4.4.2	Flexible Load Dynamics Analysis	72
4.4.2.1	Linearization	73
4.4.2.2	Controllability	75
4.4.3	Aerial Robot Control	80
4.5	Simulation	83
4.6	Conclusion	85
5	Rotor-based Vibration Suppression Module	86
5.1	Introduction	86
5.2	Robot-based Vibration Suppression Modules Design	89
5.2.1	System Description	89
5.2.2	Design Optimization	91
5.3	Dynamics Modeling with Multiple Distributed RVMs	93
5.3.1	Flexibility Modeling of the Load	94
5.3.2	Euler-Lagrange Dynamics	96
5.4	Controllability Analysis	98
5.4.1	Flexible Load Dynamics Linearization	98
5.4.2	Controllability	100
5.5	Optimal placement	105
5.5.1	Optimal Placement of Actuator	105
5.5.2	Optimal Placement of Module	108
5.5.3	Control Design	113
5.6	Experiment	113
5.7	Conclusion	116
6	Conclusion and Future Work	117
6.1	Conclusion	117
6.2	Future Work	119

List of Figures

2.1	Quadrotor with m -DOF robot arm: $p = (x, y, z)$ is quadrotor's center position, $p_e = (x_e, y_e, z_e)$ end-effector position, and λ thrust force input.	13
2.2	Snapshots of end-effector trajectory tracking of a planar quadrotor with 2-DOF arm with error convergence. Here, $\eta_1 = \phi + \theta_1 + \theta_2$ and $\eta_2 = \phi + \theta_1$	29
2.3	Snapshots of the quadrotor-manipulator system under admittance-type force control with force profile.	31
3.1	Hierarchical cooperative control framework of multiple QM systems	41
3.2	Contact force decomposition and object stiffness model.	45
3.3	Snapshots of the object pushing task using the multiple QM system under admittance-type force control with force profile.	52
3.4	Snapshots of the object transport using cooperative QM systems control of compliant behavior with unknown mass and parameter adaptation.	54
3.5	Snapshots of the quadrotor-manipulator system under admittance-type force control with force profile.	55
4.1	MAGMaS composed of one ground manipulator and three aerial robots with a co-manipulated large object.	58
4.2	Sketch of the configuration of the MAGMaS.	61
4.3	Euler-Bernoulli beam deflection model.	62
4.4	Ongoing experimental setup for the MAGMaS with a quadrotor, a flexible load and a manipulator.	80
4.5	Snapshot of the eight-shaped trajectory tracking with proposed controller. Color in the flexible load represents its relative deflection w.r.t. a rigid load.	81
4.6	Simulation results with three different controllers: 1) proposed control; 2) PD control; 3) manipulator control w/o vibration suppression. Trajectory tracking (top) and tracking with perturbation (bottom). An external force is applied to at 8, 16s for the bottom.	82

5.1	Cooperative manipulation of flexible object composed of one ground manipulator and distributed RVMs (Robot-based Vibration suppression Module).	87
5.2	Optimized design and rotor allocation of RVM.	88
5.3	Cooperative manipulation of flexible object composed of one ground manipulator and distributed two RVMs.	89
5.4	Sketch of the configuration of the system.	92
5.5	Euler-Bernoulli beam deflection model.	94
5.6	Optimal placement of two RVMs on aluminum bar. $\det(W_c)$ provides $(l_1, l_2) = (1.15m, 1.95m)$ (left). $\text{tr}(W_c)$ provides $(l_1, l_2) = (1.25m, 1.95m)$ (right).	106
5.7	Optimal placement of two RVMs on aluminum bar. Left top plot represents control cost J_1 and right top plot represents estimation cost J_2 . Bottom plot shows resultant LQG cost.	112
5.8	Snapshots and load-tip deflection plot for stationary robot arm under external disturbances. Red arrows represent times external forces exerted.	114
5.9	Snapshots and load-tip deflection plot for one-end position manipulated by robot arm. Yellow shaded columns represent times the robot arm moves.	114
5.10	Snapshots for vibration suppression of flexible load using distributed RVMs with pose manipulated by human operator.	115

Chapter 1

Introduction

1.1 Motivation and Contribution

Multi-rotor drones have been researched extensively in recent years due to their agile performance, relative-easiness to control, and affordability, with the rapid advancements in sensors, actuators, materials, and embedded computing. These multi-rotor drone, or more generally, unmanned aerial vehicles (UAVs) or aerial robots, are also promising to extend the ground-bounded ability of the typical (wheeled) mobile robots to the three dimensional space. Some application examples include: remote landscape survey, aerial photography and movie shooting, surveillance and reconnaissance, etc. Free flying motion control problem of small-size multi-rotor aerial robots is now well established with many strong theoretical results (e.g., [1–10]) and commercial systems (e.g., [11, 12]). So successful has been this multi-rotor aerial robot particularly for the aerial photography and visual inspection applications by extending humans’ eyes to the sky.

The next step, naturally along this line of reasoning, would then be to extend humans’ hands to the sky, namely, the problem of aerial operation and

manipulation (e.g., [13–16]), which can be useful for such applications as infrastructure maintenance [17], remote construction [18], object transport and assembly [19–21], etc. To make this multi-rotor drone a truly versatile and practically useful robotic platform, it is also desirable, if not necessary, to endow them with a capability of manipulation and interaction with environment/object through some physical power change. Some results for this include: 1) cable-suspended transport tasks using a single or multiple quadrotors [22, 23]; 2) grasping using a gripper attached on aerial robots [24] and stability analysis to prevent instability caused by inertia changing [25]; 3) avian-inspired passive perching mechanism without no active actuation [26]; and 4) aerial manipulation with a tool (e.g., screw driver) rigidly-attached on the quadrotor and its internal dynamics stability analysis [27, 28].

The problem of employing and controlling the quadrotor with a multi-degree-of-freedom (DOF) robotic manipulator, which would likely be one of the promising choice platform for the aerial manipulation has been actively studied only from few years ago with much less results available (e.g., [29–33]). The key challenge inherent in this quadrotor-manipulator (QM) system is that: 1) the combined QM-system dynamics, which needs to be considered when precise/dynamic control is desirable, is very complicated and nonlinear with total system’s DOF at least the same as the quadrotor’s 6-DOF in $SE(3)$; and 2) the quadrotor platform is under-actuated in its translation with the body-fixed 1-DOF thrust force control input, although the quadrotor rotation and the manipulator itself are typically fully-actuated. Perhaps, due to these challenges, the majority of the available results on this QM-system rather consider the quadrotor and the manipulator as separate systems and see their

coupling as disturbance (e.g., [29, 30]); or do not fully take into account the QM-system’s large-dimensional nonlinear dynamics in $SE(3)$ and/or the issue of under-actuation when designing/analyzing control laws (e.g., [30, 31, 33]).

The aerial manipulation is not limited to the conventional multi-rotor drone system. In recent year, there have been many attempts to adapt distributed rotor-based actuation to aerial manipulation by introducing novel aerial robot platform or partially adapting the rotors to the robotic system. In [34], ODAR (Omni-Directional Aerial Robot) is introduced to have omni-directional wrench generation capability for aerial manipulation and LASDRA (Large-size Aerial Skeleton System with Distributed Rotor Actuation) [35] is developed to enable aerial manipulation by adapting ODAR as a link while overcome limited payload and flight time. HALO and DRAGON (dual-rotor multi-link robot with ability of multi-DOF aerial transformation) is composed of multiple link with joint actuation and each link does not have flying capability. Hiryu-1 and 2 also consist of parallel link mechanism and joints actuated by thrusters and motors attached on each link. However, the above-mentioned results are limited in rigid object manipulation. On the other hand, many large-size objects often include long/slender object, such as bar, beam, and pipe. For this long/slender object handling, an induced torque by center-of-mass far from the grasping location is crucial as well as its high payload. As the length of the object gets longer, the deflection and the vibration become significant, thus it is hard to be handled by the conventional robotic system and possibly hazardous due to undesirable vibration.

Let us consider the problem of large-size object transport and manipulation with aerial robot. For this, the (virtually) unlimited workspace of the aerial

robots would be useful. However, at the same time, such construction usually requires manipulation of large-size objects (e.g., steel bar, wood beams, etc.) typically too heavy to carry by many usual aerial robots alone due to the inherent rotor-battery limitation. On the other hand, ground (mobile or fixed) manipulators are typically of high payload, yet, their workspace (or working height) limited. To address this challenge, the MAGMaS (Multiple Aerial-Ground Manipulator System) was proposed in [36] as a heterogeneous system composed of multiple ground (mobile) manipulators (with high payload, yet, limited workspace) and aerial robots (with large workspace, yet, limited payload) to collaboratively manipulate a large-size heavy object by utilizing their capabilities in a complementary manner. The MAGMaS, of course, can be useful for other applications as well, e.g., warehouse automation, manipulation of large/heavy repair/inspection tool, etc.

The main contribution of this thesis is to reveal an underlying structure of the nonlinear QM-dynamics, which can substantially facilitate the control design and analysis by applying passive decomposition [37–39]. More precisely, we show that, although often dauntingly complicated due to its nonlinearity and large-DOF, the Lagrange dynamics of the QM system, consisting of a 6-DOF quadrotor platform and m -DOF robotic manipulator, can be decomposed into the following two completely decoupled systems: 1) The center-of-mass translation dynamics in $E(3)$, which, similar to the standard quadrotor dynamics, is the point-mass dynamics under-actuated only with the body-fixed thrust force input and under the effect of gravity; and 2) The $(3 + m)$ -DOF “internal” dynamics of quadrotor’s rotation and manipulator configuration, which has the form of standard Lagrange dynamics of robot manipulators

with full-actuation, yet, without any gravity effect.

Relying on this revealed structure, we also propose a novel backstepping-like end-effector tracking control law for the QM-system, which allows us to utilize the redundancy of the QM-system, and, thereby, to assign different roles to the center-of-mass dynamics control (e.g., more authority during transportation task) and that of the internal rotational dynamics (e.g., more authority for precise end-effect control). We also perform a simulation to illustrate/verify our proposed control framework for a planar QM-system with 2-DOF robotic arm. This underlying structure of the QM-system and the proposed backstepping-like control framework, in fact, are equally applicable to *any* vehicle-manipulator systems such as spacecraft with a multi-DOF robotic arm or underwater vehicle equipped with robotic manipulators.

Standing upon our result on the dynamics and control of the single QM system [40], we propose a novel hierarchical cooperative control framework for multiple dynamic QM systems, which can endow the cooperatively-grasped object with an user-specific target behavior according to various task objective. Our proposed control framework is hierarchical and also modular with the following layers/sub-modules: 1) **Object behavior design**, which computes the required wrench for the cooperatively-grasped object to achieve the user-specific target behavior according to task objectives (e.g., trajectory tracking, velocity-field following, compliant interaction, etc.); 2) **Optimal cooperative force distribution**, which optimally assign contact force of each QM system to cooperatively achieve the desired object behavior, while minimizing a certain cost function and respecting the friction-cone constraints to prevent

slippage; and 3) **Individual QM system control**, which extends the end-effector position control of [40] for the admittance-type contact force control of each QM system with unknown object stiffness model and force sensor/estimator [41], while also explicitly taking into account the different dynamics characteristics of the (slower/coarse) quadrotor and the (faster/fine) manipulator.

The focus of [36], however, was, on top of proposing this new class of MAGMaS and its implementation, to propose the control framework for the large/slender *rigid* object manipulation by employing the complementary capabilities and redundancy of the ground-aerial robots. In this thesis, we extend this result of [36] to the case of load manipulation with *flexibility*, which is crucial for long/slender object manipulation, yet, not addressed in [36]. For this, we first provide a rigorous modeling of the MAGMaS with the (slender) load flexibility incorporated into that using Euler-Bernoulli beam theory. We then propose a novel collaborative control framework for the flexible load-tip pose tracking, where the ground manipulator provides slower nominal pose tracking with overall load weight holding, whereas the aerial robot¹ faster vibration suppression with some load weight sharing. We also elucidate the issue of controllability stemming from that the aerial robot provides less number of actuation than that of the modes of the load flexibility; and delineate some peculiar conditions for this vibration suppression controllability with their physical meaning manifested.

¹It is also worthwhile to mention that this aerial robot, by providing collocated load-tip actuation, can allow us to circumvent the well-known issue of nonminimum-phase dynamics for load-tip pose tracking control if only ground robot is employed [42, 43].

We propose a robot-based vibration suppression modules (RVM) which is optimally designed to manipulate the large flexible object while suppressing its vibration. Since the RVM is easily attachable/detachable to the object, an arbitrary number of the distributed RVMs can be adapted to various length-/shape/weight of object. The system composition of the RVM is partly motivated by our previous result of MAGMaS (Multiple Aerial-Ground Manipulator System) [44], which utilizes a single quadrotor at the flexible load-tip. However, the quadrotor requires mechanically complicated and large payload structure, e.g., passive rotational joint, to connect the object while allowing free rotation. Besides, the quadrotor is optimized for flying capability in terms of the number of the rotors and its allocation [7]. The design and distributed actuation principles are partly inspired by ODAR (Omni-Directional Aerial Robot) [34] and LASDRA (Large-size Aerial Skeleton System with Distributed Rotor Actuation) [35, 45]. In these two results, the aerial robots are composed of distributed unit modules designed to maximize control wrench for omnidirectional flying on each rigid link while the RVM is designed for vibration suppression of flexible object with a more simplified and compact design.

We aim the role of the RVM as follows: 1) vibration suppression of the flexible load; and 2) object weight sharing to support limited ground manipulator torque. Therefore, we first provide a novel RVM design by optimizing the thrust generation along the sagittal plane while minimizing undesirable wrench along other directions based on constrained optimization. Here, we utilize two rotors which is the minimum number that can generate control actuation along $E(2)$. Since an arbitrary number of the RVM can be utilized, we derive the system dynamics for arbitrary number of RVM and show that the flexible load

dynamics is composed of linear diagonal matrices even with multi-modules. In the control problem, since the number of vibration modes and RVM can be arbitrary and this might induce controllability issue, thus we come up with controllability condition and elucidate its physical meaning for the distributed RVMs thanks to dynamic structure similar to [44]. Furthermore, we provide not only the place not to allocate the RVM based on controllability but also the place the RVM needs to be allocated to maximize vibration suppression capability based on controllability gramian. Experiments are performed to demonstrate the effectiveness of the proposed theory and RVM.

1.2 Outline

The outline of this thesis is as follows. As the first part, in Chapter 2, we introduce dynamics and control problem of a single drone-manipulator system based on passive decomposition. Lagrange dynamics of the QM-system is derived in Sec. 2.2 with some structure shown. An interesting/useful underlying structure of the QM-dynamics, i.e., it is decomposable into the dynamics of the quadrotor-like center-of-mass dynamics and that of the internal rotation similar to standard fully-actuated robot arm dynamics with no gravity effect present, is revealed in Sec. 2.3 using passive decomposition [37–39]. Backstepping-like end-effector trajectory tracking control design is presented in Sec. 2.4, In Chapter 3, dynamics and control problem of a single drone-manipulator is extended to cooperation of multiple drone-manipulator system. The proposed hierarchical control framework and its constituting layers are presented in Sec. 3.3 with relevant simulation results. In the second part,

we introduce vibration suppression of flexible load using a multi-rotor drone in Chapter 4 and a novel rotor-based vibration suppression module in Chapter 5. Sec. 4.2 describes in depth the system at hand. In Sec. 4.3, the dynamical model of the system, including the vibrations in the load is derived and Sec. 4.4 makes use of it to construct the control scheme. Sec. 4.5 presents realistic simulation results which validate our approach. Sec. 5.2 explains how the RVM is optimally designed. In Sec. 5.3, the dynamical model of the system including the vibrations in the load is derived and Sec. 5.4 makes use of it to derive controllability and optimal placement. Sec. 5.6 presents experimental results which validate our approach. In Chapter 6, we summarize the contribution of this thesis with description of possible future works.

Chapter 2

Dynamics and Control of Single Drone-Manipulator System

2.1 Introduction

Multi-rotor drones¹ have been researched extensively in recent years due to their agile performance, relative-easiness to control, and affordability, with the rapid advancements in sensors, actuators, materials, and embedded computing. These quadrotors, or more generally, unmanned aerial vehicles (UAVs) or aerial robots, are also promising to extend the ground-bounded ability of the typical (wheeled) mobile robots to the three dimensional space. Some application examples include: remote landscape survey, aerial photography and movie shooting, surveillance and reconnaissance, etc. For this, many powerful results have been reported for the *motion control* of quadrotors (e.g.,[1–6]).

To make this quadrotor a truly versatile and practically useful robotic platform, it is also desirable, if not necessary, to endow them with a capability of

¹Throughout this thesis, we limit the term ‘drone’ to the multi-rotor type drone even though there are other types of drone including fixed-wing, VTOL (vertical takeoff and landing, etc. It is worthwhile to note that the proposed theories in this thesis can be applied to conventional multi-rotor drone, although we use the terminology ‘quadrotor’ mixed with ‘multi-rotor drone’.

manipulation and interaction with environment/object through some physical power change. Some results for this include: 1) cable-suspended transport tasks using a single or multiple quadrotors [22, 23]; 2) grasping using a gripper attached on aerial robots [24] and stability analysis to prevent instability caused by inertia changing [25]; 3) avian-inspired passive perching mechanism without no active actuation [26]; and 4) aerial manipulation with a tool (e.g., screw driver) rigidly-attached on the quadrotor and its internal dynamics stability analysis [27, 28].

The problem of employing and controlling the quadrotor with a multi-degree-of-freedom (DOF) robotic manipulator, which would likely be the ultimate choice platform for the aerial manipulation has been actively studied only from few years ago with much less results available (e.g., [29–33]). The key challenge inherent in this quadrotor-manipulator (QM) system is that: 1) the combined QM-system dynamics, which needs to be considered when precise/dynamic control is desirable, is very complicated and nonlinear with total system’s DOF at least the same as the quadrotor’s 6-DOF in SE(3); and 2) the quadrotor platform is under-actuated in its translation with the body-fixed 1-DOF thrust force control input, although the quadrotor rotation and the manipulator itself are typically fully-actuated. Perhaps, due to these challenges, the majority of the available results on this QM-system rather consider the quadrotor and the manipulator as separate systems and see their coupling as disturbance (e.g., [29, 30]); or do not fully take into account the QM-system’s large-dimensional nonlinear dynamics in SE(3) and/or the issue of under-actuation when designing/analyzing control laws (e.g., [30, 31, 33]).

In this chapter, applying passive decomposition [37–39], we reveal an underlying structure of the nonlinear QM-dynamics, which can substantially facilitate the control design and analysis. More precisely, we show that, although often dauntingly complicated due to its nonlinearity and large-DOF, the Lagrange dynamics of the QM system, consisting of a 6-DOF quadrotor platform and m -DOF robotic manipulator, can be decomposed into the following two completely decoupled systems:

- The center-of-mass translation dynamics in $E(3)$, which, similar to the standard quadrotor dynamics, is the point-mass dynamics under-actuated only with the body-fixed thrust force input and under the effect of gravity; and
- The $(3 + m)$ -DOF “internal” dynamics of quadrotor’s rotation and manipulator configuration, which has the form of standard Lagrange dynamics of robot manipulators with full-actuation, yet, without any gravity effect.

Relying on this revealed structure, we also propose a novel backstepping-like end-effector tracking control law for the QM-system, which allows us to utilize the redundancy of the QM-system, and, thereby, to assign different roles to the center-of-mass dynamics control (e.g., more authority during transportation task) and that of the internal rotational dynamics (e.g., more authority for precise end-effect control). We also perform a simulation to illustrate/verify our proposed control framework for a planar QM-system with 2-DOF robotic arm. This underlying structure of the QM-system and the proposed backstepping-like control framework, in fact, are equally applicable to

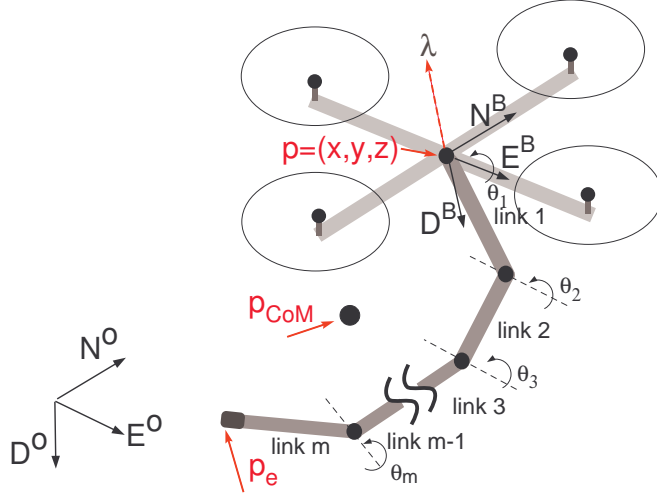


FIGURE 2.1: Quadrotor with m -DOF robot arm: $p = (x, y, z)$ is quadrotor's center position, $p_e = (x_e, y_e, z_e)$ end-effector position, and λ thrust force input.

any vehicle-manipulator systems such as spacecraft with a multi-DOF robotic arm or underwater vehicle equipped with robotic manipulators.

2.2 Lagrange Dynamics of Quadrotor-Manipulator System

Consider a quadrotor system in $SE(3)$ with a m -DOF serial-link robot arm as shown in Fig. 2.1. The configuration of this quadrotor-manipulator (QM) system can then be given by

$$q := [p; \phi; \theta] \in \mathbb{R}^n, \quad n := 6 + m$$

where $p = (x, y, z)^T \in \mathbb{R}^3$ is the quadrotor's geometric (as well as mass) center position in the inertial NED-frame, $\phi = (\phi_r, \phi_p, \phi_y)^T \in \mathbb{R}^3$ is the roll/pitch/yaw angles, and $\theta = (\theta_1, \dots, \theta_m)^T \in \mathbb{R}^m$ is the joint angles of the robotic arm.

Define also the translation and rotation Jacobians [46], $J_{v_i}(r) \in \mathbb{R}^{3 \times n}$ and $J_{w_i}(r) \in \mathbb{R}^{3 \times n}$, s.t.,

$$v_j = J_{v_j}(r)\dot{q}, \quad w_j = J_{w_j}(r)\dot{q} \quad (2.1)$$

for $j = 0, 1, \dots, m$, where $v_j, w_j \in \mathbb{R}^3$ are respectively the translation velocity of the mass center and the angular velocity of the j -th link, with $j = 0$ representing the quadrotor platform and $j = 1, \dots, m$ each link of the robot arm. Here, note that the Jacobians J_{v_j}, J_{w_j} are only functions of (fully-actuated) $r := [\phi; \theta] \in \mathbb{R}^{3+m}$ and not (under-actuated) $p = (x, y, z)$.

Using (2.1), we can also construct the QM-system's kinetic energy $\kappa := (1/2)\dot{q}^T M(q)\dot{q}$ with the inertia matrix $M(q) \in \mathbb{R}^{n \times n}$ as given by:

$$M(r) := \sum_{j=0}^m \left[m_j J_{v_j}^T J_{v_j} + J_{w_j}^T R_j I_j R_j^T J_{w_j} \right]$$

where $m_j > 0$ and $I_j > 0$ are the mass and the moment of inertia of the j -th link about their center of mass expressed in their body-fixed frame [46]. Here, note that this $M(q)$ is again only a function of r and not of p , i.e., the QM-system dynamics is symmetric w.r.t. p if no gravity is present. We can

then easily see that the inertia matrix $M(r)$ assumes the following structure:

$$M(r) = \begin{bmatrix} M_p & M_{pr}(r) \\ M_{pr}^T(r) & M_r(r) \end{bmatrix} \quad (2.2)$$

where $M_p = mI_3 \in \mathfrak{R}^{3 \times 3}$, where $m := \sum_{j=0}^m m_j > 0$ is the total mass of the QM-system, with m_o, m_i being the mass of the quadrotor and the j -th arm link.

The QM-system is also under-actuated, that is, $r = [\phi; \theta] \in \mathfrak{R}^{3+m}$ is fully-actuated with the quadrotor's roll/pitch/yaw torque inputs and that for each link of the robot arm, while $p = (x, y, z)^T \in \mathfrak{R}^3$ is under-actuated with only the thrust force input λ , whose direction is fixed to the quadrotor's body-fixed D -direction. More precisely, we can write the control action for the QM system s.t.,

$$\tau = [-\lambda R_o e_3; \tau_{\phi_r}; \tau_{\phi_p}; \tau_{\phi_y}; \tau_1; \dots, \tau_m] \in \mathfrak{R}^n \quad (2.3)$$

where $\lambda \in \mathfrak{R}$ is the thrust force input, $R_o(\phi_r, \phi_p, \phi_y) \in \text{SO}(3)$ is the rotation matrix of the quadrotor parameterized by (ϕ_r, ϕ_p, ϕ_y) , $e_3 = [0; 0; 1]$ is a basis vector representing the D -direction, and $(\tau_{\phi_r}, \tau_{\phi_p}, \tau_{\phi_y})$ and $\tau_i \in \mathfrak{R}$ are respectively the quadrotor's roll/pitch/yaw torques and that of each axis of the manipulator.

The quadrotor-manipulator system is also under the effect of gravity along

the inertial frame's D -direction. We can write this gravitational potential energy by

$$\varphi(q) := - \sum_{j=0}^m m_j g z_j \quad (2.4)$$

where $z_i \in \mathfrak{R}$ is the D -directional position of the j -th link of the QM-system (with $\dot{z} > 0$ implying going down along the D -direction). Using the kinetic energy $\kappa := (1/2)\dot{q}^T M(r)\dot{q}$ and this gravitational potential energy $\varphi(q)$, we can obtain the Lagrange dynamics of the QM-system s.t.,

$$M(r)\ddot{q} + C(r, \dot{r})\dot{q} + g(q) = \tau + f \quad (2.5)$$

where $C(r, \dot{r}) \in \mathfrak{R}^{n \times n}$ is the Coriolis matrix with $\dot{M} - 2C$ being skew-symmetric, $g(q) = \partial\varphi(q)/\partial q \in \mathfrak{R}^n$ is the gravitational force, $\tau \in \mathfrak{R}^n$ is the (under-actuated) control action, and $f \in \mathfrak{R}^n$ is the external force. The inertia matrix $M(r)$ in (3.2) has the following property, which will be instrumental for the ensuing development on the geometric structure of (3.2).

Proposition 1. If we write $M_{pr}(r)$ in (2.2) s.t.,

$$M_{pr}(r) = \begin{bmatrix} c_{\phi_r}^x & c_{\phi_p}^x & c_{\phi_y}^x & c_1^x \cdots c_m^x \\ c_{\phi_r}^y & c_{\phi_p}^y & c_{\phi_y}^y & c_1^y \cdots c_m^y \\ c_{\phi_r}^z & c_{\phi_p}^z & c_{\phi_y}^z & c_1^z \cdots c_m^z \end{bmatrix}$$

the gravity force vector $g(q)$ can also be written as

$$g^T(q) = -[0, 0, m, c_{\phi_r}^z, c_{\phi_p}^z, c_{\phi_y}^z, c_1^z, \cdots, c_m^z]g \quad (2.6)$$

Proof: Recall that the ij -th component of $M(r)$ is given by $\frac{\partial^2 \kappa}{\partial \dot{q}_i \partial \dot{q}_j}$. Therefore, with $M_p = \text{diag}[m, m, m]$, the assertion to prove is equivalent to

$$\frac{\partial^2 \kappa}{\partial \dot{z} \partial \dot{q}_i} = -\frac{1}{g} \frac{\partial \varphi}{\partial q_i}$$

Note also that the Jacobians J_{v_j} and J_{w_j} have the following structures:

$$\begin{aligned} J_{v_j}(r) &= \begin{bmatrix} 1 & 0 & 0 \\ 0 & 1 & 0 & J_{v_j}^{r_1} \dots J_{v_j}^{r_{3+m}} \\ 0 & 0 & 1 \end{bmatrix} \\ J_{w_j}(r) &= \begin{bmatrix} 0 & 0 & 0 \\ 0 & 0 & 0 & J_{w_j}^{r_1} \dots J_{w_j}^{r_{3+m}} \\ 0 & 0 & 0 \end{bmatrix} \end{aligned} \quad (2.7)$$

Therefore,

$$\frac{\partial^2 \kappa}{\partial \dot{z} \partial \dot{q}_i} = \frac{1}{2} \frac{\partial^2}{\partial \dot{z} \partial \dot{q}_i} \sum_{j=0}^m m_j \dot{q}^T J_{v_j}^T J_{v_j} \dot{q} \quad (2.8)$$

since terms with J_{w_j} in the kinetic energy κ do not contain \dot{z} , thus, will disappear by the partial differentiation w.r.t. \dot{z} . Moreover, from (2.7), we have

$$J_{v_j} \dot{q} = \begin{pmatrix} \dot{x} \\ 0 \\ 0 \end{pmatrix} + \begin{pmatrix} 0 \\ \dot{y} \\ 0 \end{pmatrix} + \begin{pmatrix} 0 \\ 0 \\ \dot{z} \end{pmatrix} + \sum_{k=1}^{3+m} J_{v_j}^{r_k} \dot{r}_k$$

thus, we can write: with $J_{v_j}^{q_i} \in \mathbb{R}^3$ being the i -th column vector of J_{v_j} ,

$$\frac{\partial^2 \kappa}{\partial \dot{z} \partial \dot{q}_i} = \frac{\partial^2}{\partial \dot{z} \partial \dot{q}_i} \left[\sum_{j=0}^m \sum_{i=1}^n m_j \begin{pmatrix} 0 \\ 0 \\ \dot{z} \end{pmatrix}^T J_{v_j}^{q_i} \dot{q}_i \right] = \sum_{j=0}^m m_j e_3^T J_{v_j}^{q_i}$$

since, again, only the terms both with \dot{z} and \dot{q}_i can survive the operation $\frac{\partial^2}{\partial \dot{z} \partial \dot{q}_i}$.

On the other hand, time derivative of the gravity potential $\varphi(q)$ in (2.4) can be computed s.t.,

$$\frac{d\varphi}{dt} = \frac{\partial \varphi}{\partial q} \dot{q} = - \sum_{j=0}^m m_j g \dot{z}_j = - \sum_{i=1}^n \sum_{j=0}^m m_j g e_3^T J_{v_j}^{q_i} \dot{q}_i$$

where we use $\dot{z}_j = e_3^T J_{v_j} \dot{q} = e_3^T \sum_{i=1}^n e_3^T J_{v_j}^{q_i} \dot{q}_i$. This then implies that

$$\frac{\partial \varphi}{\partial q_i} = - \sum_{j=0}^m m_j g e_3^T J_{v_j}^{q_i}$$

which completes the proof. ■

2.3 Passive Decomposition of Quadrotor-Manipulator System

We apply passive decomposition [37, 38] to exhibit a peculiar underlying structure of the QM-system dynamics, which can be used in control design or analysis purpose. This property is in fact also shared by many platform-manipulator

systems (e.g., spacecraft with robotic manipulator, thrust-propelled underwater vehicle with robot arm, etc). Following [39], we first define the shape map $h(q) := r$, that is, the “internal rotation” with full-actuation. Then, we can split the tangent space of the QM-system s.t.,

$$\begin{aligned}\Delta^\top &:= \{\dot{q} \in \mathbb{R}^n | \mathcal{L}_{\dot{q}}h(q) = \mathcal{L}_{\dot{q}}r = 0\} = \text{null}(\partial r / \partial q) \\ \Delta^\perp &:= \{v \in \mathbb{R}^n | v^T M(q) \xi = 0, \forall \xi \in \Delta^\top\}\end{aligned}$$

where $\mathcal{L}_{\dot{q}}h(q)$ is the Lie derivative of $h(q)$ along \dot{q} . This then implies that the tangent space splits s.t.,

$$T_q\mathcal{M} = \Delta^\top \oplus \Delta^\perp \quad (2.9)$$

where 1) Δ^\top is called *tangential distribution* (i.e., parallel to the level set of $h(q)$) and the QM-system dynamics projected on this is called *locked system* dynamics, whereas 2) Δ^\perp is called *normal distribution* (i.e., orthogonal complement of Δ^\top w.r.t. the inertia matrix $M(q)$) and the QM-system dynamics on this Δ^\perp is called *shape system* dynamics.

In coordinates, following [39], since Δ^\top can be identified by \dot{p} while Δ^\perp should span the tangent space of r , we can write this decomposition (2.9) s.t.,

$$\dot{q} = \begin{bmatrix} \Delta_\top & \Delta_\perp \end{bmatrix} \begin{pmatrix} \nu_L \\ \dot{r} \end{pmatrix} := \underbrace{\begin{bmatrix} I_3 & T(r) \\ 0 & I_{n-3} \end{bmatrix}}_{=:S(r)} \nu \quad (2.10)$$

where $\Delta_\top = [I_3; 0] \in \mathbb{R}^{n \times 3}$ and $\Delta_\perp = [T(r); I_{n-3}] \in \mathbb{R}^{n \times n-3}$ are matrices

respectively identifying Δ^\top and Δ^\perp , and $\nu_L \in \mathbb{R}^3$, which describes the center-of-mass motion of the QM-system to be shown below.

Lemma 1. If we write $T(r)$ s.t.,

$$T(r) = \begin{bmatrix} a_{\phi_r}^x & a_{\phi_p}^x & a_{\phi_y}^x & a_1^x \cdots a_m^x \\ a_{\phi_r}^y & a_{\phi_p}^y & a_{\phi_y}^y & a_1^y \cdots a_m^y \\ a_{\phi_r}^z & a_{\phi_p}^z & a_{\phi_y}^z & a_1^z \cdots a_m^z \end{bmatrix}$$

$ma_{r_i}^j = -c_{r_j}^i$, where $c_{r_j}^i$ is the ji -th element of $M_{pr}(r)$ in Prop. 1.

Proof: From the passive decomposition (2.9), the tangential and the normal distributions are orthogonal with each other w.r.t. $M(q)$ metric, that is,

$$[I_3 \quad 0]M(r) \begin{bmatrix} T(r) \\ I_{n-3} \end{bmatrix} = M_p T(r) + M_{pr} = 0$$

implying that

$$T(r) = -M_p^{-1}M_{pr}$$

where $M_p = mI_3$ is a positive and diagonal definite matrix. ■

Applying this passive decomposition to (3.2), we now reveal an underlying structure of the QM-system dynamics, namely, its dynamics can be completely decoupled into the translational center-of-mass dynamics of ν_L and the internal rotational dynamics of r , where the former has the form of the thrust propelled vehicle dynamics (e.g., quadrotor) with the under-actuation and the gravity effect showing up; whereas the latter has the form of the usual Lagrange dynamics of robotic manipulator with full-actuation.

Proposition 2. Applying the passive decomposition (2.9), we can transform the QM-system dynamics (3.2) into:

$$M_L \dot{\nu}_L + g_L = \tau_L \quad (2.11)$$

$$M_E(r) \ddot{r} + C_E(r, \dot{r}) \dot{r} = \tau_E \quad (2.12)$$

where

1. Locked system (2.11) describes the center-of-mass dynamics of the QM-system with $\nu_L = \dot{p}_{\text{CoM}}$, $M_L = mI_3$, $g_L(q) = -[0; 0; mg] \in \mathbb{R}^3$ and $\tau_L = \lambda R_o(\phi)$
2. Shape system (2.12) describes the rotational dynamics of r of the QM-system with positive and symmetric $M_E \in \mathbb{R}^{(3+m) \times (3+m)}$, skew-symmetric $\dot{M}_E - 2C_E$ and fully-actuated $\tau_E \in \mathbb{R}^{3+m}$.

Proof: The assertions on M_L, M_E and the skew-symmetry of $\dot{M}_E - 2C_E$ can be easily shown if we rewrite the dynamics (3.2) using $\dot{q} = S\nu$ (and $\ddot{q} = S\dot{\nu} + \dot{S}\nu$) with

$$\begin{bmatrix} M_L & 0 \\ 0 & M_E \end{bmatrix} := S^T M(r) S$$

$$\begin{bmatrix} C_L & C_{LE} \\ C_{EL} & C_E \end{bmatrix} := S^T [M(r) \dot{S} + C(r, \dot{r}) S]$$

with $\dot{M}_L - 2C_L$ and $\dot{M}_E - 2C_E$ both being skew-symmetric, and $C_{EL} = -C_{LE}^T$. See [37] for more details.

The assertions on τ_L, τ_E can also be shown by seeing

$$[\tau_L; \tau_E] := S^T(r)\tau$$

where τ is given in (3.1) with $\tau_{\phi_r}, \tau_{\phi_p}, \tau_{\phi_y}$ and $\tau_i, i = 1, 2, \dots, m$, all arbitrarily assignable. The assertion on $g_L(q)$ and the absence of the gravity in the shape dynamics (2.12) can be proved from

$$[g_L, g_E] := S^T(r)g(q)$$

where $q_L = \begin{bmatrix} I_3 & 0_{3 \times (3+m)} \end{bmatrix} g(q) = -[0; 0; mg]$ from (2.6); and also $q_E = \begin{bmatrix} T^T(r) & I_{3+m} \end{bmatrix} g(q) = 0$ with the i -th component of q_E given by

$$(a_{r_i}^x, a_{r_i}^y, a_{r_i}^z, \underbrace{0, \dots, 0, 1, 0, \dots, 0}_{i\text{-th } 1})g(q) = -mga_i^z - c_{r_i}^z = 0$$

from Prop. 1 with the expression of $g(q)$ given in (2.6).

The center-of-mass position is given by

$$mp_{\text{CoM}} = m_o p + \sum_{j=1}^m m_j p_j$$

where p is the quadrotor's center-of-mass and p_j is that of the j -th link of the robot arm. Then,

$$m\dot{p}_{\text{CoM}} = m_o \dot{p} + \sum_{j=1}^m m_j \dot{p}_j = \sum_{j=0}^m m_j \sum_{i=1}^n J_{v_j}^{q_i} \dot{q}_i$$

from (2.1). If we extract only the x -component of \dot{p}_{CoM} , we have

$$m\dot{p}_{\text{CoM}}^x = \sum_{i=1}^n \sum_{j=0}^m m_j e_1^T J_{v_j}^{q_i} \dot{q}_i = m\dot{x} + \sum_{i=1}^{3+m} c_{r_i}^x \dot{r}_i$$

where we use the facts that $\sum_{j=0}^m m_j e_1^T J_{v_j}^{q_i} = m$ and $e_1^T J_{v_j}^{q_i} = 0$ for $i = 2, 3$. If we collect the similar results for $m\dot{p}_{\text{CoM}}^y$ and $m\dot{p}_{\text{CoM}}^z$ and use Lem. 1, we can then achieve

$$m\dot{p}_{\text{CoM}} = m\dot{p} - mT(r)\dot{r}$$

which implies that $\dot{p}_{\text{CoM}} = \nu_L$, since $\dot{p} = \nu_L + T(r)\dot{r}$ from (2.10).

Lastly, note that the first row of the Lagrange dynamics (3.2) can be written as

$$m\ddot{x} + \sum_{i=1}^{3+m} c_{r_i}^x \ddot{r}_i + \sum_{i=1}^n \sum_{j=1}^n \frac{1}{2} \left(\frac{\partial c_j^x}{\partial q_i} + \frac{\partial c_i^x}{\partial q_j} - \frac{\partial c_j^i}{\partial x} \right) \dot{q}_i \dot{q}_j = \tau_1$$

where τ_1 is the first component of τ , $c_j^x = m_{1j}$ and $c_j^i = m_{ij}$, and the term $\sum_{i,j=1}^n \frac{1}{2} \left(\frac{\partial c_j^x}{\partial q_i} + \frac{\partial c_i^x}{\partial q_j} - \frac{\partial c_j^i}{\partial x} \right) \dot{q}_i \dot{q}_j$ is the Coriolis term [46], where $\partial c_j^i / \partial x = 0$, since $M(r)$ is a function of r only. We can further simplify

$$\sum_{i,j=1}^n \frac{1}{2} \left(\frac{\partial c_j^x}{\partial q_i} + \frac{\partial c_i^x}{\partial q_j} \right) \dot{q}_i \dot{q}_j = \sum_{i,j=1}^n \frac{\partial c_j^x}{\partial q_i} \dot{q}_i \dot{q}_j = \sum_{i=1}^{3+m} \frac{dc_{r_i}^x}{dt} \dot{r}_i$$

due to the symmetry in i and j , $c_j^x = 0$ for $k = 2, 3$ (since $M_p = mI_3$) and $\partial c_j^i / \partial q_i = 0$, $i = 1, 2, 3$ from $M(r)$ being a function of only r . Then, the above dynamics equation can be rewritten as

$$m\ddot{x} + \sum_{i=1}^{3+m} c_{r_i}^x \ddot{r}_i + \sum_{i=1}^{3+m} \frac{dc_{r_i}^x}{dt} \dot{r}_i = \tau_1 \quad (2.13)$$

with a similar also hold for the dynamics of \ddot{y}, \ddot{z} .

Recall from (2.10) with Lem. 1 that

$$m\nu_L^x = m\dot{x} + \sum_{i=1}^{3+m} c_{r_i}^x \dot{r}_i$$

the differentiation of which with (2.13) then becomes

$$m\dot{\nu}_L^x = \tau_1 \tag{2.14}$$

with a similar hold for ν_L^y and ν_L^z . This then means that the center-of-mass dynamics is given by the locked system dynamics (2.11) with no Coriolis terms therein (i.e., $C_L = 0$ and $C_{LE} = 0$). This also means that $C_{EL} = -C_{LE}^T = 0$ as well (see [37] for more details on this condition). This completes the proof. ■

Therefore, although often seemingly overwhelmingly complicated in its original Lagrange dynamics form (3.2), the QM-system dynamics possesses the underlying structure as manifested in (2.11)-(2.12) with the following interesting properties:

- It is in fact a combination of the center-of-mass translation dynamics of ν_L and the internal rotational dynamics of r ;
- The ν_L -dynamics is, similar to, e.g., the quadrotor dynamics [5], just a point-mass dynamics with body-fixed thrust force input;
- The \dot{r} -dynamics is similar to the standard Lagrange dynamics of the fully-actuated serial-link robot manipulator;

- Gravity effect and the under-actuation affect only along the ν_L -dynamics direction and completely decoupled from the \dot{r} -dynamics;
- The ν_L -dynamics and the \dot{r} -dynamics are completely decoupled from each other, with neither acceleration coupling nor Coriolis coupling.

Note also that this underlying structure (2.11)-(2.12) is universally applicable to many practically important systems, which consist of a moving/flying platform with robotic arm attached on it (e.g., spacecraft with robotic manipulator, thrust propelled underwater vehicle with robot arm, etc.). This decomposition (2.11)-(2.12) would also facilitate control design procedure, since, for instance, we can design control laws for the center-of-mass motion and the internal rotational motion, separately and individually. In the next Sec. 2.4, we present a trajectory tracking control framework, whose design is facilitated by our passive decomposition result as provided above.

2.4 Trajectory Tracking Control Design

The structure identified above would facilitate control design for otherwise typically very complicated dynamics of the QM-system (3.2). Although other control objectives would be possible, here, as a first step to utilize this underlying structure of the QM-system, we focus on the trajectory tracking of the end-effector, which is perhaps the most basic control objective among others. For this, let us first denote by $p_e := (x_e, y_e, z_e) \in \mathbb{R}^3$ the end-effector Cartesian position expressed in the inertial NED-frame. We can then establish a forward kinematic relation between p_e and q , and, furthermore, can obtain its Jacobian

relation in the following form s.t.,

$$\dot{p}_e = \begin{bmatrix} I_3 & A(r) \end{bmatrix} \dot{q} = \nu_L + B(r)\dot{r} \quad (2.15)$$

where $A(r) \in \mathbb{R}^{3 \times (3+m)}$ and we use $\dot{q} = S(r)\nu$ in (2.10) with $B(r) := A(r) + T(r)$.

For the trajectory tracking of the end-effector, we then want $\dot{p}_e = \dot{p}_e^d - k(p_e - p_e^d)$ where $k > 0$ is a constant control gain. From this relation, we can further define the desired value for ν_L^d s.t.,

$$\nu_L^d := \dot{p}_e^d - k(p_e - p_e^d) - B(r)\dot{r} \quad (2.16)$$

Of course, in general, $\nu_L \neq \nu_L^d$. Define $e_L := \nu_L - \nu_L^d$. Then, using (2.15), we can obtain

$$\dot{e}_p + k e_p = e_L \quad (2.17)$$

where $e_p := p_e - p_e^d$. Here, note that, if $e_L \rightarrow 0$, $e_p \rightarrow 0$ exponentially. The above relation then naturally give a rise to the following backstepping-like control generation equation.

Theorem 1. Consider the locked and shape systems (2.11)-(2.12). Then, we will have $(e_p, e_L) \rightarrow 0$ exponentially, if we set τ_L, τ_E s.t.,

$$\begin{aligned} \tau_L + M_L B \ddot{r} = \\ -\gamma e_p - \alpha e_L + g_L + M_L [\ddot{p}_d - \lambda \dot{e}_p - \frac{dB}{dt} \dot{r}] \end{aligned} \quad (2.18)$$

where $\gamma, \alpha, \lambda > 0$ are constant.

Proof: Define

$$V_1 = \frac{1}{2}e_p^T e_p$$

Then, from (2.17), we have

$$\frac{dV_1}{dt} = -ke_p^T e_p + e_p^T e_L$$

Following the backstepping procedure, let us augment V_1 s.t.,

$$V_2 = \frac{1}{2}e_p^T e_p + \frac{1}{2\gamma}e_L^T M_L e_L \quad (2.19)$$

with $\gamma > 0$. Then, Time derivative of V_2 is represented as following

$$\begin{aligned} \frac{dV_2}{dt} &= -ke_p^T e_p + e_p^T e_L + \frac{1}{\gamma}e_L^T M_L \dot{e}_L \\ &= -ke_p^T e_p + e_p^T e_L + \frac{1}{\gamma}e_L^T [\tau_L - g_L(q) - M_L \dot{\nu}_L^d] \\ &= -ke_p^T e_p + \frac{1}{\gamma}e_L^T M_L B M_E^{-1} [\tau_E - C_E \dot{r}] \\ &\quad + \frac{1}{\gamma}e_L^T [\gamma e_p + \tau_L - g_L - M_L (\ddot{p}_d - k\dot{e}_p - \frac{dB}{dt}\dot{r})] \end{aligned}$$

from (2.11) and (2.16), where the term $M_E^{-1}(\tau_E - C_E \dot{r}) = \ddot{r}$ comes from (2.12).

Thus, by plugging (2.18) into this, we can obtain

$$\frac{dV_2}{dt} = -ke_p^T e_p - \frac{\alpha}{\gamma}e_L^T e_L \leq 0 \quad (2.20)$$

implying that $(e_p, e_L) \rightarrow 0$ exponentially. ■

Note that the control generation equation (2.18) would be in general a redundant equation, that is, even though we have 1-DOF control $\tau_L = \lambda R_o(\phi)$, we also have $(3 + m)$ -DOF control τ_E . This then further implies a possibility to assign control actions across τ_L and τ_E depending on the task objective. For instance, if the task is simply a transport, it would be more proper to assign more control action on τ_L , while making that for τ_E only complementary. Or, if the task is a precise motion control with the platform almost stationary, τ_L would need to compensate for the gravity $g_L(q)$, while the other precise motion control action is assigned to τ_E . How to assign (and consequently design) control actions for τ_L and τ_E , given a task objective, is a very interesting topic and we spare it for future research.

Here, note that, due to the issue of under-actuation, we cannot assign τ_L arbitrarily. One way to choose $\tau_L = \lambda R_o(\phi)$ for the end-effector trajectory tracking task is to choose λ, ϕ_d s.t.,

$$\begin{aligned}\tau_L &= \lambda R_o(\phi_d) \\ &= \gamma e_p - \alpha e_L + G_L + M_L[\ddot{p}_d - \lambda \dot{e}_p - \frac{dB}{dt}\dot{r} - \zeta(r)]\end{aligned}\tag{2.21}$$

where $\zeta(r)$ is a function to encode a certain sub-task for r -motion under the end-effector trajectory tracking, whereas the inclusion of $\frac{dB}{dt}\dot{r}$ is to avoid a certain undesirable behavior incurred due to internal dynamics [27, 28] (e.g., $r \rightarrow 0$ even with $(e_p, e_L) \rightarrow 0$: the topic of this internal dynamics is beyond the scope of this thesis and will be reported in a future publication).

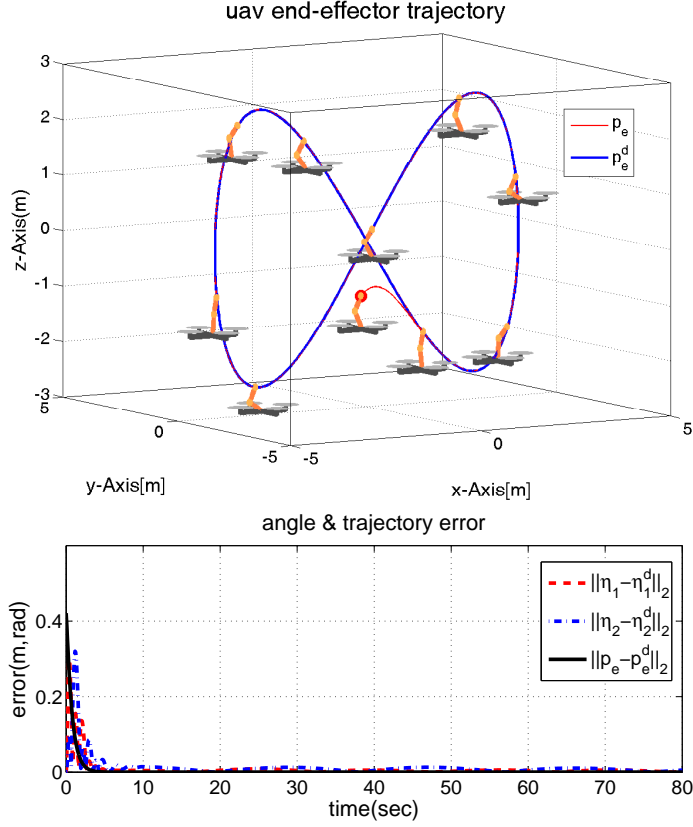


FIGURE 2.2: Snapshots of end-effector trajectory tracking of a planar quadrotor with 2-DOF arm with error convergence. Here, $\eta_1 = \phi + \theta_1 + \theta_2$ and $\eta_2 = \phi + \theta_1$

We also choose τ_E s.t.,

$$\begin{aligned}
 M_L B(r) \ddot{r} &= M_L B(r) [\tau_E - C_E(r, \dot{q}) \dot{r}] = \\
 &= -\gamma e_p - \alpha e_L + g_L + M_L [\ddot{p}_d - \lambda \dot{e}_p - \frac{dB}{dt} \dot{r}] - \tau_L
 \end{aligned} \tag{2.22}$$

where $\tau_L = \lambda R_o(\phi)$ (not $\lambda R_o(\phi_d)$). This then means that, even if τ_L , due to the under-actuation, does not precisely satisfy its control generation equation (3.7), the condition (2.18) is still ensured and so is the exponential convergence

of $(e_p, e_L) \rightarrow 0$. Now, suppose that the τ_L -generation (3.7) is achieved. Then, from (2.18), we have

$$B\ddot{r} = B(\tau_E - C_E\dot{r}) = \zeta(r) \quad (2.23)$$

This then implies that $\zeta(r)$ can encode a certain sub-task objective for the r -motion while still enforcing the end-effector trajectory tracking control. One such a sub-task example is

$$\zeta(r) = B\{\ddot{r}_d - k_d(\dot{r} - \dot{r}_d) - k_p(r - r_d)\} \quad (2.24)$$

to drive $r \rightarrow r_d$ while enforcing end-effector tracking. We may also include other sub-task objectives in this $\zeta(r)$ (e.g., maximization of manipulability), the details of which will be reported in a future publication. Note also that $B(r) \in \mathbb{R}^{3 \times (3+m)}$ in the τ_E -control generation equation (3.8) is a fat matrix. That means that $B(r)$ assumes a non-trivial nullspace, and any motion in that nullspace can be used to achieve another control objective in addition to the trajectory tracking and the sub-task for the r -motion, although, in this case, this sub-task will be limited only to the motion outside that nullspace.

We apply this control law to the end-effector trajectory tracking control for a quadrotor with 2-DOF arm, whose motion is constrained on its sagittal plane, and the result is shown in Fig. 2.2, where the trajectory is given by $x_e^d = 4 \sin t/5$, $y_e^d = -2.5 \sin(t/4)$ and the sub-task desired manipulator configuration r_d is given as $\phi + \theta_1 + \theta_2 = -2\pi/3 + 0.6 \sin t/6$, $\phi + \theta_1 = -\pi/3 + 0.3 \sin t/5$. The null-space motion as given by $\dot{\phi} = -\dot{\theta}_1$ is used to attain the desired pitch angle ϕ_d to align τ_L according to (3.7). We also perform another simulation,

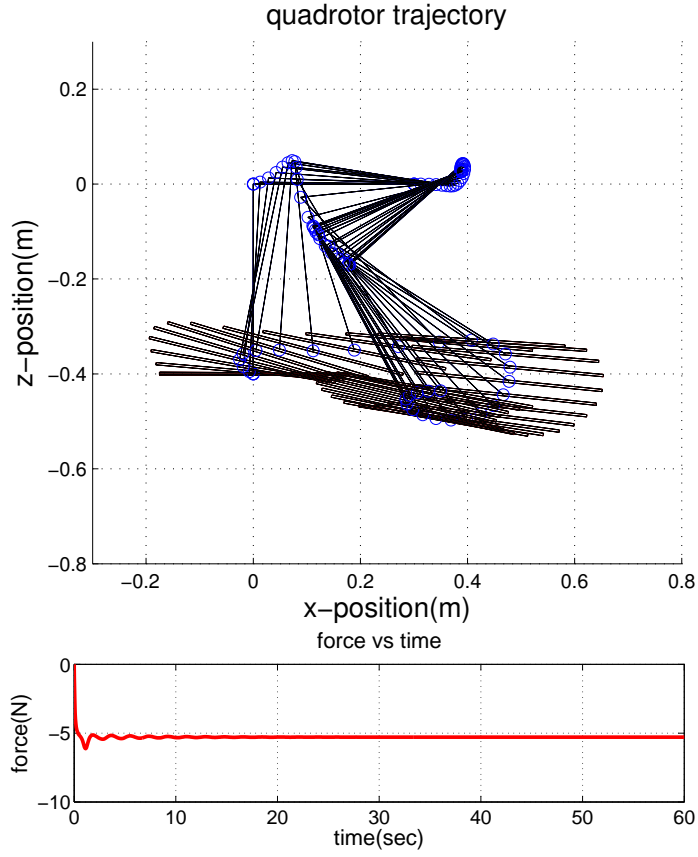


FIGURE 2.3: Snapshots of the quadrotor-manipulator system under admittance-type force control with force profile.

where, assuming that a force sensor is available, an admittance-type force control is implemented for the end-effector with a visco-elastic virtual wall. See Fig. 2.3 for the result.

2.5 Conclusion

In this chapter, we reveal a certain underlying structure of the nonlinear Lagrange dynamics of the quadrotor-manipulator (QM) system, that is, its dynamics, although often overwhelmingly complex, can be completely split into: 1) the quadrotor-like center-of-mass dynamics in $E(3)$ with all under-actuation and gravity effect; and 2) the “internal” dynamics of quadrotor’s rotation and the manipulator configuration in the form of standard Lagrange dynamics with full actuation and no gravity effect. Relying on this structure, we propose a backstepping-like end-effector trajectory tracking control law, which allows for different control authority for each of these systems according to task objectives by exploiting the redundancy inherent in the system. Simulation using a planar quadrotor with a 2-DOF arm for trajectory tracking and force control is also performed to verify the proposed theoretical framework.

Chapter 3

Cooperative Hierarchical Control of Multiple Drone-Manipulator Systems

3.1 Introduction

The multi-rotor drone platform has attracted extensive attention from researchers in the academia and the industry alike, with many strong results proposed particularly for the motion control of the quadrotors [2–5, 47]. Although many number of useful applications (e.g., aerial photography, surveillance, entertainment, etc.), this pure motion control of the quadrotor is restricted to “passive tasks” with no physical interaction with objects or external environments, and we believe that, to be truly a versatile robotic platform, it is necessary to endow this quadrotor platform with the ability of manipulation and/or physical interaction.

Some attempts have been made along this line, particularly utilizing simple interacting/manipulating mechanisms to circumvent the quadrotor’s limited payload (typically few hundreds grams), e.g.,: 1) operation using a simple un-actuated tool (e.g., screw-driver) attached on the quadrotor [27, 28]; 2)

operation using a simple gripper attached on the quadrotor[24]; and 3) payload transport using cable attached to the quadrotor was proposed in [23]. Although promising in terms of its mechanical simplicity and light weight, such simple tool, gripper or cable, yet, can only provide limited manipulation capability due to the lack of their actuation.

Aiming for dexterous aerial manipulation, quadrotor-manipulator (QM) systems have been recently considered (e.g., [29–33, 48]). See Fig. 2.1. One of the key challenges in deploying this QM system is that its dynamics is fairly complicated with large degree-of-freedom (DOF) and the nonlinear dynamic quadrotor-manipulator coupling, while the control design itself is also hindered by the under-actuation of the quadrotor platform. Perhaps, due to this difficulty, majority of the QM system control results either considered the quadrotor and the manipulator separately with their dynamic coupling considered as disturbance (e.g., [29, 30]); or simplified the QM system to be fully-actuated kinematic/dynamic systems while not explicitly taking into account the quadrotor’s under-actuation into their control design (e.g., [31, 48]). To address this dynamic complexity, in [40], we revealed that, albeit seemingly complicated, the QM system dynamics is in fact composed of the *completely-decoupled* centroid translation dynamics and the internal (or shape) dynamics (of the quadrotor’s rotation and the manipulator’s joint angles), with the former assuming the form of the standard under-actuated quadrotor dynamics and the latter the form of the standard fully-actuated robot dynamics (with no gravity). Exploiting this decomposition, in [40], we could also design a backstepping end-effector tracking control in a fairly straightforward fashion.

This QM system, yet, if deployed alone, would still suffer from the problem

of limited payload (e.g., for AscTec[®] Pelican with 500g manipulator, remaining payload would be only around 100g). Multiple cooperative QM systems would then resolve this payload problem while also providing redundancy and manipulability unattainable by a single QM system. Results on these multiple cooperative QM systems, however, are very rare, perhaps due to the aforementioned dynamics complexity of even a single QM system. In fact, to our knowledge, all the results on aerial cooperative manipulation have been restricted to the quadrotors equipped only with simple tool, gripper or cable with some of them even assuming the quadrotors to be quasi-static (e.g., [49], [22, 50], [51]).

In this thesis, standing upon our recent result on the dynamics and control of the single QM system [40], we propose a novel hierarchical cooperative control framework for multiple dynamic QM systems, which can endow the cooperatively-grasped object with an user-specific target behavior according to various task objective. Our proposed control framework is hierarchical and also modular with the following layers/sub-modules (see Fig. 3.1):

- **Object behavior design**, which computes the required wrench for the cooperatively-grasped object to achieve the user-specific target behavior according to task objectives (e.g., trajectory tracking, velocity-field following, compliant interaction, etc.);
- **Optimal cooperative force distribution**, which optimally assign contact force of each QM system to cooperatively achieve the desired object behavior, while minimizing a certain cost function and respecting the friction-cone constraints to prevent slippage; and

- **Individual QM system control**, which extends the end-effector position control of [40] for the admittance-type contact force control of each QM system with unknown object stiffness model and force sensor/estimator [41], while also explicitly taking into account the different dynamics characteristics of the (slower/coarse) quadrotor and the (faster/fine) manipulator.

3.2 Preliminary

3.2.1 Dynamics Modeling of QM System

In this chapter, we deal with the cooperation of N QM systems, each with multi-DOF serial-link manipulator. See Fig. 2.1. The configuration of a single QM system can then be given by

$$q := [p; \phi; \theta] \in \mathbb{R}^n, \quad n := 6 + m$$

where $p = [x; y; z] \in \mathbb{R}^3$ is the quadrotor platform's center-of mass in the inertial NED-frame, $\phi = [\phi_r; \phi_p; \phi_y] \in \mathbb{R}^3$ is the roll/pitch/yaw angles of the quadrotor, and $\theta = [\theta_1; \dots; \theta_m] \in \mathbb{R}^m$ is the joint angles of the manipulator.

The QM-system is under-actuated, that is, the control action for the QM-system is given by

$$\tau = [-\lambda Re_3; \tau_{\phi_r}; \tau_{\phi_p}; \tau_{\phi_y}; \tau_1; \dots; \tau_m] \in \mathbb{R}^n \quad (3.1)$$

where $\lambda \in \mathfrak{R}$ is the thrust force, $R(\phi_r, \phi_p, \phi_y) \in \text{SO}(3)$ is the rotation matrix of the quadrotor parameterized by (ϕ_r, ϕ_p, ϕ_y) , $e_3 = [0; 0; 1]$ is a basis vector representing the D -direction, and $(\tau_{\phi_r}, \tau_{\phi_p}, \tau_{\phi_y})$ and $\tau_i \in \mathfrak{R}$ are respectively the quadrotor's roll/pitch/yaw torques and that of each manipulator joints. $r = [\phi; \theta] \in \mathfrak{R}^{3+m}$ is fully-actuated with the torque input $(\tau_{\phi_r}, \tau_{\phi_p}, \tau_{\phi_y})$ and τ_i , while $p = [x; y; z] \in \mathfrak{R}^3$ is under-actuated with only the thrust force input λ , whose direction is fixed to the quadrotor body-fixed D -direction.

From the kinetic energy $\kappa = \frac{1}{2} \dot{q}^T M(r) \dot{q}$, where $M(r) \in \mathfrak{R}^{n \times n}$ is inertia matrix, and the gravitational potential energy $\varphi(q)$, Lagrange dynamics of the QM-system is given by

$$M(r)\ddot{q} + C(r, \dot{r})\dot{q} + g(r) = \tau + f \quad (3.2)$$

where $C(r, \dot{r}) \in \mathfrak{R}^{n \times n}$ is the Coriolis matrix with $\dot{M} - 2C$ being skew-symmetric, $g(q) = \partial\varphi(q)/\partial q \in \mathfrak{R}^n$ is the gravitational force, $\tau \in \mathfrak{R}^n$ is the control action (3.1), and $f \in \mathfrak{R}^n$ is the external disturbance. Note that inertia matrix $M(r)$ is only a function of r due to symmetry in $E(3)$, thus dynamics is symmetric w.r.t. p if no gravity is present.

3.2.2 Dynamics Decomposition and Control of QM System

In [40], we showed that the QM system dynamics (3.2) is in fact composed of the following two decoupled dynamics:

$$m_L \ddot{p}_L + g_L = \tau_L + f_L \quad (3.3)$$

$$M_E(r) \ddot{r} + C_E(r, \dot{r}) \dot{r} = \tau_E + f_E \quad (3.4)$$

where $p_L \in \mathbb{R}^3$ is the center-of-mass position of the total QM system with $m_L > 0$ being its mass; $r = [\phi; \theta]$ is the internal rotation with $M_E(r)$, $C_E(r, \dot{r}) \in \mathbb{R}^{(3+m) \times (3+m)}$ being its inertia and Coriolis matrices respectively with skew-symmetric $\dot{M}_E - 2C_E$; $g_L \in \mathbb{R}^3$ is the gravity vector, $\tau_L = -\lambda R e_3 \in \mathbb{R}^3$ and $\tau_E \in \mathbb{R}^{3+m}$ are the (under-actuated) thrust input for p_L and the fully-actuated control for r ; and $f_L \in \mathbb{R}^3$, $f_E \in \mathbb{R}^{3+m}$ are transformed external disturbances.

This dynamics decomposition (3.3)-(3.4) possesses the following remarkable properties: 1) the two dynamics are completely decoupled from each other with no inertial, Coriolis and gravity couplings; 2) the center-of-mass p_L dynamics (3.3) has the form of the standard under-actuated quadrotor dynamics with $\tau_L = -\lambda R e_3$; 3) the internal rotation dynamics (3.4) has the form of the standard fully-actuated manipulator dynamics; and 4) gravity effect shows up only in (3.3) and not in (3.4). This decomposition structure (3.3)-(3.4) turns out to hold for general vehicle-manipulator systems (e.g., underwater ROV with arm, space robot equipped with manipulator, etc.). This decomposition (3.3)-(3.4) also generalizes the concept of virtual manipulator in [52] to the case with the gravity.

In [40], exploiting the dynamics decomposition (3.3)-(3.4), we proposed a trajectory tracking control for the QM system's end-effector position $p_e \in \mathbb{R}^3$, which can be written as

$$\dot{p}_e = \dot{p}_L + B(r)\dot{r} \quad (3.5)$$

where p_L and r are respectively the QM system center-of-mass position and the internal rotation, whose dynamics are decoupled in (3.3)-(3.4), and $B(r) \in$

$\mathfrak{R}^{3 \times (m+3)}$ is a Jacobian-like matrix from \dot{r} to \dot{p}_e with the inertial parameters embedded in it. Then, differentiating (3.5) and individually incorporating (3.3)-(3.4), in [40], we could design the control generation equation to achieve $p_e \rightarrow p_e^d$ s.t.,

$$\begin{aligned} \tau_L + m_L B M_E^{-1} [\tau_E - C_E \dot{r}] = \\ -\gamma e_p - \alpha e_L + g_L + m_L [\ddot{p}_e^d - k \dot{e}_p - \frac{dB}{dt} \dot{r}] \end{aligned} \quad (3.6)$$

where $\gamma, \alpha, k > 0$ are control gains, $e_p := p_e^d - p_e$, and $e_L := \dot{p}_L^d - \dot{p}_L$ with $\dot{p}_L^d := \dot{p}_e^d + k(p_e^d - p_e) - B(r)\dot{r}$. Satisfying this control equation (3.6) then guarantees that $(e_p, e_L) \rightarrow 0$ exponentially [40].

In the control generation equation (3.6), $\tau_L = -\lambda R e_3$ cannot be arbitrarily assigned due to the under-actuation. However, $\tau_E \in \mathfrak{R}^{m+3}$ is fully-actuated, thus, similar to the case of redundancy resolution, can be utilized to satisfy (3.6) even with the under-actuated τ_L . Exploiting this redundancy, in [40], we suggest to allocate the control to τ_L and τ_E s.t.,

$$\tau_L^d = -\gamma e_p - \alpha e_L + g_L + m_L [\ddot{p}_e^d - k \dot{e}_p - \frac{dB}{dt} \dot{r} - \zeta(r)] \quad (3.7)$$

$$\begin{aligned} m_L B M_E^{-1} [\tau_E - C_E \dot{r}] \\ = -\gamma e_p - \alpha e_L + g_L + m_L [\ddot{p}_e^d - k \dot{e}_p - \frac{dB}{dt} \dot{r}] - \tau_L \end{aligned} \quad (3.8)$$

where, in (3.7), τ_L^d is the desired thrust input, whereas, in (3.8), τ_E is set to satisfy the control equation (3.6) even if $\tau_L \neq \tau_L^d$ due to the under-actuation, while τ_E in the nullspace of $B M_E^{-1}$ is utilized to align the quadrotor orientation to that of τ_L^d . Also, in steady-state with $\tau_L \rightarrow \tau_L^d$, we have, from

(3.7)-(3.8), $m_L B(r) \ddot{r} \rightarrow \zeta(r)$, which can encode a certain sub-task (e.g., singularity avoidance, etc.). This control allocation (3.7)-(3.8) then allows us to achieve the end-effector trajectory tracking $p_e \rightarrow p_e^d$ even in the presence of under-actuation with $\tau_L \rightarrow \tau_L^d$ and the steady-state sub-task $\zeta(t)$.

For our hierarchical cooperative control framework, in Sec. 3.3, we will extend this position control (3.6) to enable each QM system to exert their desired contact force by using (uncertain) object stiffness model and force sensing/estimator, while also explicitly incorporating slower/coarse quadrotor dynamics and faster/fine manipulator dynamics.

3.3 Hierarchical Control Framework for Multiple QM Systems

For the cooperative control of multiple QM systems, here, we adopt an hierarchical and modular approach, where an hierarchy is constructed from the highest-level task (i.e., object behavior design such as object transport or compliant interaction between the grasped object and external environment) to the middle-level task (i.e., optimal distribution of the resultant object wrench for generating the target object behavior to each QM system's end-effector) and to the lowest-level task (i.e., individual QM system admittance-type end-effector force control to realize the optimally-assigned contact force), while also each layer can be modified/replaced according to task objectives. See Fig. 3.1. In the following, we will discuss each component of this hierarchical cooperative control framework in details.

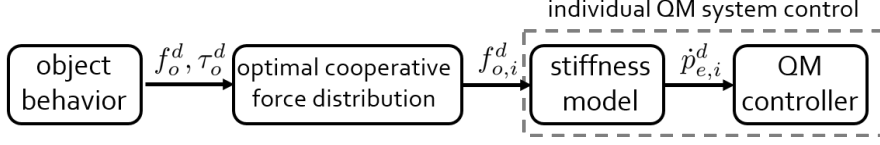


FIGURE 3.1: Hierarchical cooperative control framework of multiple QM systems

3.3.1 Object Behavior Design

As stated above, depending on the task objective, the cooperatively-grasped object should exhibit a certain desired behavior such as trajectory tracking, compliant interaction, etc. The goal of the object behavior design block of our proposed control framework is to determine the object wrench to achieve the designated target behavior of the object. For this, we assume that the grasped object is a 6-DOF rigid-body, whose dynamics is given by:

$$m_o \ddot{p}_o + m_o g = f_o + f_{ext}$$

$$I \dot{w}_o + w_o \times I_o w_o = \tau_o + \tau_{ext}$$

where $m_o \in \mathbb{R}$, $I_o \in \mathbb{R}^{3 \times 3}$ are the mass and moment of inertia of the object, $p_o, w_o \in \mathbb{R}^3$ are its position and angular velocity, $f_o, \tau_o \in \mathbb{R}^3$ are the resultant force and torque exerted by the N QM systems' end-effectors, and $f_{ext}, \tau_{ext} \in \mathbb{R}^3$ are its interaction force/torque with external environments.

We can then design f_o and τ_o to achieve some desired behavior of the grasped object. For instance, impedance interaction at the object center-of-mass with

scaled apparent inertia with rotational spring behavior can be achieved by

$$\begin{aligned} f_o &= \alpha f_{ext} + m_o g + m_o \ddot{p}_o^d + D(\dot{p}_o^d - \dot{p}_o) + K(p_o^d - p_o) \\ \tau_o &= -\gamma w_o - \sigma[R_d^T R_o - R_o^T R_d]^\vee \end{aligned}$$

where α is to scaling the apparant mass of the object at its center-of-mass, f_{ext} is external force which may be obtained by force sensor or disturbance observer [41], $p_o^d \in \mathbb{R}^3$ is the desired object trajectory, $D, K \in \mathbb{R}^{3 \times 3}$ are the symmetric and positive-definite damping and spring gains, R_d is the set-rotation for the rotational spring, γ, σ are the damping and the rotation stabilization gain for rotation dynamics and $[\cdot]^\vee$ denotes the operation $so(3) \rightarrow \mathbb{R}^3$ [53]. This impedance type behavior can be used for physical interaction tasks with external environment, humans or another objects by changing its parameter to behave lighter/softer (i.e., low impedance) or heavier/stiffer (e.g., high impedance) than the original system. Note that, for such physical interaction tasks, we typically have small $(\ddot{p}_o, \dot{p}_o, w_o)$. Also note that with $\alpha = 0$ or $(f_{ext}, \tau_{ext}) \approx 0$, which typically true for the transport operation, the object transport can be achieved.

3.3.2 Optimal Cooperative Force Distribution

To realize the desired object wrench, $F_o := [f_o; \tau_o] \in \mathbb{R}^6$, as designed in Sec. 3.3.1, we then need to determine the contact force $f_{o,i}^d \in \mathbb{R}^3$ exerted by each QM system's end-effector on the grasped object. For this, we utilize the following Jacobian relation between the object wrench F_o and the end-effector

force $f_{o,i}$ s.t.,

$$F_o = J_o \bar{f}_o \quad (3.9)$$

where $J_o \in \mathbb{R}^{6 \times 3N}$ is the object Jacobian and $\bar{f}_o = [f_{o,1}; \dots, f_{o,N}] \in \mathbb{R}^{3N}$ is the collection of the end-effector contact forces of all the QM systems, with $f_{o,i} \in \mathbb{R}^3$ being the end-effector contact force of the i -th QM system, which contains both the normal and shear/friction forces as shown in Fig. 3.2. Here, we assumed that the contact between each QM system and the object is the point contact with friction and without moment transmission. The case of more general contact scenarios will be studied in a future publication. Then, the end-effector force $f_{o,i}$ can be decomposed with respect to the object surface s.t.,

$$f_{o,i} = f_{n,i} \cdot u_{n,i} + f_{s1,i} \cdot u_{s1,i} + f_{s2,i} \cdot u_{s2,i}$$

where $u_{n,i}, u_{s1,i}, u_{s2,i} \in \mathbb{R}^3$ are the normal and tangential directional unit vectors, which are orthogonal with each other; and $f_{n,i}, f_{s1,i}, f_{s2,i} \in \mathbb{R}$ are the magnitude along each direction. See Fig. 3.2.

Here, in (3.9), $J_o \in \mathbb{R}^{6 \times 3N}$ is typically a fat matrix ($3N > 6$). Therefore, the solution of \bar{f}_o of (3.9) is not unique with different “internal/null-space forces”. Moreover, the contact force of each QM system should satisfy the friction cone constraint [54] to maintain the contact while avoiding slippage. We now formulate this problem of finding \bar{f}_o as the following constrained optimization

problem:

$$\begin{aligned}
& \min_{f_s, f_n} \quad \alpha_1 f_s^T f_s + \alpha_2 f_n^T f_n & (3.10) \\
& \text{subject to} \quad F_o = J_o \mathcal{N} f_n + J_o \mathcal{T} f_s \\
& \quad \quad \quad \sqrt{f_{s1,i}^2 + f_{s2,i}^2} \leq \mu f_{n,i}, \quad i = 1, 2, \dots, N
\end{aligned}$$

where $\alpha_1, \alpha_2 > 0$ are the weights, $f_n := [f_{n,1}; \dots; f_{n,N}] \in \mathbb{R}^N$ and $f_s := [f_{s1,1}; f_{s2,1}; \dots; f_{s1,N}; f_{s2,N}] \in \mathbb{R}^{2N}$ are respectively the collections of the normal and shear friction force components of $f_{o,i}$ w.r.t. the object contact surface, $\mu > 0$ is the static friction coefficient, and $\mathcal{N} \in \mathbb{R}^{3N \times N}$ and $\mathcal{T} \in \mathbb{R}^{3N \times 2N}$ respectively identify the tangential and normal directions with their expressions given by

$$\mathcal{N} = \text{diag}(u_{n,1}, \dots, u_{n,N}), \quad \mathcal{T} = \text{diag}(u_{s,1}, \dots, u_{s,N}).$$

where $u_{s,i} = [u_{s1,i}, u_{s2,i}] \in \mathbb{R}^{2 \times 2}$ is the collection of the i -th QM system's tangential directional unit vectors.

For this constrained optimization problem, we choose $\alpha_1 > \alpha_2 > 0$ to ensure the shear/friction force $f_{s,i}$ to be low to have a better margin against the contact slippage, while also simultaneously preventing excessively large normal contact force. Note also that: 1) the equality constraint of (3.10) is merely a different representation of the object Jacobian relation (3.9), whereas the inequality constraint in (3.10) is to enforce the friction-cone condition to ensure no-slip contact. This optimization problem is convex and has the structure of force optimization problem (FOP), thus this can be formulated as a semidefinite programming problem (SDP) or a second-order cone problem (SOCP)

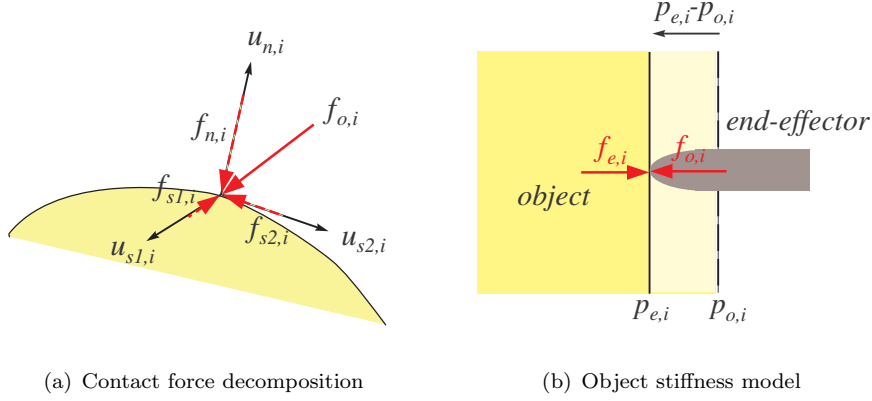


FIGURE 3.2: Contact force decomposition and object stiffness model.

[54, 55]. This FOP can be solved by standard numerical optimization method, however, to solve more faster depending on tasks, problem should be customized (e.g., dual problem [55]) rather than general SDP or SOCP. But, in this chapter, for the case of three QM systems and not agile motion in 3.3.4, standard method is sufficient to provide real-time solution.

Each individual QM system should then be able to exert this optimally-distributed contact force $f_{o,i}$. For this, we may attempt to devise a direct end-effector force control, which, yet, may not be straightforward to design here due to the presence of the quadrotor under-actuation along with the actuation redundancy of the QM system. Moreover, in practice, the robotic manipulator, which can be attached on the quadrotor platform, would likely have non-negligible joint friction. Even further, given the hardware and control precision limitations of currently available quadrotor platforms, the achievable speed of the cooperative manipulation of the grasped object would be rather slow. Due to this reason, in this chapter, we adopt the admittance-type force

control and, for that, in Sec. 3.3.3, we will extend the position control law (3.6) to the case of uncertain object deformation model, while also explicitly taking into account the different dynamics characteristics of the quadrotor platform and the robotic manipulator.

3.3.3 Force Control of QM System with Object Stiffness Model

To derive the admittance-type end-effector force control for each QM system, similar to [56], here, we assume that the deformation of the object is small so that it can be approximated by the linear stiffness model, i.e.,

$$f_{e,i} = -K_o(p_{e,i} - p_{o,i}) \quad (3.11)$$

where $f_{e,i} \in \mathbb{R}^3$ is the contact force exerted by the object to the QM system's end-effector with $f_{e,i} = -f_{o,i}$, $p_{e,i}, p_{o,i} \in \mathbb{R}^3$ are respectively the positions of the end-effector and the (undeformed) contact point of that end-effector on the grasped object, and $K_o \in \mathbb{R}^{3 \times 3}$ is the *uncertain* stiffness matrix. Here, we also assume that the deformation associated with each QM system's end-effector is independent from each other.

To achieve the admittance-type contact force control, we now design the evolution of the end-effector target position $p_{e,i}^d \in \mathbb{R}^3$ s.t.,

$$\dot{p}_{e,i}^d := k_1(f_{e,i} - f_{e,i}^d) + k_2 \int (f_{e,i} - f_{e,i}^d) dt + \dot{p}_{o,i} \quad (3.12)$$

where $k_1, k_2 > 0$ are the PI control gains, $f_{e,i}$ is the contact force feedback, for which we assume force sensor or disturbance estimator for each QM system[41],

and $f_{e,i}^d \in \mathbb{R}^3$ is the desired contact force assigned by the optimal cooperative force distribution algorithm (3.10). Here, note that we can compute $p_{o,i}$ with the position and orientation sensing of the object center with the information on its undeformed shape.

Theorem 2. Consider the N multiple cooperative QM systems with each of their dynamics given by (3.3)-(3.4) and their desired end-effector force given by $f_{e,i}^d$ (i.e., from (3.10)). Suppose that the object acceleration \ddot{p}_o and the rate of change of each QM system's desired contact force $\dot{f}_{e,i}^d$ are bounded. Then, if we set the control τ_L, τ_E s.t.,

$$\begin{aligned} \tau_L + m_L B M_E^{-1} [\tau_E - C_E \dot{r}] &= -f_L - m_L B M_E^{-1} f_E \\ &+ g_L + m_L [\hat{\ddot{p}}_e^d - \beta \dot{e}_p - \gamma(e_f + \epsilon \int e_f dt) - \frac{dB}{dt} \dot{r}] \end{aligned} \quad (3.13)$$

where $e_f := f_{e,i} - f_{e,i}^d$, $\hat{\ddot{p}}_{e,i}^d = \ddot{p}_{e,i}^d + \eta$ with bounded η , $\gamma, \beta, \epsilon > 0$ and $\epsilon < k_1 \cdot \lambda_{\min}[K_o]$, (e_f, e_{fI}, \dot{e}_p) is ultimately bounded, where $e_{fI} := \int e_f dt + \dot{f}_d$ with $\dot{f}_d := (1/k_2) K_o^{-1} \dot{f}_{e,i}^d$ and $e_p := p_{e,i} - p_{e,i}^d$.

Proof: Using the object stiffness model (3.11) and the evolution equation (3.12), we have

$$\begin{aligned} \dot{e}_f &= -K_o(\dot{p}_{e,i}^d - \dot{p}_{o,i}) - K_o \dot{e}_p - \dot{f}_{e,i}^d \\ &= -k_1 K_o e_f - k_2 K_o \int e_f dt - K_o \dot{e}_p - \dot{f}_{e,i}^d \end{aligned} \quad (3.14)$$

From this, let us define the following Lyapunov function candidate:

$$V_1 := \frac{1}{2} e_f^T e_f + \frac{1}{2} e_{fI}^T k_2 K_o e_{fI} + \epsilon e_f^T e_{fI}$$

where ϵ is a small constant to make V_1 to be positive-definite and to be determined below. Then, using (3.12)-(3.14), the time derivative of V_1 is given by

$$\begin{aligned} \frac{dV_1}{dt} = & - \begin{pmatrix} e_f \\ e_{fI} \end{pmatrix}^T \underbrace{\begin{bmatrix} k_1 K_o - \epsilon I_3 & \frac{1}{2} \epsilon k_1 K_o \\ \frac{1}{2} \epsilon k_1 K_o & \epsilon k_2 K_o \end{bmatrix}}_{:=Q} \begin{pmatrix} e_f \\ e_{fI} \end{pmatrix} \\ & + \begin{bmatrix} \epsilon \ddot{f}_d & k_2 K_o \ddot{f}_d \end{bmatrix} \begin{pmatrix} e_f \\ e_{fI} \end{pmatrix} - \dot{e}_p^T K_o (e_f + \epsilon e_{fI}) \end{aligned} \quad (3.15)$$

where $Q > 0$ for small enough $\epsilon < k_1 \cdot \lambda_{\min}[K_o]$. To proceed more, again, we define Lyapunov candidate function V_2 :

$$V_2 := V_1 + \frac{1}{2\gamma} \dot{e}_p K_o \dot{e}_p$$

Time derivative is derived using (3.3), (3.4),

$$\begin{aligned} \frac{dV_2}{dt} = & - \begin{pmatrix} e_f \\ e_{fI} \end{pmatrix}^T Q \begin{pmatrix} e_f \\ e_{fI} \end{pmatrix} + \begin{bmatrix} \epsilon \ddot{f}_d & k_2 K_o \ddot{f}_d \end{bmatrix} \begin{pmatrix} e_f \\ e_{fI} \end{pmatrix} \\ & - \frac{1}{\gamma} \dot{e}_p^T K_o [\gamma(e_f + \epsilon e_{fI}) - \ddot{e}_p] \end{aligned} \quad (3.16)$$

where $\ddot{e}_p = \ddot{p}_{e,i}(\tau_L, \tau_E) - \ddot{p}_{e,i}^d(\dot{f}_{e,i}, \dot{f}_{e,i}^d, f_{e,i}, f_{e,i}^d, \ddot{p}_{o,i})$. The first term is extended by dynamics (3.3)-(3.4) and (3.5) where

$$\ddot{p}_{e,i} = \frac{1}{m_L} [\tau_L + f_L - g_L] + B M_E^{-1} [\tau_E + f_E - C_E] + \dot{B} \dot{r}. \quad (3.17)$$

In the second term of \ddot{e}_p , $\ddot{p}_{e,i}^d$ is given by parameters in the parenthesis. $f_{e,i}$

is known from force sensor/estimator, $\dot{f}_{e,i}^d$, $\ddot{p}_{o,i}$ assumed to be bounded by assumption and $f_{e,i}^d$ is known from optimal cooperative force distribution. Then, all the parameters in the parenthesis are known or bounded, thus, we can write $\ddot{p}_{e,i}^d = \hat{\ddot{p}}_{e,i}^d - \eta$ where $\hat{\ddot{p}}_{e,i}^d$ is estimated from known parameter or numerically calculated and η is bounded remained term. From this, control generation equation (3.13) can be equivalently represented as following equation using (3.3)-(3.4) and (3.17)

$$\ddot{p}_{e,i} - \hat{\ddot{p}}_{e,i}^d = \gamma(e_f + \epsilon e_{fI} - \frac{1}{k_2} K_o^{-1} \dot{f}_{e,i}^d) - \beta \dot{e}_p. \quad (3.18)$$

Using this relation, time derivative \dot{V}_2 becomes

$$\begin{aligned} \frac{dV_2}{dt} = & - \begin{pmatrix} e_f \\ e_{fI} \end{pmatrix}^T Q \begin{pmatrix} e_f \\ e_{fI} \end{pmatrix} - \frac{\beta}{\gamma} \dot{e}_p^T K_o \dot{e}_p \\ & + \left[\epsilon \ddot{f}_d \ K_o k_2 \ddot{f}_d \right] \begin{pmatrix} e_f \\ e_{fI} \end{pmatrix} + \frac{1}{\gamma} \dot{e}_p^T K_o \bar{\eta} \end{aligned} \quad (3.19)$$

where $\bar{\eta} = \eta - \frac{1}{k_2} K_o^{-1} \dot{f}_{e,i}^d$ which is bounded. Then, all the terms, which are not negative definite, are bounded, thus are (e_f, e_{fI}, \dot{e}_p) are ultimately bounded by control (3.13). ■

Note from Th. 2 that we can guarantee the desired force tracking by enforcing (3.13), even if the object stiffness K_o is unknown. Note also that, in the control input (3.13) with the target position dynamics (3.12), there is no usage of the object stiffness K_o . This proposed admittance-type force control (3.13) shares the similar development idea with the position tracking control of [40]

(i.e., (3.7)-(3.8)). Yet it has been extended from (3.7)-(3.8) by incorporating the (unknown) object stiffness model K_o , the target position evolution equation, and the cross-coupling term (i.e., ϵ) to guarantee ultimately boundedness even in the presence of (inaccessible) $\dot{f}_{e,i}^d, \ddot{f}_{e,i}^d$.

We further modify this admittance-type force control here to explicitly into account the different dynamics characteristics of the (slower/coarse) quadrotor platform and the (faster/fine) robotic manipulator. More precisely, we assign the desired control generation equation (3.13) into the (under-actuated) quadrotor thrust control $\tau_L = -\lambda R e_3$ and the (fully-actuated) internal rotation dynamics control τ_E s.t.,

$$\tau_L^d = g_L + m_L[\text{LPF}_{w_c(\sigma)}[\hat{p}_e^d] - \beta \dot{e}_p - \zeta(r)] - f_L \quad (3.20)$$

$$\begin{aligned} m_L B M_E^{-1} [\tau_E - C_E \dot{r}] = & -f_L - m_L B M_E^{-1} f_E - \tau_L \\ & + g_L + m_L [\hat{p}_e^d - \beta \dot{e}_p - \gamma(e_f + \epsilon \int e_f dt) - \frac{dB}{dt} \dot{r}] \end{aligned} \quad (3.21)$$

where LPF is a low pass filter operator and $w_c(\sigma)$ is the cut-off frequency of this LPF, which we define to be a function of the manipulability σ of the robot manipulator [57]. Also, similar to (3.7), here, we design the desired thrust input τ_L^d via (3.20), which will be achieved by using the internal rotation control τ_E in the null-space of $B M_E^{-1}$, whereas the other components of τ_E can still guarantee the control generation equation (3.13) even if $\tau_L \neq \tau_L^d$ via (3.20)

Here, additional terms are introduced by external force f_L, f_E from interaction with the grasped object. We design the control input τ_L and τ_E (3.20)-(3.21) to cancel out these external forces f_L, f_E . Physically, f_L affect

the dynamics of the total QM system's center-of-mass position, so that thrust τ_L should resist f_L . On the other hand, f_E perturbs the quadrotor rotation and the manipulator configuration, thus, τ_E is used to cancel out f_E to maintain its posture.

Our proposed force control should also allow each QM systems to maintain its non-singular posture. For instance, when the QM system manipulates, the quadrotor platform should to keep a certain distance from the object for safety and the manipulator needs to recede from singular configuration which can cause instability. For this, the subtask $\zeta(r)$ utilized.

In (3.20), the low pass filter (LPF) is only applied to \ddot{p}_e^d , because gravity should be maintained by thrust τ_L and other terms are cancelled out or converge to small bounded value by Th. 2. Then, the LPF in the control equation (3.20) assigns low frequency slow motion to quadrotor platform via τ_L , then, the remained trajectory, which is high frequency component after substituting low frequency component, would be assigned to manipulator via τ_E . But, some infeasible desired motion can be generated without kinematic consideration. Since the manipulability is an index for measuring singularity, we propose to adapt the cut-off frequency depending on the manipulability using following relation

$$w_c = w_{c,min} \left(\frac{\sigma_{max}}{\sigma} \right)$$

where $w_{c,min}$ is the minimum cut-off frequency, σ is manipulability, σ_{max} is maximum value of the manipulability. From this equation, more specifically, if this manipulability σ is sufficient (i.e., $\sigma \approx \sigma_{max}$), the cut-off frequency of

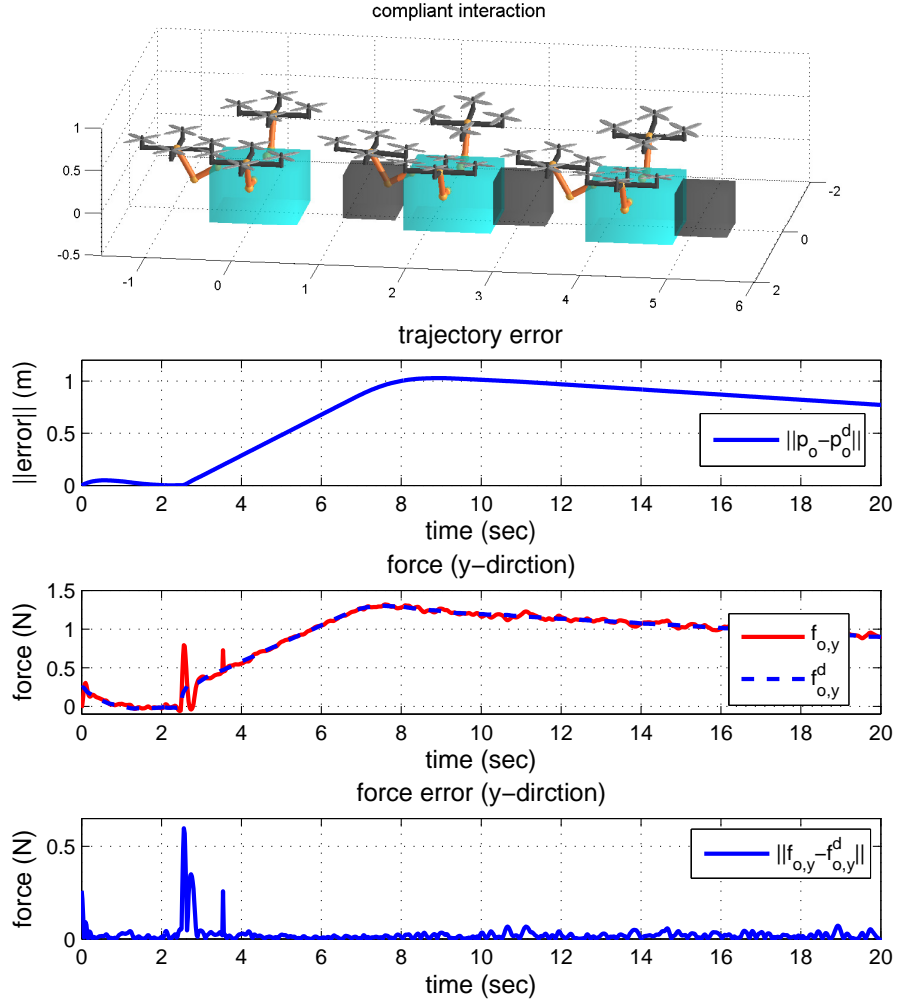


FIGURE 3.3: Snapshots of the object pushing task using the multiple QM system under admittance-type force control with force profile.

the LPF is set to be lower and almost all the motion would be assigned to the robotic manipulator via τ_E . On the other hand, near the singularity $\sigma \approx 0$, the cut-off frequency will be set to be higher and almost all the motion would be assigned to the quadrotor platform via τ_L .

3.3.4 Simulation

We perform two simulations using our proposed cooperative control framework. Here, the inertial parameter of quadrotor are $m_0 = 2kg$ and $(I_{xx}, I_{yy}, I_{zz}) = (1.24, 1.24, 1.24)kg \cdot m^2$ which are similar with AscTec[®] Pelican. 2-dof manipulator's inertial parameters are $(m_1, m_2) = (0.5, 0.4)kg$ and moment of inertia is assumed as cylinder and its length is $(l_1, l_2) = (0.4, 0.3)m$. Manipulator parameters are larger than real system to see dynamics effect. Moment of inertia is usually inaccurate, even though we can measure exact mass and length of the manipulator, thus, we add 20% error in the moment of inertia. Mass and stiffness of the object in the simulation, Fig. 3.5-3.4, are $m_o = 0.4kg$, $k_o = 200N/m$ which have $\sim 2cm$ of deformation to resist its weight. And also, here, we assume a force sensor to measure the exerting force which usually have white noise. To simulate this noise, we add a noise $w \sim \mathcal{N}(0, 0.04)$ with $3\sigma = 0.6$. Low pass filter with time constant $T = 0.5$ is also applied to reduce sensor noise, therefore, the measured force have delay due to filter.

The first simulation in Fig. 3.5 shows compliant interaction using the grasped object. For this, compliant behavior of the object is designed for object behavior design layer based on 3.3.1. Here, we control the grasped object position to y -axis. Then, to achieve this desired behavior, the optimization provides the

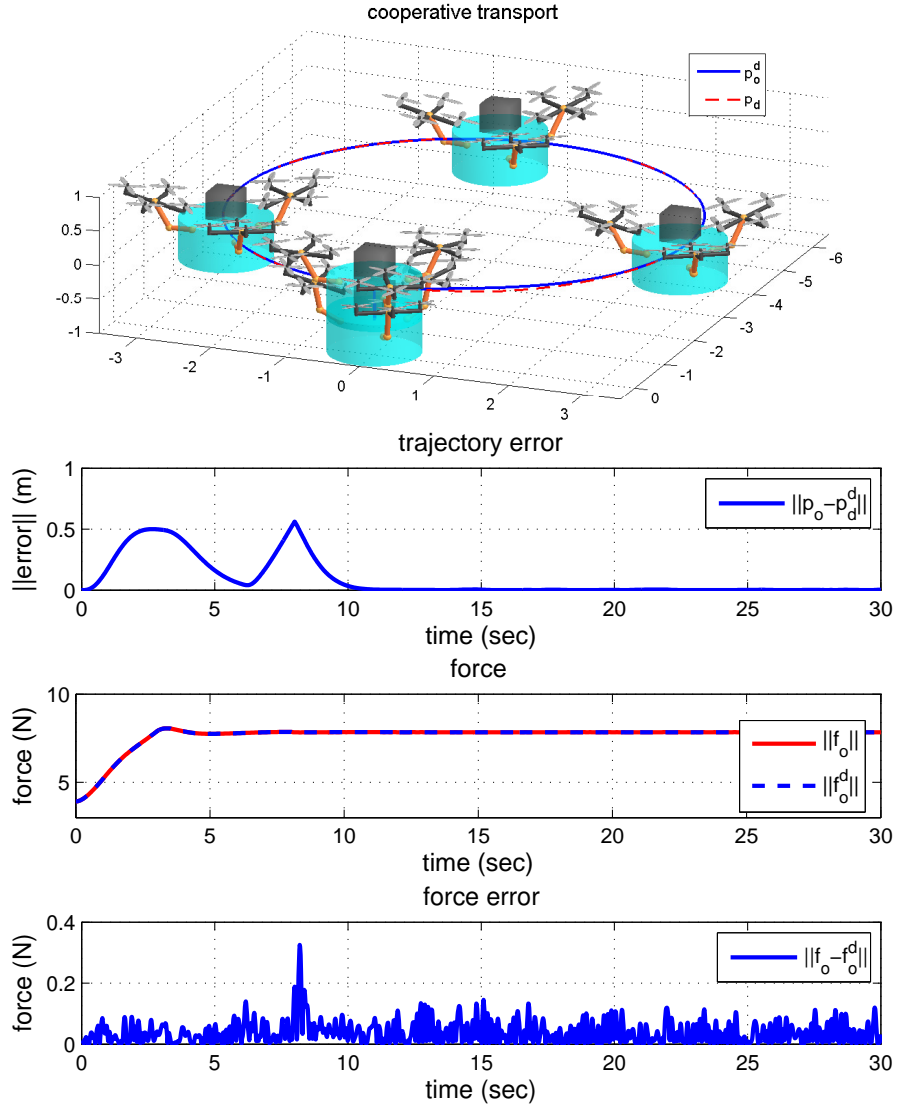


FIGURE 3.4: Snapshots of the object transport using cooperative QM systmes control of compliant behavior with unknown mass and parameter adaptation.

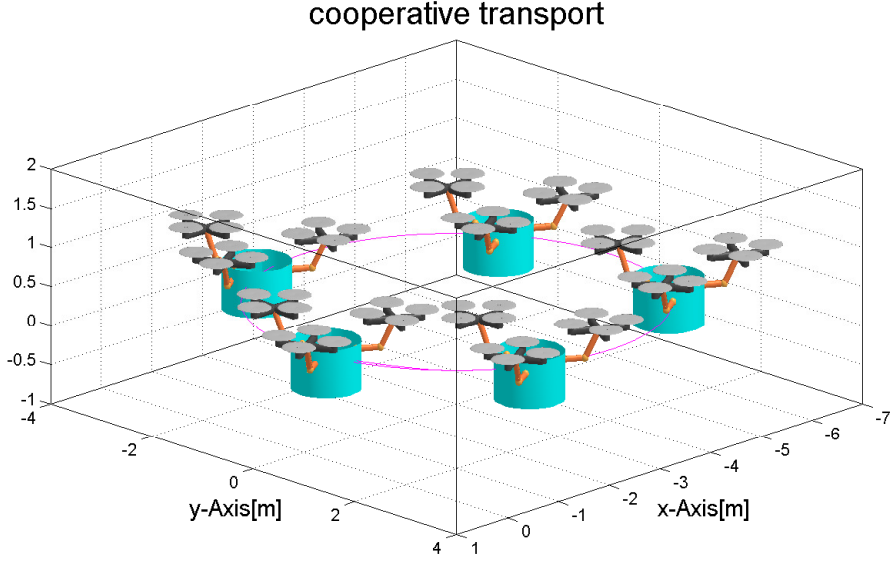


FIGURE 3.5: Snapshots of the quadrotor-manipulator system under admittance-type force control with force profile.

desired force distribution $f_{e,i}^d$. Using control (3.20)-(3.21), each QM system is controlled to achieve the desired forces $f_{e,i}^d$. Then, the grasped object pushes the object in a stationary manner. At 2.5 second, the grasped object contacts with the another, black, object. Therefore, some position error is induced by repulsive force and the compliant behavior still can follow the desired force f_o^d , though bounded force error exists. See the bottom of Fig. 3.5.

In the second simulation, Fig. 3.4, we add an unknown mass on the stationary grasped object and perform circular trajectory tracking. At first, due to the unknown mass, grasped object goes to downward and position error is increased. However, the QM systems still can maintain the object grasping, even though the unknown mass disturbs position. Using the parameter adaptation of the unknown mass about the object dynamics [58], position error converges to zero and follows the desired trajectory. Note that, the second peak at 8 sec

is caused by initial condition error (velocity and acceleration) of trajectory tracking.Chap3:

3.4 Conclusion

In this chapter, we propose the cooperative control framework for multiple QM systems which consist of following hierarchical structure: 1) object behavior design; 2) optimal cooperative force distribution; and 3) individual QM system control. The proposed control framework can be adapted to variable tasks which need different behavior by changing a specific control block rather than redesign the whole controller. And also, different types of individual QM system controllers are also applicable to this control framework without variation of the hierarchical structure. We extend previous result about the QM system position controller (3.6) from decoupled dynamics structure to admittance-like force control (3.13). Moreover, we propose how to control the individual QM system, using the decoupled dynamics (3.3)-(3.4), depending on different dynamics characteristics of the (under-actuated/slower/coarse) quadrotor platform and the (fully-actuated/faster/fine) manipulator. Simulation results of cooperative object transport and compliant interaction are presented.

Chapter 4

Flexible Load Vibration Suppression using Multi-rotor Drone

4.1 Introduction

Free flying control problem of small-size multi-rotor aerial robots is now well established with many strong theoretical results (e.g., [7–10]) and commercial systems (e.g., [11, 12]). So successful has been this multi-rotor aerial robot particularly for the aerial photography and visual inspection applications by extending humans’ eyes to the sky. The next step, naturally along this line of reasoning, would then be to extend humans’ hands to the sky, namely, the problem of aerial operation and manipulation (e.g., [13–16]), which can be useful for such applications as infrastructure maintenance [17], remote construction [18], object transport and assembly [19–21], etc.

Now, let us consider the problem of large-size structure construction. For this, the (virtually) unlimited workspace of the aerial robots would be useful. However, at the same time, such construction usually requires manipulation of large-size objects (e.g., steel bar, wood beams, etc.) typically too heavy

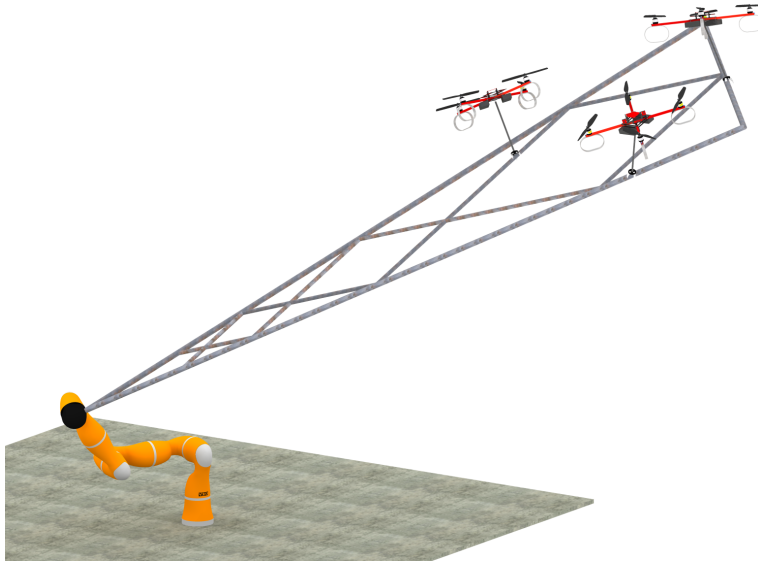


FIGURE 4.1: MAGMaS composed of one ground manipulator and three aerial robots with a co-manipulated large object.

to carry by many usual aerial robots alone due to the inherent rotor-battery limitation. On the other hand, ground (mobile or fixed) manipulators are typically of high payload, yet, their workspace (or working height) limited. To address this challenge, the MAGMaS (Multiple Aerial-Ground Manipulator System) was proposed in [36] as a heterogeneous system composed of multiple ground (mobile) manipulators (with high payload, yet, limited workspace) and aerial robots (with large workspace, yet, limited payload) to collaboratively manipulate a large-size heavy object by utilizing their capabilities in a complementary manner. The MAGMaS, of course, can be useful for other applications as well, e.g., warehouse automation, manipulation of large/heavy repair/inspection tool, etc. See Fig. 4.1.

The focus of [36], however, was, on top of proposing this new class of MAGMaS and its implementation, to propose the control framework for the

large/slender *rigid* object manipulation by employing the complementary capabilities and redundancy of the ground-aerial robots. In this chapter, we extend this result of [36] to the case of load manipulation with *flexibility*, which is crucial for long/slender object manipulation, yet, not addressed in [36]. For this, we first provide a rigorous modeling of the MAGMaS with the (slender) load flexibility incorporated into that using Euler-Bernoulli beam theory. We then propose a novel collaborative control framework for the flexible load-tip pose tracking, where the ground manipulator provides slower nominal pose tracking with overall load weight holding, whereas the aerial robot¹ faster vibration suppression with some load weight sharing. We also elucidate the issue of controllability stemming from that the aerial robot provides less number of actuation than that of the modes of the load flexibility; and delineate some peculiar conditions for this vibration suppression controllability with their physical meaning manifested. Simulations are also performed to demonstrate the effectiveness of the proposed theory.

4.2 System Description

In this section, we recall and detail the composition of the Multiple Aerial Ground Manipulators System (MAGMaS) introduced in [36]. We then provide the dynamical modeling developed in Sec. 4.3. A MAGMaS consists of a n -degrees of freedom (DoFs) ground manipulator, some load/object to manipulate and one or several aerial robot (e.g., quadrotor) connected to the load,

¹It is also worthwhile to mention that this aerial robot, by providing collocated load-tip actuation, can allow us to circumvent the well-known issue of nonminimum-phase dynamics for load-tip pose tracking control if only ground robot is employed [42, 43].

see. Fig 4.1. This system is proposed to outperform the other approaches on aerial manipulation by taking advantage of its heterogeneity: 1) higher payload and unlimited operation time of the robotic manipulator; 2) dealing with large objects or workspace with a group of aerial robots [36].

We assume a manipulated object as a long bar with skewed rectangular shape cross-section so that the vibration along only one direction is substantial, while that along the other negligible. We also confine ourselves to the case of planar manipulation in this chapter. The ground manipulator considered is then a planar n -dof manipulator. We also limit our study to a MAGMaS composed of a single aerial robot, which grasps (or is attached to) the bar-end. Even with this reduction, as can be seen below, the obtained key technical results and frameworks would be extendable to more general cases as well. The aerial robot is connected to the bar by the mean of small arm mounted on a passive rotational joint, whose center of rotation coincides with aerial robot center-of-mass (CoM). This is a requirement to limit the torque exerted by the aerial robot on the load as the actuation limits on the torque of such platform are typically quite low. This also implies that the load and the aerial robot exchange only force, not moment. See Fig. 4.2.

From the sketch in Fig. 4.2, we can detail the notations used throughout the chapter. On the ground, n -DoF robot arm is mounted whose joint configuration is defined as $\theta \in \mathbb{R}^n$. The position of each joint and the center-of-mass of each links w.r.t. the inertial frame \mathcal{W} are defined as $p_i^{\mathcal{W}} \in \mathbb{R}^2$ and $p_{c,i}^{\mathcal{W}} \in \mathbb{R}^2$ respectively. Similarly, the end-effector position of the robot arm is defined as $p_e^{\mathcal{W}} \in \mathbb{R}^2$. For brevity, we will omit the \mathcal{W} when the position is represented in the inertial frame. Define the position and the orientation of the aerial robot

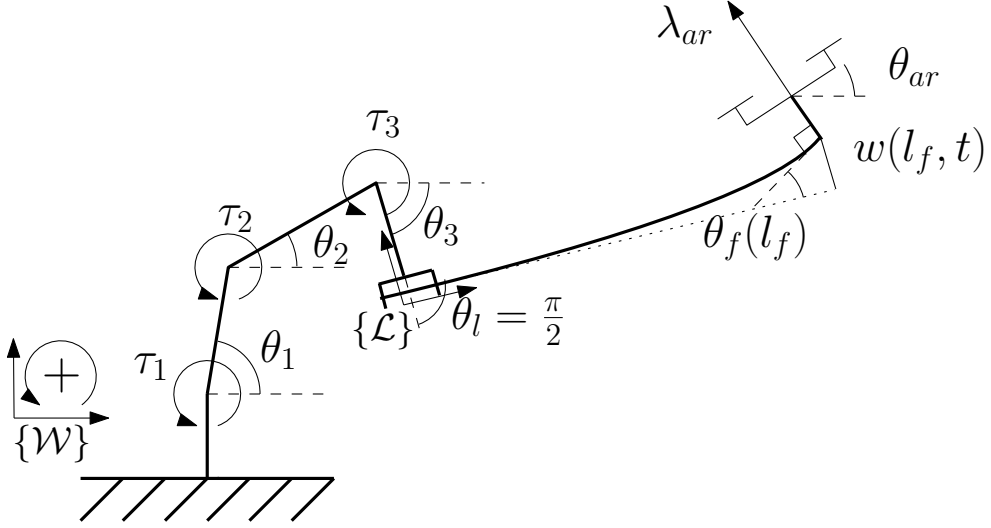


FIGURE 4.2: Sketch of the configuration of the MAGMaS.

attached on the load-tip w.r.t. \mathcal{W} as $p_{ar} \in \mathbb{R}^2$ and $\bar{\theta}_{ar} \in \mathbb{R}$. For any angle, e.g. θ , the notation $\bar{\theta}$ represents the absolute angle, e.g., $\bar{\theta}_i = \sum_{j=1}^i \theta_j$, while θ representing relative angle throughout this chapter.

The flexible load is rigidly attached to end-effector of the robot arm. The relative angle between the end-effector and the flexible load is given as θ_l . As shown in Fig. 4.3, the position and orientation of the flexible load along the x -axis w.r.t. the flexible load frame \mathcal{L} at time t can be written as

$$p_f^{\mathcal{L}}(x, t) = \begin{bmatrix} x \\ w(x, t) \end{bmatrix}, \quad \theta_f(x, t) = \frac{\partial w(x, t)}{\partial x}$$

where $w(x, t)$ is the deflection along y -direction at x in the load frame \mathcal{L} . We omit x at the load-tip position $x = l_f$ for brevity, i.e., $p_f^{\mathcal{L}}(l_f) = p_f^{\mathcal{L}}$ and $\theta_f(l_f) = \theta_f$. Recall that the aerial robot is connected to the flexible load via a passive rotational joint, which allows free relative rotation of the aerial robot

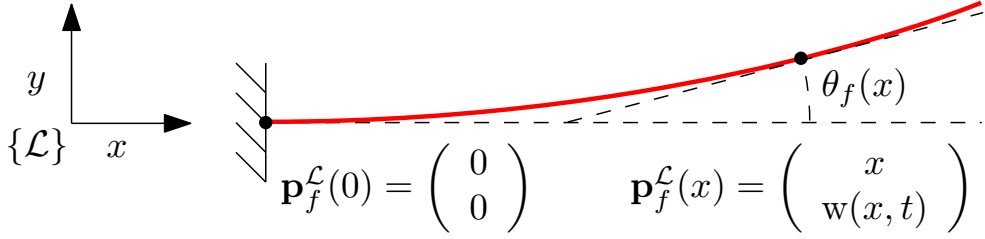


FIGURE 4.3: Euler-Bernoulli beam deflection model.

as stated above, $\bar{\theta}_{ar}$ can be independently controlled by the aerial robot. The length of the arm between the load-tip and the aerial robot CoM is d_{conn} which is assumed zero in the rest of the chapter, thus neglecting torque generated on the load by the aerial robot thrust via the rigid connecting arm.

4.3 System Modeling

The dynamic model of the MAGMaS based on the Euler-Bernoulli beam theory and Euler-Lagrange equation is derived in this section. We first briefly introduce the Euler-Bernoulli equation which is not a main contribution of this chapter, and then derive the dynamic equation of the whole MAGMaS.

4.3.1 Flexibility Modeling of the Load

Here, we suppose to include only transverse vibration, i.e., torsional effects are neglected, with restriction of motion of the MAGMaS to planar space. This assumption can be enforced by a proper structural design of the load (e.g., long slender beam) [59]. To model vibration of the flexible load, here, we adopt Euler-Bernoulli beams theory [59], whose governing equation is given

as follows

$$\rho A(x) \frac{\partial^2 w(x, t)}{\partial t^2} + \frac{\partial^2}{\partial t^2} EI(x) \frac{\partial^2 w(x, t)}{\partial t^2} = 0 \quad (4.1)$$

where E, I, ρ, A are Young's modulus, the second moment of area, the density and the intersection area of the flexible load respectively. These material properties are invariant for the homogeneous load with uniform cross section, thus, in this chapter, we assume the constant parameters along the flexible load to simplify the beam model and to meet the practical objects (e.g., long rectangular wooden rod). Using the separation of variables, a solution of given partial differential equation (4.1) can be written s.t.,

$$w(x, t) = \sum_{i=1}^m \phi_i(x) \delta_i(t) =: \Phi(x) \delta(t) \quad (4.2)$$

where $w(x, t) \in \Re$ is the load deflection along the y -direction at x and time t w.r.t the load frame \mathcal{L} , m is the number of assumed vibration modes, $\phi_i(x)$ is the time invariant mode shape function, $\delta_i(t)$ describes the time varying part of the deflection associated with given mode shape $\phi_i(x)$, $\Phi := [\phi_1, \dots, \phi_m] \in \Re^m$ is the combined row vector of mode shapes and $\delta := [\delta_1; \dots; \delta_m] \in \Re^m$ is the combined column vector of δ_i . In practice, high frequency modes are suppressed quickly due to their damping. Therefore, we only consider a finite dimension m of the vibration modes.

The explicit solution form of $\phi_i(x)$ can be written as following

$$\phi_i(x) = C_{1,i} \cosh \beta_i x + C_{2,i} \cos \beta_i x + C_{3,i} \sinh \beta_i x + C_{4,i} \sin \beta_i x \quad (4.3)$$

where C_i are the coefficients, $\beta_i^4 = w_{n,i}^2 \rho A / EI$, and $w_{n,i}$ is the natural frequency of i -th vibration mode. All these parameters are determined by the boundary condition of Euler-Bernoulli equation (4.1). To determine these coefficients, we adopt two boundary conditions: 1) the clamped boundary conditions at $x = 0$, (i.e., at the end-effector position); 2) the mass boundary conditions for moment and shear force at the load-tip l_f induced by aerial robot. These are expressed as following four conditions [60]:

$$w(x = 0, t) = 0, \quad \theta_b(x = 0, t) \approx \frac{dw}{dx} = 0 \quad (4.4)$$

$$M(x = l_f) = 0 \quad (4.5)$$

$$V(x = l_f) = -m_{ar}\ddot{w}_b(l_f, t) + m_{ar}ge_2 \quad (4.6)$$

where θ_b is deflection angle, $M(l_f) = EI \frac{\partial w^2}{\partial x^2}$ is the moment, $V(l_f) = -EI \frac{\partial w^3}{\partial x^3}$ is the shear force at the load-tip. Using these four equations derived from the boundary conditions, five coefficients $C_{1,i}, C_{2,i}, C_{3,i}, C_{4,i}, \beta_i$ can only be determined up to scale [60]. The scale of the coefficients can be determined by normalization based on the following relation

$$\rho A \int_0^{l_f} \phi_i(x)^2 dx + m_{ar} \phi_i(l_b)^2 = \frac{EI}{w_{n,i}^2} \int_0^{l_f} \phi_i''(x)^2 dx \quad (4.7)$$

This relation is derived by (4.1), (4.4)-(4.6). By assuming the left hand side of (4.7) to be unity, the mode shape ϕ_i is normalized, then we can determine scale of coefficients $C_{i,j}$.

Here, the mode shape is the eigenfunction describing the deflection based on Euler-Bernoulli equation (4.1). Therefore, orthogonality is enforced to each

mode shapes for $i \neq j$ [60] s.t.:

$$\int_0^{l_f} \phi_i''(x) \phi_j''(x) dx = 0 \quad (4.8)$$

$$\int_0^{l_f} \phi_i(x) \phi_j(x) dx + m_{ar} \phi_i(l_f) \phi_j(l_f) = 0 \quad (4.9)$$

Based on these orthogonality, the inertia and the stiffness are expressed as diagonal matrix in the Sec. 4.3.4.

As a result, we define the system configuration as $q = [\theta^T, \delta^T]^T \in \mathbb{R}^{n+m}$ where $\delta \in \mathbb{R}^m$ is the time-dependant deflection variable for the flexible load defined in (4.2).

4.3.2 Kinetic Energy of the MAGMaS

To derive Euler-Lagrange equation of the MAGMaS, first, the kinetic energy of the MAGMaS is obtained s.t.,

$$T = T_{arm} + T_{bar} + T_{ar}$$

where T_{arm}, T_{bar}, T_{ar} are the kinetic energies of the manipulator, the flexible load and the aerial robot respectively. Explicit expression of each kinetic

energies are given as following:

$$\begin{aligned}
T_{arm} &= \sum_{i=1}^3 \frac{1}{2} m_i \dot{p}_{c,i}^T \dot{p}_{c,i} + \frac{1}{2} I_{c,i} w_i^2 \\
T_{bar} &= \frac{\rho A}{2} \int_0^{l_b} \dot{p}_f(x)^T \dot{p}_f(x) dx \\
T_{ar} &= \frac{1}{2} m_{ar} p_f^T p_f + \frac{1}{2} I_{ar} w_{ar}^2
\end{aligned}$$

where $p_f(x) \in \mathbb{R}^2$ is the position of the flexible bar along the x -axis of the load frame w.r.t. the inertial frame \mathcal{W} with its expression and the time derivative are given as following

$$\begin{aligned}
p_f(x) &= p_e + R_{\mathcal{L}}^{\mathcal{W}} \begin{bmatrix} x \\ w(x, t) \end{bmatrix} \\
\dot{p}_f(x) &= \dot{p}_e + R_{\mathcal{L}}^{\mathcal{W}} \left(S(\omega_f) \begin{bmatrix} x \\ w(x, t) \end{bmatrix} + \begin{bmatrix} 0 \\ \dot{w}(x, t) \end{bmatrix} \right) \\
&= \underbrace{\left(\begin{bmatrix} J_e & 0 \end{bmatrix} + \begin{bmatrix} R_{\mathcal{L}}^{\mathcal{W}} \begin{bmatrix} -w(x, t) \\ x \end{bmatrix} 1_m^T & e_2 \Phi(x) \end{bmatrix} \right)}_{=: J_f(x) \in \mathbb{R}^{2 \times (n+m)}} \begin{bmatrix} \dot{\theta} \\ \dot{\delta} \end{bmatrix} \quad (4.10)
\end{aligned}$$

where $J_e \in \mathbb{R}^{2 \times n}$ is the robot arm Jacobian for the end-effector, $w_f = \sum_{i=1}^n \dot{\theta}_i$ is the angular velocity of the flexible load frame \mathcal{L} which is same as the angular velocity of the end-effector, $1_m = [1; \cdots; 1] \in \mathbb{R}^m$ is one vector, $e_2 = [0; 1] \in \mathbb{R}^2$ is the unit vector and $\Phi(x) = [\phi_1(x), \cdots, \phi_m(x)] \in \mathbb{R}^m$ is the mode shape row vector at x . Here, recall that we deal with the planar motion, thus we only consider pitch motion for the aerial robot which is expressed as $\bar{\theta}_{ar} \in \mathbb{R}$ and its time derivative $w_{ar} \in \mathbb{R}$.

4.3.3 Potential Energy

The potential energy of the MAGMaS is expressed as the summation of the gravitational potential energies and the elastic potential energy of the flexible load:

$$U = U_{arm} + U_{bar,el} + U_{bar,g} + U_{ar}$$

The gravitational potential energies are expressed as

$$U_{arm} = \sum_{i=1}^n m_i g e_2^T p_{c,i}, \quad U_{ar} = m_{ar} g e_2^T p_f(l_f)$$

$$U_{bar,g} = \rho A g e_2^T \left(p_e + \int_0^{l_b} R_{\mathcal{L}}^{\mathcal{W}} p_f^c(x) dx \right)$$

where $g \in \Re$ is the gravitational acceleration. Note that the position of the aerial robot is same as the load-tip position $p_{ar} = p_f(l_f)$ due to the assumption of $d_{conn} \approx 0$. The elastic energy of the flexible load can be written as

$$U_{bar,el} = \frac{EI}{2} \int_0^{l_b} \left(\frac{\partial^2 w}{\partial x^2} \right)^2 dx = \frac{EI}{2} \sum_{i=1}^m \sum_{j=1}^m d_{ij} \delta_i \delta_j$$

where $d_{ij} := \int_0^{l_b} \phi_i'' \phi_j'' dx$ is satisfying the orthogonality in (4.8).

4.3.4 Euler-Lagrange Dynamics

Using the kinetic T and the potential energy U , the Lagrangian is defined as $L = T - U$. Then, we can derive following Euler-Lagrange dynamics of the

MAGMaS:

$$\begin{bmatrix} M_\theta & M_{\theta\delta} \\ M_{\delta\theta} & M_\delta \end{bmatrix} \ddot{q} + \begin{bmatrix} C_\theta & C_{\theta\delta} \\ C_{\delta\theta} & 0 \end{bmatrix} \dot{q} + g(q) + \begin{bmatrix} 0 & 0 \\ 0 & K \end{bmatrix} q = B(q) \begin{bmatrix} \tau_m \\ \tau_{ar} \end{bmatrix} \quad (4.11)$$

where $M_\theta \in \mathbb{R}^{n \times n}$, $M_\delta \in \mathbb{R}^{m \times m}$, $M_{\theta\delta} = M_{\delta\theta}^T \in \mathbb{R}^{m \times n}$ are the inertia matrix, $C_\theta \in \mathbb{R}^{n \times n}$, $C_{\delta\theta} \in \mathbb{R}^{m \times n}$, $C_{\theta\delta} \in \mathbb{R}^{n \times m}$ are the Coriolis matrix, $g(q) \in \mathbb{R}^{n+m}$ is the gravity force vector, $B(q) \in \mathbb{R}^{(n+m) \times (n+2)}$ is the input mapping matrix, $\tau_m \in \mathbb{R}^n$ is the joint torque and $\tau_{ar} = \lambda R_{ar} e_2 \in \mathbb{R}^2$ is the aerial robot thrust input with the rotation matrix $R_{ar} \in SO(2)$, and the thrust magnitude $\lambda_{ar} \in \mathbb{R}$. The inertia matrix for flexibility M_δ and the stiffness matrix K are constant diagonal matrix where the off-diagonal terms are eliminated by the orthogonality properties (4.8) and (4.9). Note that the aerial robot rotation is independent to above dynamics thanks to the passive rotational joint design of the connector, thus the aerial robot rotational dynamics is excluded in (4.11). We can consider the aerial robot as a rotating thrust generator similar with [13]. The input mapping matrix $B(q)$ have the following structure

$$B(q) = \begin{bmatrix} I_n & J_f^T \\ 0 & B_{\delta,ar} \end{bmatrix}$$

where $I_n \in \mathbb{R}^{n \times n}$ is the identity matrix, J_f is the Jacobian of the load-tip defined in (4.10), $B_{\delta,ar} \in \mathbb{R}^{m \times 2}$ is the input matrix for the flexibility dynamics

with the following expression

$$B_{\delta,ar} = \begin{bmatrix} -\phi_1(l_f) \sin \bar{\theta}_l & \phi_1(l_f) \cos \bar{\theta}_l \\ \vdots & \vdots \\ -\phi_m(l_f) \sin \bar{\theta}_l & \phi_m(l_f) \cos \bar{\theta}_l \end{bmatrix} \quad (4.12)$$

where $\bar{\theta}_l = \sum \theta_i + \theta_l$ is the absolute orientation of the flexible load at the end-effector. From the input mapping matrix $B(q)$, the manipulator control input τ_m cannot directly apply its torque to the flexible load dynamics while the aerial robot input τ_{ar} directly control the flexible load along $B_{\delta,ar}$. Note that the matrix $B_{\delta,ar}$ is rank one matrix along Φ^T although it is m by 2 matrix. Therefore, the m -DoFs flexible load dynamics is under-actuated with rank one input unless the number of the mode shape m is one.

4.4 Control Design

For the MAGMaS, our control objective is the position/orientation trajectory tracking of the flexible load-tip (c.f., rigid object control in previous work [36]). For this control objective, if we only have the robot arm control input τ_m , i.e., the dynamics (4.11) without aerial robot input τ_{ar} , the zero dynamics is unstable [61]. On the other hand, the MAGMaS can overcome this fundamental issue by incorporating the aerial robot as a force generator to the flexible load dynamics as shown in (4.11) with τ_{ar} .

However, as shown in the structure of $B_{\delta,ar}$ in (4.12), we only have rank one control input to stabilize m -dim flexible load vibration dynamics. To resolve this under-actuation problem, we divide this control objective into the

following two sub-problems: 1) slow fully-actuated robot arm control; 2) under-actuated flexible load vibration suppression via the fast aerial robot control. First, for the fully actuated manipulator dynamics, by considering the flexible load at the equilibrium similar to a rigid body, we can design a desired trajectory for the robot arm end-effector $(p_e^d, \bar{\theta}_e^d)$ based on the inverse kinematics. Then, the robot arm is enforced to follow the computed desired trajectory. Next, for the under-actuated flexible load dynamics, since we cannot generate arbitrary control input due to less number of the actuation than the modes of the load flexibility, we perform the controllability analysis for the linearized dynamics by assuming perfect trajectory tracking of the robot arm which is established in first step. Then, we design the vibration suppression controller (i.e., for $\dot{\delta}_i \rightarrow 0$) for the aerial robot. When we compute the equilibrium of the flexible load in the first step, we also design the aerial robot thrust to compensate the deflection at the flexible load-tip $w(l_f) \rightarrow 0$ whose physical meaning is the gravity induced deflection compensation. In the second step, the controllability analysis validate the proposed controller can stabilize vibration near the equilibrium deflection. Here, as the vibration dynamics is relatively faster than end-effector trajectory, this linearization approach is feasible.

4.4.1 Manipulator Control

For the end-effector trajectory tracking of the manipulator, we first transform the joint space dynamics (4.11) into the manipulator workspace dynamics using Jacobian mapping:

$$\dot{\xi} = J_\xi \dot{\theta}, \quad \ddot{\xi} = \dot{J}_\xi \dot{\theta} + J_\xi \ddot{\theta}$$

where $\xi := [p_e, \bar{\theta}_e] \in \mathbb{R}^3$ is the end-effector position/orientation w.r.t. the inertial frame \mathcal{W} , $J_\xi \in \mathbb{R}^{3 \times n}$ is the manipulator Jacobian for the joint angle θ to ξ . Here, we assume the non-redundant manipulator (i.e., $n = 3$) to focus on the cooperative control with the aerial robot rather than deal with the manipulator's redundancy. Then, the MAGMaS dynamics in workspace coordinates can be written as following

$$\begin{aligned} \begin{bmatrix} M_\xi & M_{\xi\delta} \\ M_{\delta\xi} & M_\delta \end{bmatrix} \begin{pmatrix} \ddot{\xi} \\ \ddot{\delta} \end{pmatrix} + \begin{bmatrix} C_\xi & C_{\xi\delta} \\ C_{\delta\xi} & 0 \end{bmatrix} \begin{pmatrix} \dot{\xi} \\ \dot{\delta} \end{pmatrix} + S^T g(q) \\ + \begin{bmatrix} 0 & 0 \\ 0 & K \end{bmatrix} \begin{pmatrix} \xi \\ \delta \end{pmatrix} = S^T B(q) \begin{bmatrix} \tau_m \\ \tau_q \end{bmatrix} \end{aligned} \quad (4.13)$$

where $S = \text{diag}(J_\xi^{-1}, I_m) \in \mathbb{R}^{(n+m) \times (n+m)}$ is transformation matrix. Using this workspace dynamics, we can design following control input

$$\begin{aligned} \tau_m = \bar{M}_\xi \ddot{\xi}_d + \bar{C}_\xi \dot{\xi} + D_e \dot{e} + K_e e - C_{\xi\delta} \dot{\delta} - M_{\xi\delta} \bar{K} \delta + \bar{g}_e \\ - (J_e^{-1} J_b(q) - M_{\xi\delta} \bar{B}_{\delta,ar}) \tau_{ar} \end{aligned} \quad (4.14)$$

where $e = \xi - \xi^d$ is the end-effector position/orientation error, $\bar{M}_\xi = M_\xi - M_{\xi\delta} M_\delta^{-1} M_{\delta\xi}$, $\bar{C}_\xi = C_\xi - M_{\xi\delta} M_\delta^{-1} C_{\delta\xi}$, $\bar{g}_\xi = J_e^{-1} g_\theta - M_{\xi\delta} M_\delta^{-1} g_\delta$, $\bar{K} = M_\delta^{-1} K$ and $D_e, K_e \in \mathbb{R}^{3 \times 3}$ are positive definite control gain matrices. Here, the desired end-effector trajectory can be computed from the desired load-tip trajectory by assuming the deflection is zero (i.e., $w(l_f) = 0$) which is enforced by the aerial robot control. Note that this inverse kinematics is same with the standard manipulator. Then, the closed-loop dynamics for the manipulator workspace

is given as following

$$\bar{M}_\xi \ddot{e} + D_e \dot{e} + K_e e = 0$$

Given closed loop dynamics converges to $e \rightarrow 0$ with positive definite \bar{M}_ξ, D_e, K_e .

Note that the manipulator dynamics is fully-actuated standard robot dynamics, thus the controller can be easily extended to redundant manipulator [62] for $n > 3$ or other controllers (e.g., robust control, adaptive control, etc.).

4.4.2 Flexible Load Dynamics Analysis

From previous section 4.4.1, the proposed robot arm control guarantees $\xi \rightarrow \xi^d$. Therefore, the vibration dynamics can then be rewritten as follows with $\xi = \xi^d$

$$\begin{aligned} \begin{bmatrix} \ddot{\delta} \\ \dot{\delta} \end{bmatrix} &= \begin{bmatrix} 0_m & -M_\delta^{-1}K \\ I_m & 0_m \end{bmatrix} \begin{bmatrix} \dot{\delta} \\ \delta \end{bmatrix} + \begin{bmatrix} M_\delta^{-1}B_{\delta,ar} \\ 0 \end{bmatrix} \tau_{ar} - \begin{bmatrix} M_\delta^{-1}E \\ 0_m \end{bmatrix} \\ &=: \begin{bmatrix} 0_m & -\bar{K} \\ I_m & 0_m \end{bmatrix} \begin{bmatrix} \dot{\delta} \\ \delta \end{bmatrix} + \begin{bmatrix} \bar{B}_{\delta,ar} \\ 0 \end{bmatrix} \tau_{ar} - \begin{bmatrix} \bar{E} \\ 0 \end{bmatrix} \end{aligned} \quad (4.15)$$

where E is defined as

$$E := M_{\delta\xi} \ddot{\xi}^d + C_{\delta\xi} \dot{\xi}^d + g_\delta(\bar{\theta}_e^d)$$

We can further simplify the control input expression using the definition of $B_{\delta,ar}$ in (4.12) and τ_{ar} as following

$$\begin{aligned}\bar{B}_{\delta,ar}\tau_{ar} &= M_{\delta}^{-1}B_{\delta,ar}R(\bar{\theta}_{ar})e_2\lambda_{ar} \\ &= M_{\delta}^{-1}\underbrace{\Phi^T \cos(\bar{\theta}_{ar} - \bar{\theta}_l)}_{=: \bar{b}_{\delta,ar} \in \mathbb{R}^m} \lambda_{ar} = \bar{b}_{\delta,ar}\lambda_{ar}\end{aligned}\tag{4.16}$$

where $R(\bar{\theta}_{ar}) \in SO(2)$ is rotation matrix and $\theta_{ar}^{\mathcal{L}} = \bar{\theta}_{ar} - \bar{\theta}_l$ is the relative orientation of aerial robot w.r.t. the flexible load frame. Recall that $\bar{\theta}_{ar}$ is independently controlled, thus if we regulate $\dot{\theta}_{ar}^{\mathcal{L}} = 0$, then the input mapping vector $\bar{b}_{\delta,ar}$ can be considered as a constant.

4.4.2.1 Linearization

Due to the under-actuation with the rank one aerial robot input $\bar{b}_{\delta,ar}\lambda_{ar}$ for the m -DoFs flexible load dynamics (4.15), we cannot completely cancel out the coupling between the manipulator and the flexible load \bar{E} . Therefore, we design a flexible load vibration/deflection suppression controller with controllability analysis. To analyse controllability, we need to linearize the dynamics (4.15) at the equilibrium deflection $\delta_e \in \mathbb{R}^m$ along the end-effector trajectory ξ^d . Here, we can assume relatively slow manipulator end-effector motion than vibration (i.e., $\dot{\xi} \ll \dot{\delta}$) because the robot arm can generate desired velocity for the load-tip with slow manipulator end-effector motion as length of the load increases.

We aim to behave the flexible load similar to the rigid body, thus the control objective of the aerial robot includes both the vibration suppression $\dot{\delta} = 0$ and

the deflection compensation $w(l_f) = 0$. Note that zero deflection at the tip $w(l_f) = 0$ does not imply zero deflection for all location along the load (i.e., not $\delta_i(x) = 0$ for all x). Therefore, $w(l_f) = 0$ is the equilibrium point of the linearized flexible load dynamics which is also the assumption of the inverse kinematics of $(p_e^d, \bar{\theta}_e^d)$ in Sec. 4.4.1.

First of all, we design a feedforward control input to compensate the gravity force at the equilibrium deflection δ_e to satisfy $w(l_f) = 0$. The equilibrium deflection satisfies following equality

$$K\delta_e + g_\delta(\theta) = b_{\delta,ar}\lambda_{ar}$$

We then get the following expression for the deflection $w(l_f)$ by multiplying ΦK^{-1}

$$\Phi\delta_e = \Phi K^{-1}(b_{\delta,qr}\lambda_{ar} - g_\delta(\theta))$$

Then, the control input for the gravity induced deflection compensation can be proposed as

$$\lambda_{ar} = (\Phi K^{-1}b_{\delta,ar})^{-1}\Phi K^{-1}g_\delta \quad (4.17)$$

Note that stiffness matrix K is a diagonal invertible matrix, thus $\Phi K^{-1}b_{\delta,ar} = \sum \phi_i^2(l_f)/K_{ii} \cos(\theta_{ar}^{\mathcal{L}})$ is also invertible unless $\cos(\theta_{ar}^{\mathcal{L}}) = 0$. Then, the equilibrium deflection vector δ_e can be written as following

$$\delta_e = (-I + K^{-1}b_{\delta,ar}(\Phi K^{-1}b_{\delta,ar})^{-1}\Phi)K^{-1}g_\delta(\theta)$$

Note that the equilibrium deflection δ_e enforced by λ_{ar} satisfies zero deflection at the load-tip, i.e., $w(l_f) = \Phi\delta_e = 0$.

Finally, we can linearize the dynamics (4.15) at the equilibrium deflection δ_e

$$\begin{bmatrix} \ddot{\tilde{\delta}} \\ \dot{\tilde{\delta}} \end{bmatrix} = \underbrace{\begin{bmatrix} 0_m & -\bar{K} \\ I_m & 0_m \end{bmatrix}}_{=:A} \begin{bmatrix} \dot{\tilde{\delta}} \\ \tilde{\delta} \end{bmatrix} + \underbrace{\begin{bmatrix} \bar{b}_{\delta,ar} \\ 0 \end{bmatrix}}_{=:B} \bar{\lambda}_{ar} \quad (4.18)$$

where $\tilde{\delta} = \delta - \delta_e$ and $\bar{\lambda}_{ar} = \lambda_{ar} - (\Phi K^{-1} b_{\delta,ar})^{-1} \Phi K^{-1} g_\delta$.

4.4.2.2 Controllability

The linearized flexible load dynamics (4.18) is represented by $2m$ configurations $(\dot{\tilde{\delta}}, \tilde{\delta})$ with the rank one aerial robot input $B\lambda_{ar}$. Therefore, we need to verify whether the input $B\lambda_{ar}$ can suppress the vibration/deflection to the equilibrium $(\dot{\tilde{\delta}}, \tilde{\delta}) \rightarrow (0,0)$ in the linearized system before designing a controller. For this, we utilize the controllability matrix \mathcal{C} of the linearized deflection dynamics (4.18) defined as following

$$\mathcal{C} := [B \ AB \ \cdots \ AB^{m-1}] \in \mathfrak{R}^{2m \times 2m}.$$

Combining with (4.18), the controllability matrix \mathcal{C} can be written as

$$\mathcal{C} = \begin{bmatrix} \bar{b}_{\delta,ar} & 0 & \cdots & (-\bar{K})^{m-1} \bar{b}_{\delta,ar} & 0 \\ 0 & \bar{b}_{\delta,ar} & \cdots & 0 & (-\bar{K}^{m-1}) \bar{b}_{\delta,ar} \end{bmatrix} \quad (4.19)$$

The given linearized flexible load dynamics (4.18) is controllable, if the controllability matrix satisfies $\text{rank}(\mathcal{C}) = 2m$.

To figure out the condition for the controllability, we need to check the condition for $\det(\mathcal{C}) \neq 0$. Here, we can simplify the evaluation of $\det(\mathcal{C})$ by utilizing the column permutation of the matrix \mathcal{C} which only have impact on the sign of the determinant. Using the column permutation, we can collect all the odd columns and even columns, then the controllability matrix \mathcal{C} can be expressed as block diagonal matrix of following submatrix \mathcal{C}_s :

$$\mathcal{C}_s = \begin{bmatrix} \bar{b}_{\delta,ar} & \bar{K}\bar{b}_{\delta,ar} & \cdots & \bar{K}^{m-1}\bar{b}_{\delta,ar} \end{bmatrix}$$

From the property of block diagonal matrix, $|\det(\mathcal{C})| = |\det(\mathcal{C}_s)|^2$, thus we only need to analyse $\det(\mathcal{C}_s)$. The determinant of \mathcal{C}_s is described in the following Lemma.

Lemma 2. Consider the submatrix of the controllability matrix \mathcal{C}_s of the linearized system (4.18). Then the determinant of the matrix \mathcal{C}_s satisfies following equation

$$\det(\mathcal{C}_s) = \prod_{i=1}^m \bar{b}_i \cdot \prod_{j=1}^m \left(\frac{EI d_{jj}}{M_{\delta,jj}} - \frac{EI d_{(j+1)(j+1)}}{M_{\delta(j+1)(j+1)}} \right) \quad (4.20)$$

where \bar{b}_i is i -th component of $\bar{b}_{\delta,ar}$, $M_{\delta,ii}$ is (i, i) component of the inertia matrix M_{δ} and $d_{ii} = \int \phi_i''(x)^2 dx$. If $j = m$, then $j + 1$ is considered as 1.

Proof: If $m = 2$, we can compute $\det(\mathcal{C}_s)$ as following

$$\det(\mathcal{C}_s) = \begin{vmatrix} \bar{b}_1 & \frac{EId_{11}}{M_{\delta,11}} \bar{b}_1 \\ \bar{b}_2 & \frac{EId_{22}}{M_{\delta,22}} \bar{b}_2 \end{vmatrix} = \bar{b}_1 \bar{b}_2 \left(\frac{EId_{22}}{M_{\delta,22}} - \frac{EId_{11}}{M_{\delta,11}} \right)$$

Next, we assume (4.20) is satisfied for $m = n - 1$. If this relations is also available for $m = n$, then the equation (4.20) is satisfied for any positive integer m . For $m = n$ the determinant is given as following

$$\begin{aligned} \det(\mathcal{C}_s) &= \left| \bar{b}_{\delta,ar} \quad \bar{K} \bar{b}_{\delta,ar} \quad \dots \quad \bar{K}^{n-1} \bar{b}_{\delta,ar} \right| \\ &= \det \left(\text{diag}(\bar{b}_1, \dots, \bar{b}_n) \cdot \begin{bmatrix} 1_n & \bar{K} 1_n \dots \bar{K}^{n-1} 1_n \end{bmatrix} \right) \\ &= \prod_{i=1}^n \bar{b}_i \cdot \underbrace{\det \left(\begin{bmatrix} 1_n & \bar{K} 1_n \dots \bar{K}^{n-1} 1_n \end{bmatrix} \right)}_{=: \mathcal{K}_n} \end{aligned}$$

where $1_n = [1, \dots, 1]^T \in \mathfrak{R}^n$ is n -dim one vector. First term of right hand side is same with (4.20), thus we need to verify second term. According to Laplace's formula, determinant of matrix is expressed as summation of determinant of

submatrices

$$\begin{aligned}
\det(\mathcal{K}_n) &= \sum_{j=1}^n (-1)^{(j+1)} \det(\mathcal{K}_{n,(1,j)}) \\
&= \sum_{j=1}^n (-1)^{(j+1)} \left| \bar{K}_{(j,j)} 1_{n-1} \quad \cdots \quad \bar{K}_{(j,j)}^{n-1} 1_{n-1} \right| \\
&= \sum_{j=1}^n (-1)^{(j+1)} \left| \bar{K}_{(j,j)} \right| \cdot \left| 1_{n-1} \quad \cdots \quad \bar{K}_{(j,j)}^{n-2} 1_{n-1} \right| \\
&= \sum_{j=1}^n (-1)^{(j+1)} \det(\bar{K}_{(j,j)}) \det(\mathcal{K}_{n,(n,j)}) \\
&= \sum_{j=1}^n (-1)^{(j+1)} \prod_{\substack{i=1 \\ i \neq j}}^n w_{n,i} \cdot \prod_{\substack{i=1 \\ i \neq j}}^n (w_{n,i} - w_{n,i+1}) \tag{4.21}
\end{aligned}$$

where $\mathcal{K}_{n,(i,j)}, \bar{K}_{(i,j)} \in \mathbb{R}^{(n-1) \times (n-1)}$ are matrices whose i -th column and j -th row are eliminated from the original matrices \mathcal{K}_n, \bar{K} and $w_{n,i} := EId_{ii}/M_{\delta,ii}$ is the natural frequency of i -th mode. For the last equation, every $w_{n,i}$ have $(n-1)$ -order. If we consider this equation as a function of $w_{n,i}$ (i.e., $f(w_{n,i}) = 0$), then $(n-1)$ order polynomial function have $(n-1)$ solutions. It is straightforward to show $w_{n,i} = w_{n,j} \ \forall j \in \{1, \dots, i-1, i+1, \dots, n\}$ are the solutions of this polynomial equation using (4.21) by substituting it to solution. As a result, equation (4.20) is satisfied for $m = n$ and, thus, satisfied for any positive integer m . ■

From Lemma 2, the three conditions to ensure controllability of the linearized system can be extracted in the following theorem:

Theorem 3. Consider the linearized flexible load dynamics (4.18) and controllability matrix \mathcal{C} . Then, if the following three conditions are met, the linearized

flexible load dynamics is controllable:

- 1) **Design condition** $\phi_i(l_f) \neq 0, \forall i = 1, \dots, m$;
- 2) **Control condition** $\cos(\theta_{ar}^{\mathcal{L}}) \neq 0$, i.e., $\theta_{ar}^{\mathcal{L}} \neq \frac{\pi}{2} + k\pi, k \in \mathcal{Z}$;
- 3) **Physical condition** $\frac{EId_{ii}}{M_{\delta,ii}} \neq \frac{EId_{jj}}{M_{\delta,jj}}$ (or $w_{n,i} \neq w_{n,j}$).

Proof: According to Lemma 2, $\det(\mathcal{C}_s)$ is represented as product of \bar{b}_i and $\frac{EId_{ii}}{M_{\delta,ii}} - \frac{EId_{jj}}{M_{\delta,jj}}$. The conditions for $\det(\mathcal{C}_s) = 0$ are induced by $\bar{b}_i = 0$ or $w_{n,i} = \frac{EId_{ii}}{M_{\delta,ii}} = \frac{EId_{jj}}{M_{\delta,jj}} = w_{n,j}$. From the expression of \bar{b}_i in (4.16) and given that $M_\delta > 0$, we can conclude the condition translates to $\phi_i(l_f) = 0$ and/or $\cos(\theta_{ar}^{\mathcal{L}}) = 0$ which are the design and the control condition. The later one directly correspond to the physical condition. ■

To satisfy the design condition, the mode shape at the aerial robot attachment position should not be zero, i.e., $\phi_i(l_f) \neq 0$. This controllability condition enforces a design criteria for attaching the aerial robot to avoid the node position, i.e., $\phi_i(x) = 0, \forall i = 1, \dots, m$. This design condition is valid for our one aerial robot case of the MAGMaS whose aerial robot is connected at the flexible load tip (i.e., $x = l_f$). This conditions can also be applied to the MAGMaS with multiple aerial robots.

If the aerial robot cannot meet the control condition, i.e., $\cos(\theta_{ar}^{\mathcal{L}}) = 0$ or $\theta_{ar}^{\mathcal{L}} = \frac{\pi}{2} + k\pi, k \in \mathcal{Z}$, then the thrust of the aerial robot is aligned to x -axis of the load frame \mathcal{L} and subsequently cannot exert force along the deflection direction. This controllability condition impose to control the aerial robot

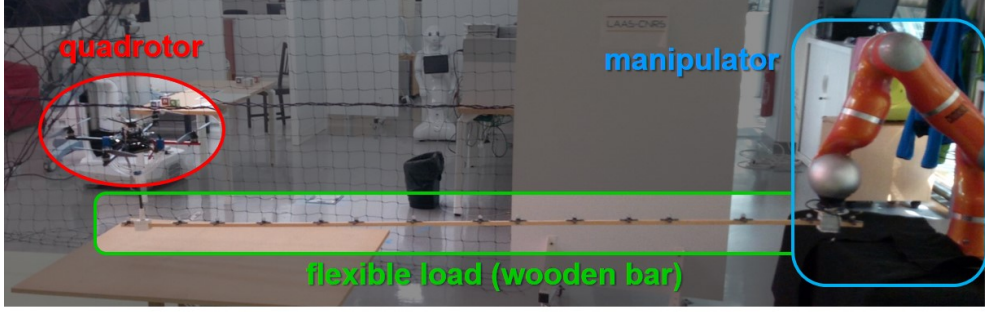


FIGURE 4.4: Ongoing experimental setup for the MAGMaS with a quadrotor, a flexible load and a manipulator.

orientation to $\cos(\theta_{ar}^{\mathcal{L}}) \neq 0$. In this chapter, to preserve the control condition and to maximize the thrust input along the deflection of the flexible load, we control the aerial robot attitude to $\bar{\theta}_{ar} = \bar{\theta}_l$, i.e., $\cos \bar{\theta}_{ar}^{\mathcal{L}} = 1$.

The physical condition represents identical natural frequency between two different modes. Physically, two vibration modes with identical natural frequency represented as one combined vibration mode. Mathematically, we compute unique vibration mode for each distinct natural frequencies. Therefore, this condition is always satisfied.

4.4.3 Aerial Robot Control

Vibration suppression can be achieved by the aerial robot control input $\bar{b}_{ar,\delta}\lambda_{ar}$ based on the controllability analysis. Then, we design two independent control: 1) the aerial robot orientation control for the thrust aligning; 2) the vibration suppression control for the flexible load using the aerial robot thrust. Recall that these two independent controller are available due to the independent

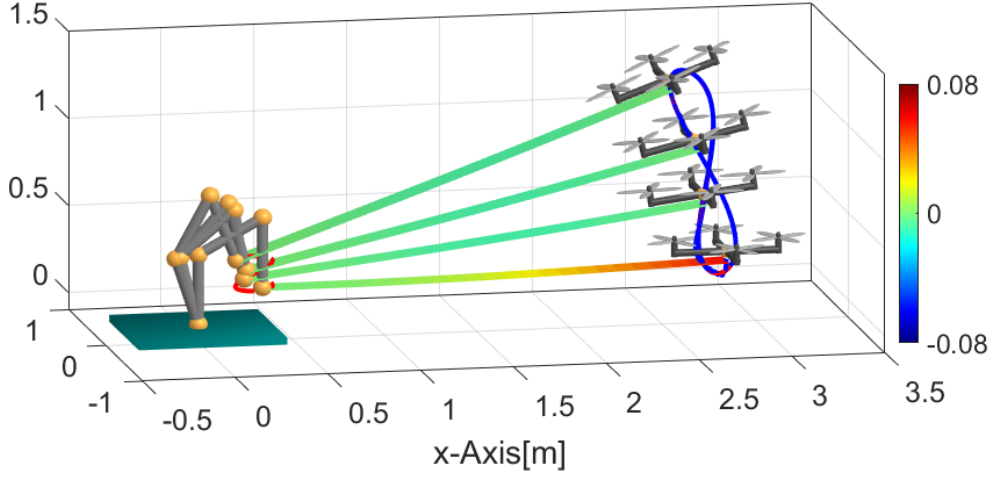


FIGURE 4.5: Snapshot of the eight-shaped trajectory tracking with proposed controller. Color in the flexible load represents its relative deflection w.r.t. a rigid load.

rotational dynamics of the aerial robot thanks to the passive rotational joint connector. This rotational joint cannot exert torque to the flexible load.

First, we design aerial robot orientation controller to align thrust direction to the perpendicular direction of the flexible load (i.e., y -direction of the flexible load frame \mathcal{L}). The control objective is expressed as $\bar{\theta}_{ar} \rightarrow \bar{\theta}_l$. This control objective maximize magnitude of the input vector $b_{\delta,ar}$ for the load vibration. For the planar case, the orientation control of the angular rate controlled aerial robot is given as following

$$\dot{\theta}_{ar} = \dot{\bar{\theta}}_e^d + k(\bar{\theta}_l^d - \bar{\theta}_{ar})$$

where $\bar{\theta}_l^d = \bar{\theta}_e^d + \theta_l$ is the desired load orientation with constant θ_l , $\dot{\bar{\theta}}_l = \dot{\bar{\theta}}_e$

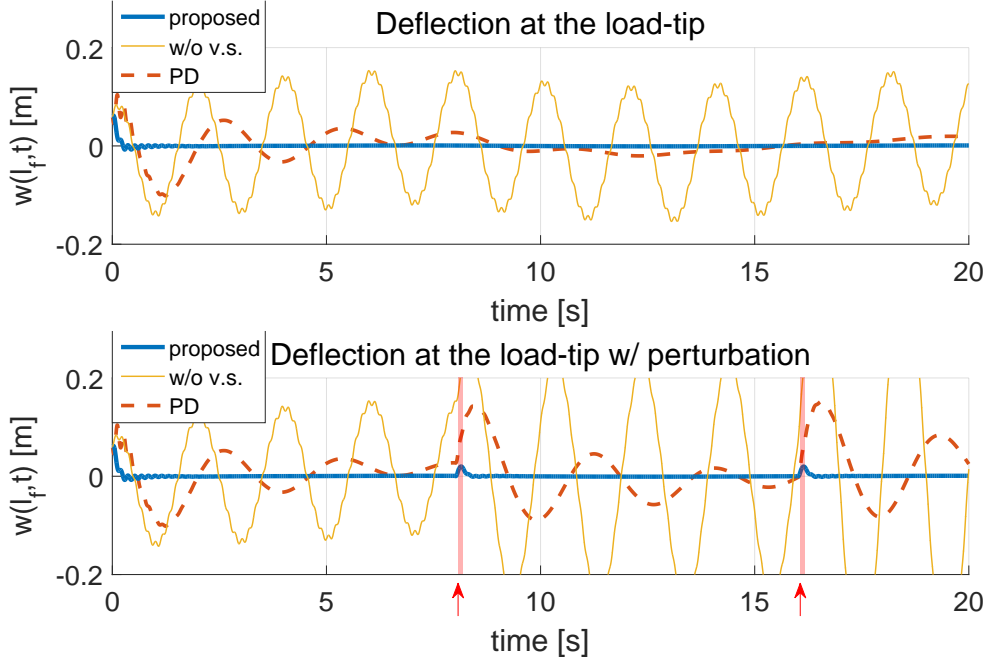


FIGURE 4.6: Simulation results with three different controllers: 1) proposed control; 2) PD control; 3) manipulator control w/o vibration suppression. Trajectory tracking (top) and tracking with perturbation (bottom). An external force is applied to at 8, 16s for the bottom.

and k is control gain. Note that angular velocity controlled aerial robot can capture many commercially available UAV [8]. For the torque controlled aerial robot, we can exploit a control design proposed in [10].

Next, using the linearized flexible load dynamics and the controllability analysis in Sec. 4.4, we can design various linear controller to suppress the vibration. Here, we utilize LQR (linear quadratic regulator) to optimally suppress vibration in the MAGMaS.

$$\lambda_{ar} = K_{LQR} \begin{bmatrix} \dot{\bar{\delta}} \\ \bar{\delta} \end{bmatrix} + (\Phi K^{-1} b_{\delta, ar})^{-1} \Phi K^{-1} g_{\delta} \quad (4.22)$$

where $K_{LQR} \in \mathbb{R}^{1 \times 2m}$ is the control gain based on LQR.

4.5 Simulation

To verify the performance of the proposed control scheme, we conduct a set of two simulations. In these simulations, the system parameters are based on real platform data and are as follow: 1) inertia parameters $(m_1, m_2, m_3, m_l, m_{ar}) = (4, 4, 4, 0.591, 1)kg$ and moment of inertia are evaluated as rectangular bar; 2) length $(l_1, l_2, l_3, l_f) = (0.4, 0.4, 0.4, 2.5)m$; 3) bar properties $EI = 51.3Nm^2$, $\rho A = 0.205kg/m$. From this load property, its natural frequencies are given as $(w_{n,1}, w_{n,2}) = (1.44, 8.98)Hz$ which are experimentally retrieved via vibration excitation and FFT analysis. We only consider the first 2-modes as the other higher frequency modes are negligible in our identification experiments. Here, we utilize two vibration modes $m = 2$ from our preliminary experiments of the wooden load vibration. From the third to higher modes, the magnitude of vibration is negligible and suppressed fast by its own damping.

For the simulation, we assume that the deflection of each modes δ_i is available. In practice, we can indirectly measure the mode deflection by measuring $w(x, t)$ using MoCap or strain gage for several different points as following

$$\begin{bmatrix} w(x_1, t) \\ w(x_2, t) \end{bmatrix} = \underbrace{\begin{bmatrix} \phi_1(x_1) & \phi_2(x_1) \\ \phi_1(x_2) & \phi_2(x_2) \end{bmatrix}}_{=:\Phi_{12}} \begin{bmatrix} \delta_1(t) \\ \delta_2(t) \end{bmatrix}$$

where x_i are the points which makes non-zero determinant of matrix Φ_{12} .

The first simulation consists in a trajectory tracking task. As mentioned in Sec. 4.4, we can design the trajectory of the end-effector by considering the flexible load as rigid body. Here, the trajectory is given as $(x_e^d, y_e^d, \bar{\theta}_e) = (0.1 \sin(t), 0.1 \cos(0.5t), 0.2 \sin(0.5t))$. To validate our approach, we compare three different controllers for this trajectory tracking task: 1) proposed controller in (4.14) and (4.22); 2) manipulator controller without vibration suppression: τ_m is same with (4.14) and λ_{ar} is same with (4.17); 3) PD control in [43]: λ_{ar} is same with (4.17) and τ_m satisfies

$$\tau_m = \bar{M}_\xi \ddot{\xi}_d + D_e \dot{e} + K_e e + \bar{g}_e - (J_e^{-1} J_b(q) - B_{\delta, ar}) \tau_{ar}$$

For controller 2 and 3, the aerial robot input is just gravity compensation of the flexible load and the aerial robot. The simulation result are gathered in Fig. 4.6. Under the tracking controller 2, vibration is not suppressed while control 3 and the proposed controller is suppressing the vibration. Controller 3 can suppress the vibration, however it only relies on energy dissipation, the convergence time is slower than our proposed controller which can directly suppress the vibration using the aerial robot control input τ_{ar} .

The second simulation in Fig. 4.6 includes perturbations by an external force on the load-tip. The perturbations are given as $(f_x, f_y) = (5, 15)N$ at $t = 8s$ and $t = 16s$ during $0.05s$. In this plot, we exclude the result of controller 2 whose vibration amplitude is too large to compare. Similar to the first simulation, after the perturbation, both controller 3 and our proposed controller can suppress the vibration although the convergence is much slower for controller 3.

Those two simulations validate our proposed approach to leverage MAGMaS's heterogeneous design, by exploiting the aerial robot control input, trajectory tracking performances are increased.

4.6 Conclusion

In this chapter, we extend results on the MAGMaS, a novel cooperative heterogeneous manipulation system [36], to the case of flexible load manipulation. In particular, we derive the dynamical model of a planar MAGMaS, including vibrations in the long slender load. We then propose a control strategy for both trajectory tracking and effective vibration cancellation by exploiting the dynamical properties of such an under-actuated system for vibration, in particular vibration cancellation is achieved through a linearization scheme. Along the way, the conditions for controllability of the vibrations modes are exhibited. The validity of this approach is demonstrated in two simulations by comparing its performance to the one of previously proposed approaches.

Chapter 5

Rotor-based Vibration Suppression Module

5.1 Introduction

Large-size object transport and manipulation are one of the important tasks in industries, thus, these tasks also have been tried to be partially or fully handled by robotic systems typically in the assembly line in manufacturing. Regarding large-size object manipulation, there are several attempts to bring the robotic system to the outside of the factory using multiple robots [63–65]. Recently, ETHZ demonstrates a structure construction by assembling steel rebar, timber, and blocks using robotic manipulator [66]. ATOUN is proposed to assist human workers to transport a heavy object [67].

However, the above-mentioned results are limited in rigid object manipulation. On the other hand, these large-size objects often include long/slender object, such as bar, beam, and pipe. For this long/slender object handling, an induced torque by center-of-mass far from the grasping location is crucial



FIGURE 5.1: Cooperative manipulation of flexible object composed of one ground manipulator and distributed RVMs (Robot-based Vibration suppression Module).

as well as its high payload. As the length of the object gets longer, the deflection and the vibration become significant, thus it is hard to be handled by the conventional robotic system and possibly hazardous due to undesirable vibration.

In this chapter, we propose a robot-based vibration suppression modules (RVM) which is optimally designed to manipulate the large flexible object while suppressing its vibration. Since the RVM is easily attachable/detachable to the object, an arbitrary number of the distributed RVMs can be adapted to various length/shape/weight of object. The system composition of the RVM is partly motivated by our previous result of MAGMaS (Multiple Aerial-Ground Manipulator System) [44], which utilizes a single quadrotor at the flexible load-tip. However, the quadrotor requires mechanically complicated and large payload structure, e.g., passive rotational joint, to connect the object while allowing free rotation. Besides, the quadrotor is optimized for flying capability

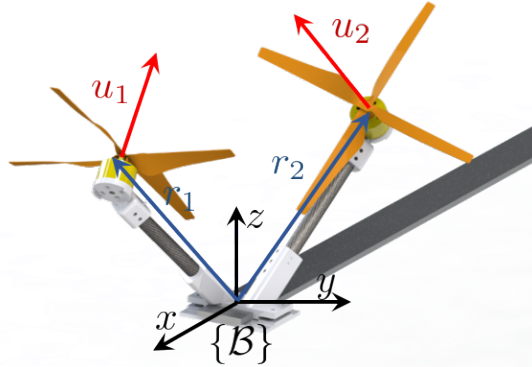


FIGURE 5.2: Optimized design and rotor allocation of RVM.

in terms of the number of the rotors and its allocation [7]. The design and distributed actuation principles are partly inspired by ODAR (Omni-Directional Aerial Robot) [34] and LASDRA (Large-size Aerial Skeleton System with Distributed Rotor Actuation) [35, 45]. In these two results, the aerial robots are composed of distributed unit modules designed to maximize control wrench for omni-directional flying on each rigid link while the RVM is designed for vibration suppression of flexible object with a more simplified and compact design.

We aim the role of the RVM as follows: 1) vibration suppression of the flexible load; and 2) object weight sharing to support limited ground manipulator torque. Therefore, we first provide a novel RVM design by optimizing the thrust generation along the sagittal plane while minimizing undesirable wrench along other directions based on constrained optimization. Here, we utilize two rotors which is the minimum number that can generate control actuation along $E(2)$. Since an arbitrary number of the RVM can be utilized, we derive the system dynamics for arbitrary number of RVM and show that the flexible load dynamics is composed of linear diagonal matrices even with multi-modules. In

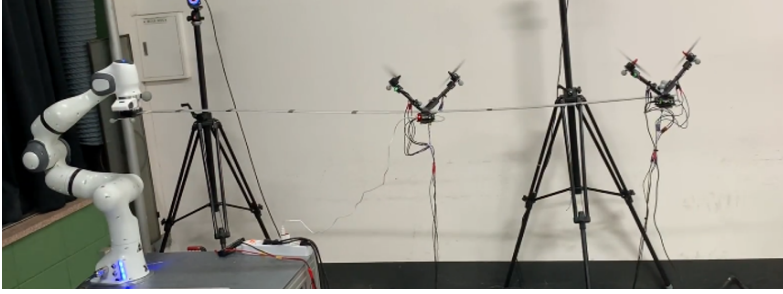


FIGURE 5.3: Cooperative manipulation of flexible object composed of one ground manipulator and distributed two RVMs.

the control problem, since the number of vibration modes and RVM can be arbitrary and this might induce controllability issue, thus we come up with controllability condition and elucidate its physical meaning for the distributed RVMs thanks to dynamic structure similar to [44]. Furthermore, we provide not only the place not to allocate the RVM based on controllability but also the place the RVM needs to be allocated to maximize vibration suppression capability based on controllability gramian. Experiments are performed to demonstrate the effectiveness of the proposed theory and RVM.

5.2 Robot-based Vibration Suppression Modules Design

5.2.1 System Description

We recall the composition of distributed RVMs and a ground manipulator for the flexible object manipulation. A manipulation system consists of a n -degrees of freedom (dof) ground manipulator, a load/object to be manipulated and

distributed RVMs connected to the load, see Fig. 5.8. This system is proposed to overcome the limitation of approaches with quadrotor [36, 44, 68] by taking advantages of distributed modules with rotor actuation: 1) optimized design and simplified structure for manipulation and vibration suppression; and 2) dealing with large and flexible objects with distributed RVMs.

We assume a manipulated object as a long bar with skewed rectangular shape cross-section so that the transverse vibration is substantial only, while that along the others are negligible. We also confine ourselves to the case of planar manipulation for simplicity and the results are extendable to more general cases of course. We do not limit the location and the number of RVMs connected to the flexible load (c.f., one-quadrotor at the bar-end [44]). The RVM is rigidly connected to the flexible load through screw tightening mechanisms. This simple connection structure provides lighter and smaller RVM compared to a passive rotational joint in [44].

The actuation property of the rotor that generates both thrust force and moment along the rotor rotation axis makes the design problem non-trivial. Here, we consider to use the thrust force for vibration suppression control, then an undesirable torque can affect to other direction, e.g., a torsional torque. Therefore, we should consider both maximizations of the thrust force in the sagittal plane and minimization of the torsional torque. Different from the conventional multirotor drone, the RVM does not necessary to have at least four rotors for flying capability, thus we utilize only two rotors for RVM which is sufficient to provide control input in $E(2)$ to minimize the number of rotors while realizing the compact and lightweight design.

5.2.2 Design Optimization

The goal of module design optimization is to specify the optimal attaching location of each rotor $r_i \in \mathbb{R}^3$ and the respective thrust generation direction $u_i \in \mathbb{R}^3$ all expressed in the RVM body frame \mathcal{B} . The search space of the optimization is then given by $\mathcal{U} := \{u_i \in \mathbb{R}^3 | |u_i| = 1, i = 1, 2\}$ and $\mathcal{R} := \{r_i \in \mathbb{R}^3 | |r_i| \leq r_{max}, i = 1, 2\}$ where \mathcal{U} and \mathcal{R} are the set of the thrust direction vectors and the location vectors, respectively, the condition $|u_i| = 1$ is used to let $u_i \in S^2$, and r_{max} is the maximum allowable length for all the rotor locations. Here, we set $r_{max} = 0.15m$. Our design procedure presented here can also be extended for other numbers of rotors as well.

We can then formulate the design optimization problem as a constrained optimization problem s.t.

$$(u_1^*, u_2^*, r_1^*, r_2^*) := \arg \max_{u, r} (u_1 \times u_2)^T e_y \quad (5.1)$$

$$\text{subj. to } u_i \in \mathcal{U}, \quad r_i \in \mathcal{R} \quad (5.2)$$

$$(r_i \times u_i + \gamma u_i) \cdot e_x = 0, \quad \sum r_i \times e_z = 0 \quad (5.3)$$

$$\frac{|(r_1 - r_2) \cdot (u_1 \times u_2)|}{|u_1 \times u_2|} \geq d_{aero} \quad (5.4)$$

where $(\cdot)^*$ is optimal value, γ is thrust to moment ratio and $e_x, e_y, e_z \in \mathbb{R}^3$ are unit vector of corresponding axis. The thrust generated by two rotors renders a plane whose normal vector is $u_1 \times u_2$ while its area is $|u_1 \times u_2|$. The bigger area means the bigger thrust generation capability along the plane. Therefore, to maximize thrust generation capability along xz -plane, we project this area into xz -plane for the cost function (5.1). Each constraints stand for

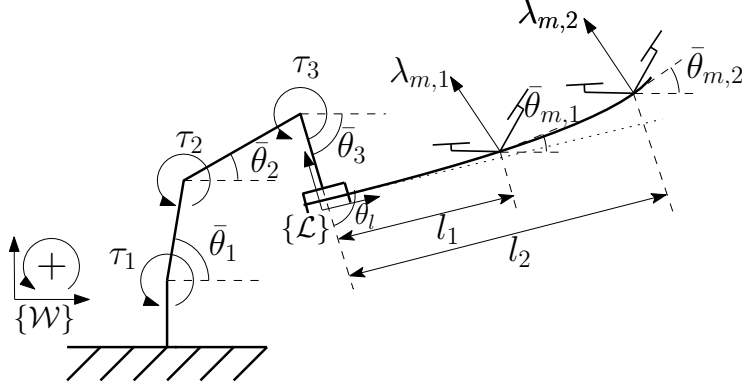


FIGURE 5.4: Sketch of the configuration of the system.

following conditions: (5.2) constrain unit direction vector $u_i \in S^2$ and limit the maximum volume of the rotor location; (5.3) balance torsional torque around x -axis induced by rotor thrust and moment to prevent torsional deflection of the flexible load and balance torsional torque around x -axis induced by weight of the acuator; and (5.4) constrains the airflow interference among rotors by ensuring the distance among their airflow larger than a certain value d_{aero} . (5.4) represents the shortest distance between the center axis of the cylinder produced by airflow. As shown in [34], if the distance between two rotors is longer than a certain value d_{aero} , the airflow interference can be negligible. We solve this constrained optimization and the resultant RVM design is illustrated in Fig. 5.2.

5.3 Dynamics Modeling with Multiple Distributed RVMs

From the sketch in Fig. 5.4, we detail the notations used throughout the chapter. On the ground, n -dof robot arm is mounted whose joint configuration is defined as $\theta \in \mathbb{R}^n$. The position of each joint, the center-of-mass of each links and end-effector of robot arm w.r.t. the inertial frame \mathcal{W} are defined as $p_i^{\mathcal{W}}, p_{c,i}^{\mathcal{W}} \in \mathbb{R}^2$ and $p_e^{\mathcal{W}} \in \mathbb{R}^2$ respectively. For brevity, we will omit the \mathcal{W} when the position is represented in the inertial frame. Define the position and the orientation of the RVM attached along the flexible load w.r.t. \mathcal{W} as $p_{m,i} \in \mathbb{R}^2$ and $\theta_{m,i} \in \mathbb{R}$. For any angle, e.g. θ , the notation $\bar{\theta}$ represents the absolute angle, e.g., $\bar{\theta}_i = \sum_{j=1}^i \theta_j$, while θ representing relative angle throughout this chapter.

The flexible load is rigidly attached to end-effector of the robot arm, thus relative angle between the end-effector and the flexible load is constant θ_l . As shown in Fig. 5.5, the position and orientation of the flexible load along the x -axis w.r.t. the flexible load frame \mathcal{L} at time t can be written as $p_f^{\mathcal{L}}(x, t) = [x; w(x, t)]$ and $\theta_f(x) = \frac{\partial w(x, t)}{\partial x}$ where $w(x, t)$ is the deflection along z -direction at x in \mathcal{L} . Recall that the RVMs are rigidly attached to the flexible load at the user determined location. At the given location, the RVM can be considered as a thrust generator along the sagittal plane. Thanks to the RVM design in 5.2.2, the resultant thrust direction $\theta_{t,i}$ can be arbitrarily determined.

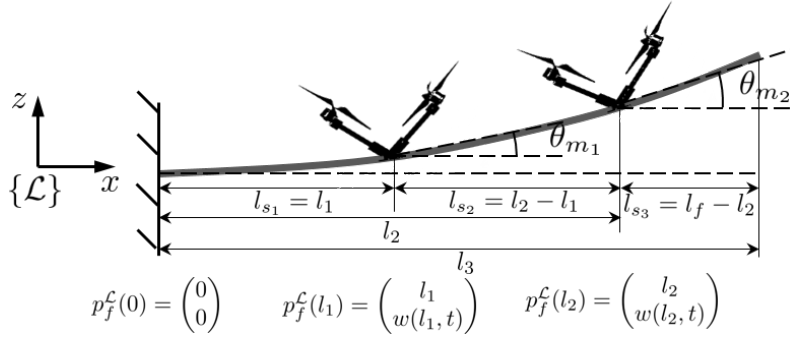


FIGURE 5.5: Euler-Bernoulli beam deflection model.

5.3.1 Flexibility Modeling of the Load

To model vibration of the flexible load, here, we adopt Euler-Bernoulli beams theory [59], whose governing equation is $\rho A \frac{\partial^2 w(x, t)}{\partial t^2} + \frac{\partial^2}{\partial x^2} EI \frac{\partial^2 w(x, t)}{\partial x^2} = 0$ where E, I, ρ, A are Young's modulus, the second moment of area, the density and the intersection area of the flexible load respectively. We assume the constant parameters along the flexible load to simplify the beam model and to meet the practical objects. Using the separation of variables, a solution of given partial differential Euler-Bernoulli equation can be written s.t. $w(x, t) = \sum_{i=1}^m \phi_i(x) \delta_i(t) =: \Phi(x) \delta(t)$ where m is the number of assumed vibration modes, $\phi_i(x)$ is the time invariant mode shape function, $\delta_i(t)$ describes the time varying part of the deflection associated with given mode shape $\phi_i(x)$, $\Phi := [\phi_1, \dots, \phi_m] \in \mathbb{R}^m$ and $\delta := [\delta_1; \dots; \delta_m] \in \mathbb{R}^m$ are the corresponding row and column vector. In practice, high frequency modes are suppressed quickly due to their damping. thus, finite dimension m of the vibration modes are considered. As a result, we define the system configuration as $q = [\theta^T, \delta^T]^T \in \mathbb{R}^{n+m}$.

The attached location of the RVM can be arbitrarily chosen by the user, therefore, the flexible load model should be derived to adopt arbitrary number of the RVM at arbitrary location. Since each RVM is rigidly attached to flexible beam, the RVM provides substantial mass and moment of inertia at attached location. Therefore, to solve Euler-Bernoulli equation, the mass and the moment of inertia of each RVM should also be incorporated to the boundary condition: $M_{s_{i-1}}(l_{s_{i-1}}) = M_{s_i}(0) + \mathcal{I}_{m,i} \frac{\partial \ddot{w}_s}{\partial x} \big|_{x=0}$ and $V_{s_{i-1}}(l_{s_{i-1}}) = -m_{m,i} \ddot{w}_s(0) + V_{s_i}(0)$ where $M(x) = E \frac{\partial^2 w}{\partial x^2}$ is the moment and $V(x) = -EI \frac{\partial^3 w}{\partial x^3}$ is the shear force and the subscript s_i represent i -th segments divided by $(i-1)$ -th and i -th module with $l_0 = 0$ and $l_{n_m+1} = l_f$ as illustrated in Fig. 5.4 and Fig. 5.5. Therefore, the flexible load is divided into $n_m + 1$ segments. Since the length of the RVM module ($l \approx 0.05m$) is typically smaller than the length of manipulated flexible beam ($l_f > 1m$), the RVM location is approximately expressed as a point along x -axis. Then, the solution can be computed by simultaneously solving the Euler-Bernoulli equation of all segments. Note that the resultant mode shapes of all the segments are the eigenfunctions of the Euler-Bernoulli equation, thus the integration along the overall length still hold orthogonality between each mode shape for $i \neq j$ s.t.:

$$\begin{aligned} \int_0^{l_f} \phi_{ij}''(x) dx &= 0 \\ \rho A \int_0^{l_f} \phi_{ij}(x) dx + \sum_{k=1}^{n_m} (m_{m,k} \phi_{ij}(l_k) + \mathcal{I}_{m,k} \phi_{ij}'(l_k)) &= 0 \end{aligned} \quad (5.5)$$

where $\phi_{ij} := \phi_i \phi_j$ and $m_{m,i}, \mathcal{I}_{m,i}$ are mass and moment of inertia of i -th RVM.

5.3.2 Euler-Lagrange Dynamics

Using the kinetic energy T and the potential energy U , the Lagrangian is defined as $L = T - U$. This Lagrangian is identical with standard robot except for the flexible load. To compute its kinetic energy, the position and velocity along the flexible load is necessary w.r.t. \mathcal{W} :

$$p_f(x) = p_e + R_{\mathcal{L}}^{\mathcal{W}} \left(x \ w(x, t) \right)^T, \quad \dot{p}_f(x) = J_f(x) \dot{q} \quad (5.6)$$

where $J_f \in \mathbb{R}^{2 \times (n+m)}$ is the flexible load Jacobian attached on robot arm, $1_m \in \mathbb{R}^m$ is one vector, $e_2 = [0; 1] \in \mathbb{R}^2$ is the unit vector. Its corresponding kinetic energy is given as $T_{bar} = \frac{\rho A}{2} \int_0^{l_f} \dot{p}_f(x)^T \dot{p}_f(x) dx$.

Regarding the potential energy, the elastic energy is also different with standard robot dynamics $U_{bar,el} = \frac{EI}{2} \int_0^{l_b} \left(\frac{\partial^2 w}{\partial x^2} \right)^2 dx = \frac{EI}{2} \sum_{i=1}^m \sum_{j=1}^m d_{ij} \delta_i \delta_j$ where $d_{ij} := \int_0^{l_b} \phi_i'' \phi_j'' dx$ satisfies the orthogonality in (5.5).

Then, we can derive following Euler-Lagrange dynamics of the cooperative manipulation system with the RVM:

$$\begin{bmatrix} M_{\theta} & M_{\theta\delta} \\ M_{\delta\theta} & M_{\delta} \end{bmatrix} \ddot{q} + \begin{bmatrix} C_{\theta} & C_{\theta\delta} \\ C_{\delta\theta} & 0 \end{bmatrix} \dot{q} + g + \begin{bmatrix} 0 & 0 \\ 0 & K \end{bmatrix} q = B\tau \quad (5.7)$$

where $M_{\theta} \in \mathbb{R}^{n \times n}$, $M_{\delta} \in \mathbb{R}^{m \times m}$, $M_{\theta\delta} = M_{\delta\theta}^T \in \mathbb{R}^{n \times m}$ are the inertia matrix, $C_{\theta} \in \mathbb{R}^{n \times n}$, $C_{\delta\theta} \in \mathbb{R}^{m \times n}$, $C_{\theta\delta} \in \mathbb{R}^{n \times m}$ are the Coriolis matrix, $g \in \mathbb{R}^{n+m}$ is the gravity force vector, $B(q) \in \mathbb{R}^{(n+m) \times (n+2n_m)}$ is the input mapping matrix, $\tau = [\tau_a; \tau_m] \in \mathbb{R}^{n+m}$ is control input with the joint torque of manipulator $\tau_a \in \mathbb{R}^n$ and the module thrust input $\tau_m = [\lambda_1 R_{m,1} e_2; \dots; \lambda_{n_m} R_{m,n_m} e_2] \in \mathbb{R}^{n_m}$

\mathbb{R}^{2n_m} where $R_{m,i} \in SO(2)$ is the rotation matrix of i -th module, and $\lambda_{m,i} \in \mathbb{R}$ is the thrust magnitude. It is important to note that the inertia matrix for flexibility M_δ and the stiffness matrix K are constant diagonal matrix, even if multiple RVM in contrast to a single quadrotor in [44], where the off-diagonal terms are eliminated because $\dot{\delta}_i \dot{\delta}_j$ terms in the kinetic energy and $\delta_i \delta_j$ terms in the elastic energy meets the orthogonality properties (5.5). Note that the RVM is rigidly attached to the flexible load, thus its equation of motion is incorporated in the above dynamics. The input mapping matrix $B(q)$ have the following structure

$$B = \begin{bmatrix} I_n & B_{\theta m} \\ 0 & B_{\delta m} \end{bmatrix} \in \mathbb{R}^{(n+m) \times (n+2n_m)}$$

where $I_n \in \mathbb{R}^{n \times n}$ is the identity matrix, $B_{\theta m} = [J_{f\theta}^T(l_1) \cdots J_{f\theta}^T(l_{n_m})] \in \mathbb{R}^{n \times n_m}$ is the input mapping matrix from the module thrust to robot arm joints, $B_{\delta m} = [B_{\delta m,1} \cdots B_{\delta m,n_m}] \in \mathbb{R}^{m \times 2n_m}$ is the input matrix for the flexibility dynamics with

$$B_{\delta m,i} = \Phi(l_i)^T [-\sin \bar{\theta}_l, \cos \bar{\theta}_l] \quad (5.8)$$

where $\bar{\theta}_l = \sum \theta_i + \theta_l$ is the absolute orientation of the flexible load at the end-effector of the arm. Note that the manipulator control input τ_a cannot directly apply its torque to the flexible load dynamics while the RVM input τ_m directly control the flexible load along $B_{\delta m}$. Since the matrix $B_{\delta m,i}$ has rank one although each RVM can generate thrust in $E(2)$, the m -dof flexible load dynamics can be under-actuated when the number of the RVM is less than the number of the mode shape (i.e., $n_m < m$).

5.4 Controllability Analysis

The controller design is motivated by diagonal and constant dynamic structure of the flexible load in (5.7). Then, we divide the control framework into the following two sub-problems: 1) fully-actuated robot arm nominal trajectory tracking; 2) flexible load vibration suppression and gravity compensation via the distributed RVMs.

However, as shown in the structure of $B_{\delta m}$ in (5.8), depending on the relation between the number of the modules n_m and mode shapes m , given robotic system can be under-actuated to the vibration dynamics. Thus, we analyse the controllability condition, which is only handled for single quadrotor attached on the flexible load in [44], therefore, the theory should be extended to distributed RVMs. In addition, the terms in $B_{\delta m}$ is determined by location of the RVMs, thus we can expect that the distribution of RVMs affect to not only controllability but also the control performance.

5.4.1 Flexible Load Dynamics Linearization

The fully actuated robot arm control guarantees $\xi \rightarrow \xi^d$ where $\xi = (p_e, \theta_e) \in \mathbb{R}^3$ is end-effector pose. Therefore, the vibration dynamics can then be rewritten with ξ^d as follows

$$\begin{bmatrix} \ddot{\delta} \\ \dot{\delta} \end{bmatrix} = \begin{bmatrix} 0_m & -\bar{K} \\ I_m & 0_m \end{bmatrix} \begin{bmatrix} \dot{\delta} \\ \delta \end{bmatrix} + \begin{bmatrix} \bar{B}_{\delta m} \\ 0 \end{bmatrix} \tau_m - \begin{bmatrix} M_\delta^{-1} E \\ 0 \end{bmatrix} \quad (5.9)$$

where $\bar{K} := M_\delta^{-1}K$, $\bar{B}_{\delta m} := M_\delta^{-1}B_{\delta m}$ and E is defined as $E := M_{\delta\xi}\ddot{\xi}^d + C_{\delta\xi}\dot{\xi}^d + g_\delta(\bar{\theta}_e^d)$. We can further simplify the control input expression using the definition of $B_{\delta m}$ in (5.8) and τ_m as follows

$$\bar{B}_{\delta,m}\tau_m = \underbrace{M_\delta^{-1} [\Phi(l_1)^T \cos \theta_{t,1}^\mathcal{L} \cdots \Phi(l_{n_m})^T \cos \theta_{t,n_m}^\mathcal{L}]}_{=: b_{\delta m} \in \mathbb{R}^{m \times n_m}} \lambda_m$$

where $\theta_{t,i}^\mathcal{L} = \theta_{t,i} - \bar{\theta}_l$ is the relative thrust generation direction of i -th RVM w.r.t. the flexible load frame \mathcal{L} . Recall that θ_t can be independently controlled thanks to arbitrary thrust generation capability of RVM in $E(2)$ as stated in Sec. 5.2.

Depending on relation between n_m , m and placement of the RVM, the system can lose its controllability. Therefore, we design the flexible load vibration/deflection suppression controller based on controllability analysis. To analyse controllability, we linearize the dynamics (5.9) at the equilibrium deflection $\delta_e \in \mathbb{R}^m$ along the end-effector trajectory ξ^d .

We aim that the flexible load behaves similar to the rigid body, thus the control objective of the RVM includes both the vibration suppression (i.e., $\dot{\delta} = 0$) and the deflection compensation $w(l_f) = 0$. For this, we design a feedforward control input to compensate the gravity at the equilibrium deflection δ_e to satisfy $w(l_f) = 0$ as $\lambda_m = (\Phi K^{-1} b_{\delta m})^\dagger \Phi K^{-1} g_\delta(\bar{\theta}_e^d)$ where $(\cdot)^\dagger$ is Moore-Penrose pseudo inverse. Here, we choose λ_m solution that minimize overall energy consumption by minimizing in terms of thrust two-norm. Then, the corresponding equilibrium deflection shape mode vector satisfies $\delta_e = (-I + K^{-1} b_{\delta m} (\Phi K^{-1} b_{\delta m})^{-1} \Phi) K^{-1} g_\delta(\bar{\theta}_e^d)$. Note that the equilibrium deflection δ_e satisfies zero deflection at the load-tip, i.e., $w(l_f) = \Phi \delta_e = 0$.

Finally, we can linearize the dynamics (5.9) at the equilibrium deflection δ_e

$$\begin{bmatrix} \ddot{\tilde{\delta}} \\ \dot{\tilde{\delta}} \end{bmatrix} = \underbrace{\begin{bmatrix} 0_m & -\bar{K} \\ I_m & 0_m \end{bmatrix}}_{=:A} \begin{bmatrix} \ddot{\tilde{\delta}} \\ \dot{\tilde{\delta}} \end{bmatrix} + \underbrace{\begin{bmatrix} \bar{b}_{\delta m} \\ 0 \end{bmatrix}}_{=:B} \bar{\lambda}_m \quad (5.10)$$

where $\tilde{\delta} = \delta - \delta_e$ and $\bar{\lambda}_m = \lambda_m - (\Phi K^{-1} b_{\delta m})^\dagger \Phi K^{-1} g_\delta$.

5.4.2 Controllability

The linearized flexible load dynamics (5.10) is represented by $2m$ -dof configurations $[\dot{\tilde{\delta}}; \tilde{\delta}] \in \mathbb{R}^{2m}$ with n_m -dof RVM inputs via $B\lambda_m$. And the input mapping matrix B is a function of the module placement $\phi_i(l_j)$ and the thrust direction $\theta_{t,i}$. Therefore, we need to verify whether the input λ_m can suppress the vibration/deflection in the linearized system. For this, we utilize the controllability matrix $\mathcal{C} := [B \ AB \ \cdots \ A^{2m-1}B] \in \mathbb{R}^{2m \times 2mn_m}$ of the linearized dynamics (5.10) which is computed as follows

$$\mathcal{C} = I_2 \otimes \underbrace{\begin{bmatrix} \bar{b}_{\delta m} & -\bar{K} & \cdots & (-\bar{K})^{m-1} \bar{b}_{\delta m} \end{bmatrix}}_{=: \mathcal{C}_s \in \mathbb{R}^{m \times mn_m}} \quad (5.11)$$

where \otimes is Kronecker product. The linearized flexible load dynamics (5.10) is controllable, if the controllability matrix has full row rank. Since the left term of Kronecker product is identity matrix, to figure out the controllability condition, we need to check the full row rank condition of \mathcal{C}_s . However, the controllability matrix is not a square matrix for multiple RVM case, thus we cannot directly apply previous result by checking determinant (c.f., square

matrix $\mathcal{C}_s \in \mathbb{R}^{m \times m}$ in [44]). Since the full row rank condition for \mathcal{C}_s is equivalent to $\det(\mathcal{C}_s \mathcal{C}_s^T) > 0$, we first evaluate it.

Lemma 3. Consider the submatrix of the controllability matrix \mathcal{C}_s of the linearized system (5.10). Then the matrix \mathcal{C}_s satisfies following properties:

$$\mathcal{C}_s \mathcal{C}_s^T = \sum_{i=1}^{n_m} \text{diag}(\bar{b}_{i,1}, \dots, \bar{b}_{i,m}) \mathcal{K}_m \mathcal{K}_m^T \text{diag}(\bar{b}_{i,1}, \dots, \bar{b}_{i,m})$$

where $\mathcal{K}_m := [1_m, \bar{K}1_m, \dots, \bar{K}^{m-1}1_m]$ and $\bar{b}_{i,j}$ is (i, j) component of $\bar{b}_{\delta m}$; and

$$\det(\mathcal{C}_s \mathcal{C}_s^T) = \prod_{i=1}^m \left(\sum_{j=1}^{n_m} \bar{b}_{i,j}^2 \right) \cdot \prod_{\substack{k=2 \\ 1 \leq l < k}}^m w_{n,k-l}^2 + f(b_{\delta m}, \mathcal{K}_m) \quad (5.12)$$

where $w_{n,k-l} := w_{n,k} - w_{n,l}$ and $f(b_{\delta m}, \mathcal{K}_m)$ is residual function satisfying following inequality:

$$f(l, \theta_m) \geq - \prod_{i=1}^m \left(\sum_{j=1}^{n_m} \bar{b}_{i,j}^2 \right) \cdot \prod_{\substack{k=2 \\ 1 \leq l < k}}^m w_{n,k-l}^2$$

where \geq is replaced by $>$ only when $\prod_{i=1}^m \left(\sum_{j=1}^{n_m} \bar{b}_{i,j}^2 \right) \cdot \prod_{\substack{k=2 \\ 1 \leq l < k}}^m w_{n,k-l}^2 \neq 0$.

Proof: The first item is the result of straightforward calculation of the matrix multiplication. Regarding the second item, the given matrix $\mathcal{C}_s \mathcal{C}_s^T \in \mathbb{R}^{m \times m}$ is positive semi-definite symmetric matrix and it always satisfy following inequality from $x \mathcal{C}_s \mathcal{C}_s^T x \geq 0, \forall x \in \mathbb{R}^m : |x| = 1$ which is equivalent to $\det(\mathcal{C}_s \mathcal{C}_s^T) \geq 0$.

From the Leibniz formula of the matrix determinant, the determinant of $\mathcal{C}_s \mathcal{C}_s^T$ can be written as

$$\det(\mathcal{C}_s \mathcal{C}_s^T) = \sum_{\sigma \in S_n} \text{sgn}(\sigma) \prod_i^n \left(\left(\sum_{j=1}^{n_m} \bar{b}_{i,j} \bar{b}_{\sigma_i,j} \right) \mathcal{K}_{m,1} \mathcal{K}_{m,\sigma_i}^T \right) \pm \prod_{i=1}^m \left(\sum_{j=1}^{n_m} \bar{b}_{i,j}^2 \right) \sum_{\sigma \in S_n} \text{sgn}(\sigma) \prod_i^n (\mathcal{K}_{m,1} \mathcal{K}_{m,\sigma_i}^T) \quad (5.13)$$

where $\text{sgn}(\cdot)$ is the sign function of permutations in the permutation group S_n which returns 1 or -1 for even and odd permutations respectively. We employ the result of Theorem 1 in [44] for $\det(\mathcal{K}_n)$ in second line equation which is similar to well-known Vandermonde matrix structure whose determinant is given by

$$\begin{aligned} \det(\mathcal{K}_m \mathcal{K}_m^T) &= \sum_{\sigma \in S_n} \text{sgn}(\sigma) \prod_i^n (\mathcal{K}_{m,1} \mathcal{K}_{m,\sigma_i}^T) \\ &= \det(\mathcal{K}_m)^2 = \prod_{\substack{k=2 \\ 1 \leq l < k}}^m w_{n,k-l}^2 \end{aligned} \quad (5.14)$$

Since this determinant is larger than zero and the term $(\sum_{j=1}^{n_m} \bar{b}_{i,j}^2) \geq 0$, the resultant product term in (5.12) and (5.13) should be larger than zero. This (5.14) explain the first term in (5.12) and the second line is equivalent with (5.13).

Other terms stand for the residual function $f(b_{\delta m}, \mathcal{K}_m)$. Regarding the residual function, if $\sum_{j=1}^{n_m} \bar{b}_{i,j}^2 \neq 0, \forall i = 1, \dots, m$, then there exists i that satisfies $\text{diag}(\bar{b}_{i,1} \dots, \bar{b}_{i,m})x \neq 0, \forall x \in \mathfrak{R}^m : |x| = 1$. On the other hand, if

$w_{n,i} \neq w_{n,j}, \forall i, j = 1, \dots, m : i \neq j$, $\mathcal{K}_n \mathcal{K}_n^T$ is positive definite from its determinant expression in (5.14). If $\sum_{j=1}^{n_m} \bar{b}_{i,j}^2 = 0$ or $w_{n,k} = w_{n,l}$ for some i, j, l , then the inequality automatically hold due to semi-positive definite matrix $\mathcal{C}_s \mathcal{C}_s^T$. ■

From Lemma 3, the three sufficient conditions to ensure controllability of the linearized system can be extracted in the following theorem:

Theorem 4. Consider the linearized flexible load dynamics (5.10) and controllability matrix \mathcal{C} . Then, if the following three conditions are met, the linearized flexible load dynamics is controllable:

- 1) **Placing condition** $\sum_{j=1}^{n_m} \phi_i(l_j)^2 \neq 0, \forall i = 1, \dots, m$;
- 2) **Tilting condition** $\cos(\theta_{t,i}^{\mathcal{L}}) \neq 0$ or $\theta_{t,i}^{\mathcal{L}} \neq \frac{\pi}{2} + k\pi, k \in \mathcal{Z}$
- 3) **Mode independency condition** $w_{n,i} \neq w_{n,j}$.

Proof: According to Lemma 3, $\det(\mathcal{C}_s \mathcal{C}_s^T) > 0$ if $(\sum_{j=1}^{n_m} \bar{b}_{i,j}^2) \neq 0, \forall i = 1, \dots, m$ and $w_{n,k-l}^2 \neq 0, \forall k, l = 1, \dots, m$ and $k \neq l$. Therefore, the flexible load dynamics (5.10) is controllable when the placing, tilting and mode independency conditions meet. ■

To satisfy the placing condition, at least one of the mode shape at the RVM location should not be zero for each vibration mode, i.e., $\sum_{j=1}^{n_m} \phi_i(l_j)^2 \neq 0, \forall i = 1, \dots, m$. This controllability condition enforces a design criteria for attaching the RVM to avoid the node position, i.e., $\phi_i(x) = 0$. Unlike a single

quadrotor case in previous result [44], even though one of the RVM is located at the node position of i -th mode, the whole system is controllable as long as there exists a RVM that is not located in node position of i -th mode.

If the RVM cannot meet the tilting condition, i.e., $\cos(\theta_{t,i}^{\mathcal{L}}) = 0$, then the thrust of the RVM is aligned to x -axis of the load frame \mathcal{L} and subsequently cannot exert force along the deflection direction. This controllability condition imposes to control the thrust direction to $\cos(\theta_{t,i}^{\mathcal{L}}) \neq 0$. This condition can always be preserved since the RVM is designed to instantly generate arbitrary direction thrust in the plane. On the other hand, If we use a quadrotor as shown in [44], the quadrotor attitude should be controlled to generate desired thrust direction.

Theorem 4 suggests sufficient conditions for the controllable system. The exact necessary and sufficient condition for controllability can elucidate when the system become uncontrollable, however, those exact conditions does not meet the practicality. For example, even though two vibration modes have same natural frequency against the physical condition, the system can be controllable with certain condition. However, the physical condition cannot be violated theoretically. Therefore, in practice, the sufficient conditions are enough to ensure controllability.

5.5 Optimal placement

5.5.1 Optimal Placement of Actuator

In the previous section, the controllability is affected by how the RVMs are distributed along the flexible load. However, the controllability analysis does not explain how well the RVMs can suppress the vibration and what is the optimal RVM placement. For this, we adopt controllability gramian approach whose definition is given by $W_c = \int_0^\infty e^{A\tau} B B^T e^{A^T \tau} d\tau$. An asymptotically stable system should have unique bounded solution with integration along infinite time horizon. Since the linearized vibration dynamics is spring-mass system, we add the damping term to (5.10). This assumption is valid, because the real system always suppress the vibration with its own small damping as time goes by. The coefficient is verified to have small value $D \approx 0$, thus we add the diagonal damping term D similar to diagonal K , however, note that it can be neglected by assuming it to zero as we utilize in previous section.

Here, we transform the linearized dynamics (5.10) into equivalent state space representation to simplify controllability analysis as $\dot{x} = \hat{A}x + \hat{B}\lambda_m$ where $x = [\dot{\delta}_1; w_{n,1}\delta_1; \dots, \dot{\delta}_m; w_{n,m}\delta_m] \in \mathbb{R}^{2m}$ is transformed state and the matrix \hat{A} and \hat{B} satisfy corresponding transformation. Then, the controllability gramian solution is given in the following theorem

Theorem 5. Consider the linearized flexible load dynamics $\dot{x} = \hat{A}x + \hat{B}\lambda_m$. Suppose the damping ratio satisfy $\zeta_i \ll w_{n,i}$ and $\zeta_i \approx 0, \forall i = 1, \dots, m$. Then,

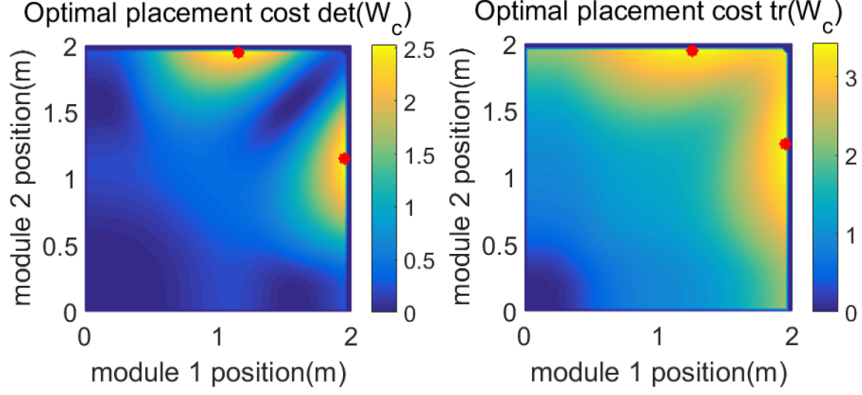


FIGURE 5.6: Optimal placement of two RVMs on aluminum bar. $\det(W_c)$ provides $(l_1, l_2) = (1.15m, 1.95m)$ (left). $\text{tr}(W_c)$ provides $(l_1, l_2) = (1.25m, 1.95m)$ (right).

the controllability gramian is derived s.t.,

$$W_c \approx \text{diag}(W_{11}, \dots, W_{mm}) \quad (5.15)$$

where $W_{ii} = \text{diag}\left(\frac{\beta_{ii}}{4\zeta_i w_{n,i}}, \frac{\beta_{ii}}{4\zeta_i w_{n,i}}\right)$ and $\beta_{ij} = \sum_{k=1}^{n_m} \bar{b}_{i,k} \bar{b}_{j,k}$.

Proof: Using transformed linearized dynamics, the controllability gramian can be solved by Sylvester equation similar to [69] and its block matrix is

$$W_{ij} = \frac{\beta_{ij}}{d_{ij}} \begin{bmatrix} a_{ij}(\zeta_i w_{n,j} + \zeta_j w_{n,i}) & w_{n,j} c_{ji} \\ -w_{n,i} c_{ji} & a_{ij}(\zeta_i w_{n,i} + \zeta_j w_{n,j}) \end{bmatrix}$$

with $d_{ij} = 4w_{n,i}w_{n,j}(\zeta_i w_{n,i} + \zeta_j w_{n,j})(\zeta_i w_{n,j} + \zeta_j w_{n,i}) + (w_{n,i}^2 - w_{n,j}^2)^2$, $a_{ij} = 2w_{n,i}w_{n,j}$ and $c_{ji} = (w_{n,j}^2 - w_{n,i}^2)$.

From the assumption $\zeta_i \ll w_{n,i}$ and $\zeta_i \approx 0$, $d_{ij} \approx (w_{n,i} - w_{n,j})^2$ for $i \neq j$ and $d_{ii} = 16w_{n,i}^3\zeta_i^2$ for $i = j$. Then, the off-diagonal block matrices are not depend

on $1/\zeta$, however, the diagonal block matrices depend on $1/\zeta$. Therefore, the components in the off-diagonal matrices are approximated to zero since those are relatively smaller than the diagonal matrices in (5.15). ■

Controllability gramian W_c characterizes the minimal energy required to steer the state from zero to certain state (i.e., $x^T W_c^{-1} x$) [70]. From this property, different quantitative measures of controllability considered in literature [71]. The trace of W_c related to the average control energy over random target states, however this metric cannot show how effectively it can suppress all the vibration, because only slow vibration modes are dominant. On the other hand, the determinant of W_c represents the volume of the ellipsoid containing the states that can be reached with an unit-energy, thus $\max \text{tr}(W_c)$ represents the effectiveness of vibration suppression to every vibration modes. Here, we choose the controllability metric as $\det(W_c)$ to effectively suppress the vibrations which is given in Fig. 5.6 for experimental setup in Sec. 5.6. These metrics are represented by the singular values of W_c and directly computed by $\frac{\beta_{ii}}{4\zeta_i w_{n,i}}$ according to Theorem 5.

Theorem 5 gives an intuition that the location where it maximizes mode deflection or its summation is the optimal placement which is compatible with Theorem 4 that shows the node positions can makes system uncontrollable. And the controllability conditions are also compatible with the structure of W_c in Theorem 5. In Theorem 5, the determinant of W_c is represented by the multiplication of the diagonal terms. The diagonal terms become zero when $\beta_{ii} = 0$ which is also shown in Lemma 3, thus W_c cannot be singular as long as placing and tilting condition hold.

5.5.2 Optimal Placement of Module

In Sec. 5.5.1, the analysis about the optimal placement of actuators shows that the maximization of deflection, deflection angle and strain or its summation give an optimal placement for actuators and sensors while its node position give loss of the controllability or the observability. Even though these analysis give an intuition of the optimal placement of each case, however, it still cannot provide optimal placement of the RVM equipped with both actuator and sensor.

Here, the deflection of the flexible load can be measured by an external measurement such as MoCap, however, we aim to realize onboard estimation of the deflection through the sensor equipped with RVM rather than rely on external measurement. For this, we need to verify whether the deflection of the load can be estimated by sensors. The sensors equipped with RVM can be formulated by following output relation

$$\underbrace{\begin{bmatrix} y_a \end{bmatrix}}_{=: y \in \mathbb{R}^{n_m}} = \underbrace{\begin{bmatrix} 0_m & C_{a\delta} \end{bmatrix}}_{=: C \in \mathbb{R}^{2n_m \times 2m}} \begin{bmatrix} \dot{\tilde{\delta}} \\ \tilde{\delta} \end{bmatrix} \quad (5.16)$$

where $y_a \in \mathbb{R}^{n_m}$ is output variable represents angle measurement from IMU, $C_{a\delta} = [\Phi'(l_1); \dots; \Phi'(l_{n_m})] \in \mathbb{R}^{n_m \times m}$ is output matrix for y_a .

Therefore, we need to formulate an optimal placement of RVM to maximize both control capability for vibration suppression via rotors of RVMs and sensing capability for deflection via sensor equipped on RVM. However, the optimal placement for actuation and sensor are not identical, thus, we need to

quantify both capabilities as an unified cost function to deal with these conflict conditions. For this, we adopt a LQG (Linear Quadratic Gaussian) formulation to give a quantitative value at a given RVMs placement. To adopt the LQG formulation, we first derive a linearized flexible load vibration dynamics driven by additive white Gaussian noise:

$$\dot{x} = Ax + B_u u + B_v v_x \quad (5.17)$$

$$y = C_y x + D_y v_y \quad (5.18)$$

where $v_x \in \mathbb{R}^{2m}$ and $v_y \in \mathbb{R}^{2n_m}$ are the uncertainty of the system dynamics and output model whose covariance matrices are $V_x := E[v_x v_x^T] \in \mathbb{R}^{2m \times 2m}$ and $V_y := E[v_y v_y^T] \in \mathbb{R}^{2n_m \times 2n_m}$. This linear system is originally derived in (5.10), however, since the LQG formulation allows to handle uncertainties on the dynamics model and measurement model, the additive white Gaussian noise is additionally introduced compared to (5.10) and (5.16). The uncertainty in linearized dynamics v_x includes modeling error, uncertainty from rotor thrust dynamics and inertial parameters, etc. For the output model, the uncertainty v_y mainly comes from the uncertainty of sensor and modeling error of between deflection and measurement. The LQG formulation have an advantage that can handle uncertainties in models while the controllability and observability gramian in Sec. 5.5.1 can handle deterministic system.

To quantify the given RVMs placement based on (5.17), we utilize infinite horizon LQG (Linear Quadratic Gaussian) formulation since this formulation provides a cost regardless of the initial and final state, thus it is suitable to evaluate the control and sensing capability. Then, the cost function is given as

follows

$$J := \min_{\lim t \rightarrow \infty} E [x(t)^T Q x(t) + u(t)^T R u(t)]$$

where $E(\cdot)$ is expectation of probabilistic variable, $Q \in \Re^{2m \times 2m}$ and $R \in \Re^{n_m \times n_m}$ are the weight matrices which are assumed to be diagonal matrix in here. Here, we can apply infinite horizon LQG problem since the flexible load dynamics is formulated by a linear time-invariant system. The cost function represents the optimal performance of control and state estimation with given RVMs distribution.

According to LQG theory, the separation principle of linear system with additive noise provides the solution of this minimization problem that can be equivalently represented by following equation:

$$J = \text{trace} [Q^{\frac{1}{2}} Y^* (Q^{\frac{1}{2}})^T] + \text{trace} [\bar{B}^T X \bar{B}]$$

where $\bar{B} := Y^* C_y^T (D_y V_y D_y^T)^{-\frac{1}{2}}$, and $X \in \Re^{n \times n}$, $Y \in \Re^{n \times n}$ are the solution of following two algebraic Riccati equations

$$\begin{aligned} A^T X^* + X^* A - X^* B_u (R)^{-1} B_u^T X^* + Q &= 0 \\ A Y^* + Y^* A^T - Y^* C^T (D_y V_y D_y^T)^{-1} C Y^* + B_v V_x B_v^T &= 0. \end{aligned}$$

Each Riccati equation represents the algebraic Riccati equation for infinite horizon LQR (Linear Quadratic Regulator) and steady state Kalman filter. Thus, it can be interpreted that the optimal solution is given by the separated formulation of optimal controller and optimal estimator with given RVMs

distribution.

At every RVM placement, the LQG problem gives both optimal controller and optimal estimator with corresponding cost function value J . If we define a given RVMs placement set $\mathcal{P} := \{l_1, \dots, l_{n_m}\}$, then the optimal cost and its corresponding LQR and Kalman filter gain can be calculated. The optimal placement formulation can be summarized into following minimization problem:

$$\mathcal{P}^* = \arg \min_{\mathcal{P}} J(\mathcal{P}) \quad (5.19)$$

where $\mathcal{P}^* = \{l_1^*, \dots, l_{n_m}^*\}$ is the set of optimal placement. Here, this LQG formulation concerns about the placement of RVMs only, thus, even though the thrust direction $R_{m,i}e_2$ also affect to control capability, we assume the direction is fixed with unit vector e_y .

Note that the controllability gramian and the LQG formulation is equivalent when the output model is deterministic, i.e., $v_y = 0$ and the cost function only includes weight on input, i.e., $Q = 0$. Due to the duality between the controllability and the observability, the observability gramian is also equivalent with LQG when the control input is zero and the model propagation noise $v_x = 0$. Since LQG be computed with various weight matrix Q, R , it can manage the system with different properties and purposes using various weight matrix such as maximizing control performance, minimizing control effort.

It is also noticeable that the proposed optimal placement can be extended with various robust controller including H_2 , H_∞ controller by replacing the

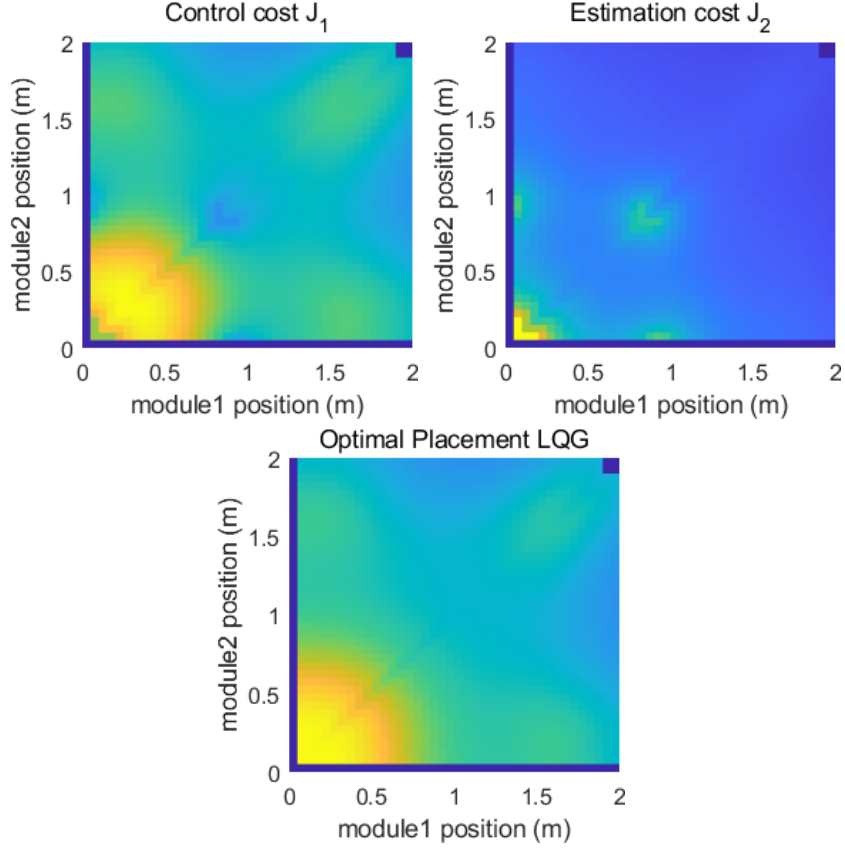


FIGURE 5.7: Optimal placement of two RVMs on aluminum bar. Left top plot represents control cost J_1 and right top plot represents estimation cost J_2 . Bottom plot shows resultant LQG cost.

cost function of (5.19). The cost function can be any function that can quantify the capability of control and sensing.

The optimal placement is determined by material property, i.e., density, Young's modulus, cross section area, etc, and the relative inertia between the flexible load and the RVM and number of RMVs on the flexible load. However, since the RVM is rigidly attached on the flexible load during the task, the optimal placement is calculated off-line and it is provided as a lookup table.

5.5.3 Control Design

Here, we utilize LQR to optimally suppress vibration along with the gravity compensation for the RVM. And we utilize computed torque control for the robot arm. This control is same with the approach introduced in previous result. For more detail, please refer [44].

5.6 Experiment

We implement two RVMs attached on 2m long aluminium bar at optimal place in Fig. 5.6 with cross section $40mm \times 3mm$ as shown in Fig. 5.8. Each RVM is constructed based on optimal design in Sec. 5.2 and equipped with Pixhawk for computing, wireless communication between ground PC and ESCs control. MoCap is used to measure the position and orientation of each RVM and load-tip deflection. Power supply unit is used to supply power to the RVMs, however, each module can also be operated using onboard battery.

Three experimental verifications are performed for this two RVM system: 1) stationary robot arm with external disturbances and 2) one end position manipulated by robot arm. These two experiments are compared to the same scenarios without RVMs; and 3) one end pose manipulated by human operator. In the first experiment, an operator exerts external disturbances every 3 to 5 seconds at various location on the aluminium bar. On the other hand, the disturbances are exerted every 9 to 10 seconds for the experiment without RVMs because the vibration persists for a long time. It takes about 1 min to totally suppress the vibration with its structural damping. The plot in Fig.

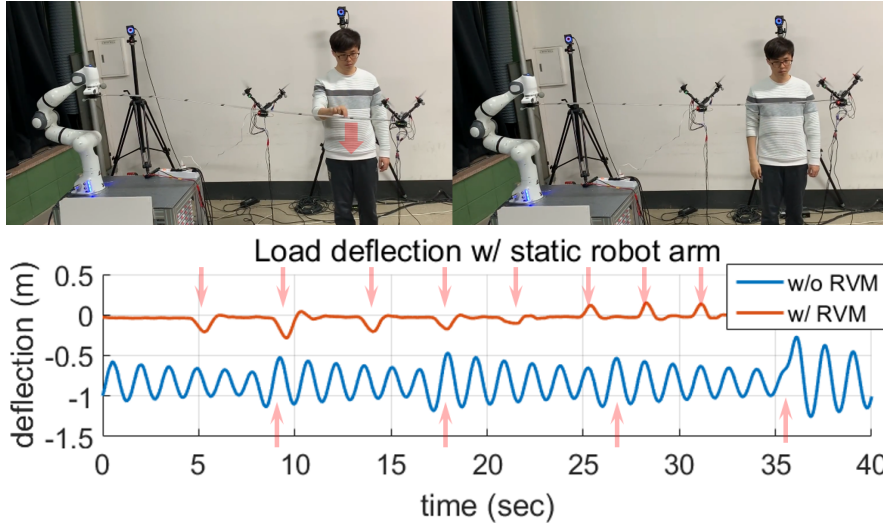


FIGURE 5.8: Snapshots and load-tip deflection plot for stationary robot arm under external disturbances. Red arrows represent times external forces exerted.

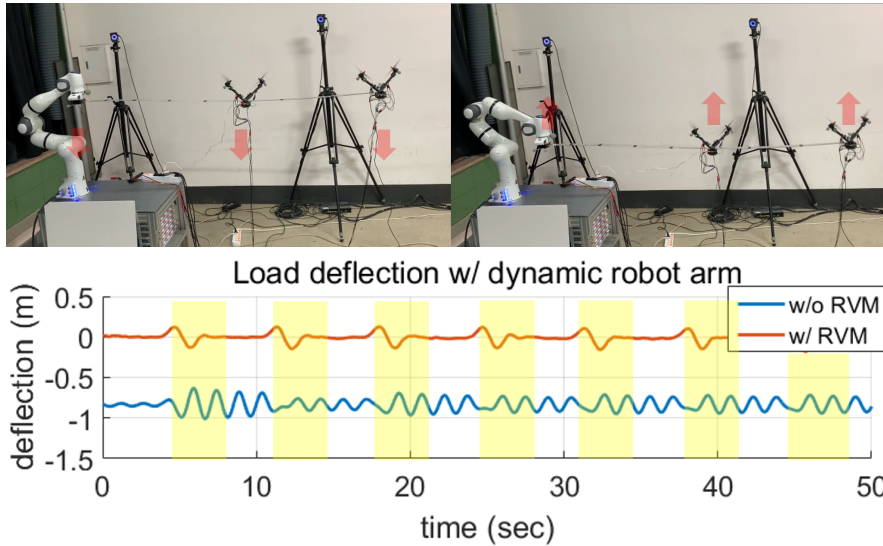


FIGURE 5.9: Snapshots and load-tip deflection plot for one-end position manipulated by robot arm. Yellow shaded columns represent times the robot arm moves.



FIGURE 5.10: Snapshots for vibration suppression of flexible load using distributed RVMs with pose manipulated by human operator.

5.8 shows that RVMs effectively suppress the vibration before it reaches next peak of sinusoidal deflection.

In the second experiment, the external disturbance is replaced by the motion of robotic arm. To see the vibration suppression performance, the RVM input does not have feedforward input of the robot arm. The robot motion includes both upward and downward motion and this motion induces vibration. In Fig. 5.9, the plot shows that the RVM can suppress the vibration right after the motion stops. In contrast, without RVM, the plot shows that even though its amplitude is amplified or reduced depending on direction of robot arm motion and vibration, the vibration is not suppressed during the bar is manipulated. The last experiment shows that the distributed RVMs system can also be applied to non-stationary robot systems or even cooperative tasks with humans.

Three experiments also show that the gravity induced deflection of the aluminium bar is compensated by the RVMs so that the vibration shifted from -0.8m to 0m .

5.7 Conclusion

In this chapter, we propose a novel RVM to manipulate and transport a large flexible object. The number of modules can be varied to adapt the various object since the RVM can be easily attachable/detachable. The RVM is optimally designed to maximize the feasible thrust generation area along the plane that vibration occurs with the minimum number of rotors while it minimizes undesirable torque. We derive the full dynamics of the distributed RVMs and elucidate the controllability condition. Furthermore, we also propose the optimal placement of the RVMs on the flexible load based on the controllability gramian. Experimental validation of the distributed RVMs is also presented.

Chapter 6

Conclusion and Future Work

6.1 Conclusion

This thesis addresses the dynamics and control problems of novel aerial manipulation system based on rotor based actuation. The aerial manipulation system includes: 1) quadrotor manipulator system; and 2) novel rotor-based vibration module.

For the first part, we reveal a certain underlying structure of the nonlinear Lagrange dynamics of the quadrotor-manipulator (QM) system, that is, its dynamics, although often overwhelmingly complex, can be completely split into: 1) the quadrotor-like center-of-mass dynamics in $E(3)$ with all under-actuation and gravity effect; and 2) the “internal” dynamics of quadrotor’s rotation and the manipulator configuration in the form of standard Lagrange dynamics with full actuation and no gravity effect. Relying on this structure, we propose a backstepping-like end-effector trajectory tracking control law, which allows for different control authority for each of these systems according to task objectives by exploiting the redundancy inherent in the system. Simulation using a

planar quadrotor with a 2-DOF arm for trajectory tracking and force control is also performed to verify the proposed theoretical framework.

Based on a result of single QM system, we also propose the cooperative control framework for multiple QM systems which consist of following hierarchical structure: 1) object behavior design; 2) optimal cooperative force distribution; and 3) individual QM system control. The proposed control framework can be adapted to variable tasks which need different behavior by changing a specific control block rather than redesign the whole controller. And also, different types of individual QM system controllers are also applicable to this control framework without variation of the hierarchical structure. We extend the result about the QM system position controller from decoupled dynamics structure to admittance-like force control. Moreover, we propose how to control the individual QM system, using the decoupled dynamics, depending on different dynamics characteristics of the (under-actuated/slower/coarse) quadrotor platform and the (fully-actuated/faster/fine) manipulator. Simulation results of cooperative object transport and compliant interaction are presented.

For the second part, we extend results on the MAGMaS, a novel cooperative heterogeneous manipulation system [36], to the case of flexible load manipulation. In particular, we derive the dynamical model of a planar MAGMaS, including vibrations in the long slender load. We then propose a control strategy for both trajectory tracking and effective vibration cancellation by exploiting the dynamical properties of such an under-actuated system for vibration, in particular vibration cancellation is achieved through a linearization scheme. Along the way, the conditions for controllability of the vibrations modes are exhibited. The validity of this approach is demonstrated in two simulations by

comparing its performance to the one of previously proposed approaches. The possible next step for this work are the experimental validation for the planar case, the system for which is already in construction, and the extension of the theoretical work to the general 3-dim case with multiple aerial robots. We then propose a novel RVM to manipulate and transport a large flexible object. The number of modules can be varied to adapt the various object since the RVM can be easily attachable/detachable. The RVM is optimally designed to maximize the feasible thrust generation area along the plane that vibration occurs with the minimum number of rotors while it minimizes undesirable torque. We derive the full dynamics of the distributed RVMs and elucidate the controllability condition. Furthermore, we also propose the optimal placement of the RVMs on the flexible load based on the controllability gramian. Experimental validation of the distributed RVMs is also presented. Some possible future research topics include: 1) sensor fusion with onboard sensor; 2) MoCap-less operation of distributed RVMs.

6.2 Future Work

We believe that the dynamics formulation and the control framework presented in this thesis will provide a general framework for other aerial manipulation systems with large DOF or systems with flexible components. The proposed dynamics formulation and control framework is not limited to the drone-manipulator system, thus it can be applied to large-DOF articulated robotic systems such as mobile manipulator, ROV, space robot, and a humanoid robot. The design framework also can be utilized to design other novel

aerial robots or the robotic system to optimally allocate the actuator with the minimum number. In addition, the analysis and the optimal placement of the actuator/sensor also can be employed in other robotic systems include flexible and soft components.

The dynamics formulation can be applied to not only the drone-manipulator system but also the general vehicle-manipulator system and this vehicle-manipulator system includes a humanoid robot. Differential geometric interpretation of the decomposition might provide a connection to other dynamics formulation and the fundamental properties to have these decoupled properties. From this decoupled dynamics structure, the complex control design problem can be simplified into a simple control design problem of two decoupled dynamics. Here, we provide the backstepping-based controller with dynamic properties of each decoupled dynamics, however, other control frameworks can be employed with the proposed dynamic structure while incorporating the properties of a given vehicle-manipulator system.

The control framework proposed for the drone-manipulator system is validated via simulation results in this thesis. The real implementation has many practical issues such as the development of precise and light-weight robotic arm, difficulties of torque control for lightweight robotic arm due to high gear ratio of the motor, force-torque control with under-actuation, etc. Thus, the real implementation and its practical problem might be a possible direction of this thesis.

For long and slender objects, the flexibility of the objects plays an important

role in the manipulation and transport of the payload. Furthermore, the flexibility of the link or joint of the aerial manipulation system and robotic systems that interact with the environment also plays an important role to ensure safe interaction without precise control, estimation under external disturbances. Thus, the controllability and observability also can be extended to more general robotic systems with multiple flexible links, joints, or even soft robots. In addition, unlike the rigid link and joint, the flexible and soft component in the robotic system can degrade control and estimation performance. Thus, it is important to determine and analyze how and where to place the actuator and sensor along with the robot. And the performance of the overall system can be affected by which sensor and actuator are employed. Therefore, the framework and analysis presented in this thesis might be extended and provide direction for starting analysis for those problems of flexible components and actuator/sensor allocation.

Bibliography

- [1] E. Frazzoli, M. A. Dahleh, and E. Feron. Trajectory tracking control design for autonomous helicopters using a backstepping algorithm. In *Proc. American Control Conference*, pages 4102–4107, 2000.
- [2] R. Mahony and T. Hamel. Robust trajectory tracking for a scale model autonomous helicopter. *International Journal of Robust and Nonlinear Control*, 14:1035–1059, 2004.
- [3] M-D Hua, T. Hamel, P. Morin, and C. Samson. A control approach for thrust-propelled underactuated vehicles and its application to vtol drones. *IEEE Transactions on Automatic Control*, 54(8):1837–1853, 2009.
- [4] O. Purwin and R. D’Andrea. Performing aggressive maneuvers using iterative learning control. In *Proc. IEEE Int’l Conference on Robotics and Automation*, pages 1731–1736, 2009.
- [5] D. J. Lee. Distributed backstepping control of multiple thrust-propelled vehicles on balanced graph. *Automatica*, 48(11):2971–2977, 2013.
- [6] D. J. Lee, C. Ha, and Z. Zuo. Backstepping control of quadrotor-type uavs: trajectory tracking and teleoperation over the internet. In *Proc. Int’l Conference on Autonomous Systems*, pages 217–225, 2013.

- [7] R. Mahony, V. Kumar, and P. Corke. Multirotor Aerial Vehicles: Modeling, Estimation, and Control of Quadrotor. *IEEE Robotics & Automation Magazine*, 19(3):20–32, 2012.
- [8] C. Ha, Z. Zuo, F. B. Choi, and D. J. Lee. Passivity-based adaptive backstepping control of quadrotor-type uavs. *Robotics and Automation Systems*, 62(9):1305–1315, 2014.
- [9] A. Franchi, C. Secchi, M. Ryll, H. H. Bühlhoff, and P. Robuffo Giordano. Shared control: Balancing autonomy and human assistance with a group of quadrotor UAVs. *IEEE Robotics & Automation Magazine*, 19(3):57–68, 2012.
- [10] D. J. Lee, A. Franchi, H. I. Son, C. Ha, H. H. Bulthoff, and P. R. Giordano. Semiautonomous haptic teleoperation control architecture of multiple unmanned aerial vehicles. *IEEE Transactions on Mechatronics*, 18(4):1334–1345, 2014.
- [11] DJI. www.dji.com/, Accessed: 2018-03-02.
- [12] Intel Shooting Star. <https://www.intel.com/content/www/us/en/technology-innovation/aerial-technology-light-show.html>, Accessed: 2018-03-02.
- [13] H.-N. Nguyen, S. Par, J. Park, and D. J. Lee. A novel robotic platform for aerial manipulation using quadrotors as rotating thrust generators. *IEEE Transactions on Robotics*, 34(2):353–369, 2018.
- [14] K. Kondak, F. Hubert, M. Schwarzbach, M. Laiacker, D. Sommer, M. Bejar, and A. Ollero. Aerial manipulation robot composed of an autonomous

- helicopter and a 7 degrees of freedom industrial manipulator. In *Proc. IEEE Int'l Conference on Robotics and Automation*, pages 2108–2112, 2014.
- [15] C. Korpela, M. Orsag, M. Pekala, and P. Oh. Dynamic stability of a mobile manipulating unmanned aerial vehicle. In *Proc. IEEE Int'l Conference on Robotics and Automation*, pages 4922–4927, 2012.
- [16] M. Tognon, B. Yuksel, G. Buondonno, and A. Franchi. Dynamic decentralized control for protocentric aerial manipulators. In *Proc. IEEE Int'l Conference on Robotics and Automation*, pages 6375–6380, 2017.
- [17] G. Darivianakis, Kostas Alexis, Michael Burri, and R. Siegwart. Hybrid predictive control for aerial robotic physical interaction towards inspection operation. In *Proc. IEEE Int'l Conference on Robotics and Automation*, pages 53–58, 2014.
- [18] Q. Lindsey, D. Mellinger, and V. Kumar. Construction of cubic structures with quadrotor teams. In *Robotics: Science and Systems*, 2011.
- [19] Koushil Sreenath, Nathan Michael, and Vijay Kumar. Trajectory generation and control of a quadrotor with a cable-suspended load-A differentially-flat hybrid system. In *Proc. IEEE Int'l Conference on Robotics and Automation*, pages 4888–4895, 2013.
- [20] H. Yang and D. J. Lee. Hierarchical Cooperative Control Framework of Multiple Quadrotor-Manipulator Systems. In *Proc. IEEE Int'l Conference on Robotics and Automation*, pages 4656–4662, 2015.

- [21] M. Mohammadi, A. Franchi, D. Barcelli, and D. Prattichizzo. Cooperative aerial tele-manipulation with haptic feedback. In *Proc. IEEE/RSJ Int'l Conference on Intelligent Robots and Systems*, pages 5092–5098, 2016.
- [22] N. Michael, J. Fink, and V. Kumar. Cooperative manipulation and transportation with aerial robots. *Autonomous Robots*, 30(11):73–86, 2011.
- [23] I. Palunko, R. Fierro, and P. Cruz. Trajectory generation for swing-free maneuver of a quadrotor with suspended payload: a dynamic programming approach. In *Proc. IEEE Int'l Conference on Robotics and Automation*, pages 2691–2697, 2012.
- [24] V. Ghadiok, J. Goldin, and W. Ren. Autonomous indoor aerial gripping using a quadrotor. In *Proc. IEEE/RSJ Int'l Conference on Intelligent Robots and Systems*, pages 4645–4651, 2011.
- [25] A. M. Dollar P. E. I. Punds, D. R. Bersak. Grasping from the air: hovering capture and load stability. In *Proc. IEEE Int'l Conference on Robotics and Automation*, pages 2491–2498, 2011.
- [26] C. E. Doyle, J. J. Bird, T. A. Isom, J.C. Kalmman, D. F. Bareiss, D. J. Dunlop, R. J. King, J. J. Abbott, and M. A. Minor. An avian-inspired passive mechanism for quadrotor perching. *IEEE/ASME Transactions on Mechatronics*, 18(2):506–517, 2013.
- [27] D. J. Lee and C. Ha. Mechanics and control of quadrotors for tool operation. In *Proc. ASME Dynamics Systems and Control Conference*, pages 177–184, 2012.

- [28] H. N. Nyugen and D. J. Lee. Hybrid force/motion control and internal dynamics of quadrotors for tool operation. In *Proc. IEEE/RSJ Int'l Conference on Intelligent Robots and Systems*, pages 3458–3464, 2013.
- [29] A.E. Jimenez-Cano, J. Martin, G. HereDia, and R. Cano A. Ollero. Control of an aerial robot with multi-link arm for assembly tasks. In *Proc. IEEE Int'l Conference on Robotics and Automation*, pages 4901–4906, 2013.
- [30] C. Korpela, M. Orsag, and P. Oh M. Pekala. Dynamic stability of a mobile manipulating unmanned aerial vehicle. In *Proc. IEEE Int'l Conference on Robotics and Automation*, pages 4907–4912, 2013.
- [31] V. Lippiello and F. Ruggiero. Exploiting redundancy in cartesian impedance control of uavs equipped with a robotic arm. In *Proc. IEEE/RSJ Int'l Conference on Intelligent Robots and Systems*, pages 3768–3773, 2012.
- [32] X. Ding and Y. Yu. Motion planning and stabilization control of a multipropeller multifunction aerial robot. *IEEE/ASME Transactions on Mechatronics*, 18(2):645–656, 2013.
- [33] K. Kondak, K. Krieger, A. Albu-Schaeffer, M. Schwarzbach, M. Laiacker, I. Maza, A. Rodriguez-Castano, and A. Ollero. Closed-loop behavior of an autonomous helicopter equipped with a rootic arm for aerial manipulation tasks. *International Journal of Advanced Robotic Systems*, 10(145):1–9, 2013.

- [34] S. Park, J. Lee, J. Ahn, M. Kim, J. Her, G-H. Yang, and D. J. Lee. Odar: Aerial manipulation platform enabling omni-directional wrench generation. *IEEE/ASME Transactions on Mechatronic*, 23(4):1907–1918, 2018.
- [35] H. Yang, S. Park, J. Lee, J. Ahn, D. Son, and D. J. Lee. Lasdra: Large-size aerial skeleton system with distributed rotor actuation. In *Proc. IEEE Int’l Conference on Robotics and Automation*, pages 7017–7023, 2018.
- [36] N. Staub, M. Mohammadi, D. Bicego, D. Prattichizzo, and A. Franchi. Towards robotic MAGMaS: Multiple aerial-ground manipulator systems. In *Proc. IEEE Int’l Conference on Robotics and Automation*, pages 1307–1312, 2017.
- [37] D. J. Lee. Passive decomposition and control of nonholonomic mechanical systems. *IEEE Transactions on Robotics*, 26(6):978–992, 2010.
- [38] D. J. Lee. Passive decomposition of mechanical systems with coordination requirements. *IEEE Transactions on Automatic Control*, 58(1):230–235, 2013.
- [39] D. J. Lee. Passive configuration decomposition and practical stabilization of nonholonomic mechanical systems with symmetry. In *Proc. IEEE Conference on Decision and Control*, pages 3620–3625, 2010.
- [40] H. Yang and D. J. Lee. Dynamics and control of quadrotor with robotic manipulator. In *Proc. IEEE Int’l Conference on Robotics and Automation*, pages 5544–5549, 2014.

- [41] F. Ruggiero, J. Cacace, H. Sadeghian, and V. Lippiello. Impedance control of vtol uavs with a momentum based external generalized forces estimator. In *Proc. IEEE Int'l Conference on Robotics and Automation*, pages 2093–2099, 2014.
- [42] B. Siciliano and W. J. Book. A singular perturbation approach to control of lightweight flexible manipulators. *The International Journal of Robotics Research*, 7(2):79–90, 1988.
- [43] A. D. Luca and B. Siciliano. Regulation of flexible arms under gravity. *IEEE Transactions on Robotics and Automation*, 9(4):463–467, 1993.
- [44] H. Yang, N. Staub, A. Franchi, and D. J. Lee. Modeling and control of multiple aerial-ground manipulator system (magmas) with load flexibility. In *Proc. IEEE/RSJ Int'l Conference on Intelligent Robots and Systems*, pages 4840–4847, 2018.
- [45] S. Park, Y. Lee, J. Heo, and D. J. Lee. Pose and posture estimation of aerial skeleton systems for outdoor flying. In *Proc. IEEE Int'l Conference on Robotics and Automation*, pages 704–710, 2019.
- [46] M. W. Spong, S. Hutchinson, and M. Vidyasagar. *Robot modelling and control*. WILEY, 2006.
- [47] C. Ha, Z. Zuo, F. B. Choi, and D. J. Lee. Passivity-based adaptive backstepping control of quadrotor-type uavs. *Robotics and Autonomous Systems*, 62(9):1305–1315, 2014.

- [48] S. Kim, S. Choi, and H. J. Kim. Aerial manipulation using a quadrotor with a two dof robotic arm. In *Proc. IEEE/RSJ Int'l Conference on Intelligent Robots and Systems*, pages 4990–4995, 2013.
- [49] G. Gioioso, A. Franchi, S. Savietti, S. Scheggi, and D. Prattichizzo. The flying hand: a formation of uavs for cooperative serial tele-manipulation. In *Proc. IEEE Int'l Conference on Robotics and Automation*, pages 4335–4341, 2014.
- [50] D. Mellinger, M. Shomin, N. Michael, and V. Kumar. Cooperative grasping and transport using multiple quadrotors. In *Proc. Int'l Symposium on Distributed Autonomous Robotic Systems*, 2010.
- [51] K. Sreenath and V. Kumar. Dynamics, control and planning for cooperative manipulation of payloads suspended by cables from multiple quadrotor robots. In *Robotics: Science and Systems*, 2013.
- [52] Z. Vafa and S. Dubowsky. The kinematics and dynamics of space manipulators: the virtual manipulator approach. *The International Journals of Robotics Research*, 9(4):3–21, 1990.
- [53] A. Sarlette, R. Sepulchre, and N. E. Leonard. Autonomous rigid body attitude synchronization. *Automatica*, 45(2):572–577, 2009.
- [54] M. Buss, H. Hashimoto, and J. B. Moore. Dextrous hand grasping force optimization. *IEEE Transactions on Robotics and Automation*, 12(3):406–418, 1996.
- [55] S. P. Boyd and B. Wegbreit. Fast computation of optimal contact forces. *IEEE Transactions on Robotics*, 23(6):1117–1132, 2007.

- [56] D. Sun and X. Shi; Y. Liu. Modeling and cooperation of two-arm robotic system manipulating a deformable object. In *Distributed Autonomous Robotic Systems*, pages 545–558, 2013.
- [57] T. Yoshikawa. Manipulability of robotic mechanisms. *The International Journal of Robotics Research*, 4(3):3–9, 1985.
- [58] J. E. Slotine and W. Li. *Applied nonlinear control*. Prentice Hall, 1991.
- [59] D. J. Inman. *Engineering Vibration*. Pearson, 2008.
- [60] A. D. Luca and B. Siciliano. Closed-form dynamic model of planar multilink lightweight robots. *IEEE Transactions on Systems, Man, and Cybernetics*, 21(4):826–839, 1991.
- [61] J. Cheong, W. K. Chung, and Y. Youm. Inverse kinematics of multi-link flexible robots for high-speed applications. *IEEE Transactions on Robotics and Automation*, 20(2):269–282, 2004.
- [62] Y. Nakamura, H. Hanafusa, and T. Yoshikawa. Task-priority based redundancy control of robot manipulators. *The International Journal of Robotics Research*, 6(2):3–15, 1987.
- [63] A. Yamashita, T. Arai, J. Ota, and H. Asama. Motion planning of multiple mobile robots for cooperative manipulation and transportation. *IEEE Transactions on Robotics*, 19(2):223–237, 2003.
- [64] Y. Hirata, Y. Kume, and T. Sawada. Handling of an object by multiple mobile manipulators in coordination based on caster-like dynamics. In *Proc. IEEE Int’l Conference on Robotics and Automation*, pages 807–812, 2004.

- [65] D. Mellinger, M. Shomin, N. Michael, and V. Kumar. Cooperative grasping and transport using multiple quadrotors. In *Distributed Autonomous Robotic Systems*, pages 545–558, 2013.
- [66] Gramazio Kohler Research. <http://www.gramaziokohler.arch.ethz.ch/web/e/forschung/index.html/>, Accessed: 2019-09-15.
- [67] ATOUN. <http://atoun.co.jp/products/atoun-model-k/>, Accessed: 2019-09-15.
- [68] N. Staub, M. Mohammadi, D. Bicego, Q. Delamare, H. Yang, D. Prati-
tichizzo, P. R. Giordano, D. J. Lee, and A. Franchi. The tele-magmas:
An aerial-ground comanipulator system. *IEEE Robotics & Automation
Magazine*, 25(4):66–75, 2018.
- [69] A. Hać and L. Liu. Sensor and actuator location in motion control of
flexible structures. *Journal of Sound and Vibration*, 167(2):239–261, 1993.
- [70] C. T. Chen. *Linear System Theory and Design*. Oxford University Press,
Inc., 1998.
- [71] F. Pasqualetti, S. Zampieri, and F. Bullo. Controllability metrics, lim-
itations and algorithms for complex networks. *IEEE Transactions on
Network Systems*, 1(1):40–52, 2014.

초록

본 학위논문에서는 로터로 구동되는 새로운 공중조작 시스템의 동역학과 제어문제에 대해서 기술한다. 본 논문에서 기술하는 새로운 공중조작 시스템은 1) 드론과 로봇팔을 결합한 드론-매니퓰레이터 시스템과 2) 유연성을 갖는 물체의 진동저감을 위한 로터기반 진동저감 모듈이며, 각각의 공중조작 시스템의 동역학 해석과 제어기법에 대해 기술한다.

드론-매니퓰레이터 시스템의 구동부족 문제와 높은 자유도의 비선형 동역학 문제를 해결하기 위해 수동성기반 동역학 분할기법을 적용하여 일반적인 다중 로터 드론의 구동부족 동역학과 같은 형태의 전체 시스템 무게중심의 병진운동 동역학과, 일반적인 완전 구동 로봇팔의 동역학과 같은 로봇 동역학으로 구성된 전체시스템의 회전 동역학으로 나누어짐을 보였으며 이 동역학 구조를 활용한 단일 및 다중 드론-매니퓰레이터의 협조제어기법을 제시하였다.

다음으로 로터구동에 기반한 진동저감 모듈 연구에서는 진동 저감을 위한 최소한의 로터를 가지며, 원하는 방향으로 최대한의 힘과 진동저감에 방해되는 최소한의 토크를 가지도록하는 최적설계 방법을 제안하였다. 이를 바탕으로 유연성을 갖는 물체위에 손쉽게 탈부착이 가능하며, 다양한 물체의 크기에 적용이 가능한 확장성을 확보하였으며, 탑재된 온보드 센서를 통해 물체의 변형 측정이 가능하도록 하였다. 진동저감을 위한 물체와 모듈이 결합되었을때의 동역학 해석 및 제어 가능성에 대하여 해석하였으며, 여러개의 모듈을 배치하였을때 제어와 추정을 최적화 하는 방법을 제시하였다. 마지막으로 관련된 시뮬레이션과 실험결과를 제시한다.

주요어: 드론, 공중조작, 동역학, 제어, 최적배치, 구동부족

학 번: 2014-30352

Acknowledgement

From 2008, I started my journey at Seoul National University and spent all of my 20s and early 30s in INRoL. Now, with this thesis, I would like to thank my family, friends, and advisers.

First and foremost, I would like to express my deep and sincere gratitude to my research advisor Prof. Dongjun Lee with whom I could learn strict attitude toward research and how to enjoy research. I am also deeply grateful to him for his inspiring advice, sincere supports, and encouragement throughout my study.

Besides my advisor, I would also like to express my sincere gratitude to my thesis committee chair Prof. Frank Chongwoo Park and committee members Prof. Kyujin Cho, Prof. Jaeheung Park, and Dr. Christian Ott for their inspiring comments, advice during my defense and for this thesis from other cities and countries during especially hard time of this pandemic due to COVID-19.

During my study at Seoul National University, it was my pleasure to study, discuss, explore knowledge, and grow with many fellow graduate students who encouraged and motivated me and also made the time of my study enjoyable and fun. I would like to thank all the former and current INRoL members and my friends who have been studied at Bldg. 301 together and graduated.

I would like to thank Dr. Antonio Franchi and Dr. Nicolas Staub for our collaborative work of Tele-MAGMaS and flexible MAGMaS at LAAS-CNRS

in France during 2015 and 2016. I also appreciate to other graduate students in LAAS-CNRS who spent enjoyable and inspiring time during my visit.

Last but not least, I must express my very profound gratitude to my parents and to my elder sister for providing me with unfailing support and continuous encouragement throughout my years of study and through the process of study and writing this thesis. This accomplishment would not have been possible without them.

Jan. 2021

Hyunsoo Yang